UNIVERSITÀ DELLA CALABRIA

UNIVERSITA' DELLA CALABRIA

Dipartimento di FISICA

Dottorato di Ricerca in

Scienze e Tecnologie Fisiche Chimiche e dei Materiali

CICLO

XXIX

Synthetic receptors at the interface: molecular architectures and host-guest complexation by Sum-Frequency Spectroscopy

Settore Scientifico Disciplinare FIS/07

Coordinatore: Ch.mo Prof. (Vincenzo Carbone)

Firma Vincenzo Carbone

Supervisore/Tutor: Ch.mo Prof. (Pasquale Pagliusi)

Firma

Dottoranda: Dott.ssa (Arianna Aprile)

Firma Arianna Aprile

Synthetic receptors at the interface: molecular architectures and host-guest complexation by Sum-Frequency Spectroscopy

Arianna Aprile

Department of Physics

Università della Calabria

This dissertation is submitted for the degree of

Doctor of Philosophy

Università della Calabria 2017

A papà, mamma, Simona e Antonio.

Acknowledgements

I would like to thank all the people I met during these three years, because each one left me something, both scientifically and humanly. This wonderful personal growth experience would not have been complete without the continued support of my advisor and of all the people I worked with. I also thank my family, my partner and my friends for the unconditional encouragement in pursuing my goals.

Ad meliora et maiora semper.

Sommario

Il riconoscimento molecolare in natura è uno degli eventi chimici più diffusi e regola gran parte dei processi che avvengono nei sistemi viventi. Ad esempio, l'interazione tra recettori molecolari e specifici ligandi disciplina fenomeni come il trasporto di acqua e nutrienti all'interno delle cellule. Ispirandosi alla selettività e all'efficienza di tali recettori molecolari, negli ultimi decenni i chimici supramolecolari hanno sintetizzato una vasta gamma di composti che ne emulano le caratteristiche, motivati dalla loro potenziale applicabilità in diversi ambiti. Studiare i fenomeni di complessazione *in-situ* alle interfacce è essenziale per prevedere le prestazioni di complessazione in termini di conformazione, orientamento e organizzazione del recettore. Tutti i sensori sono basati, infatti, sull'accoppiamento tra superfici opportunamente funzionalizzate, che vengono esposte a mezzi contenenti i composti da rilevare, e meccanismi di trasduzione che consentono di convertire l'interazione chimica recettore-analita in un segnale leggibile.

In questo lavoro, sono riportati i primi studi di spettroscopia vibrazionale a somma frequenza (SFVS) sull'architettura molecolare di recettori sintetici e sull'evento di riconoscimento molecolare alle interfacce solido/gas e liquido/gas. In particolare, la capacità dei cavitandi chinossalinici (QxCav) di complessare selettivamente i composti aromatici volatili in fase gassosa e liquida è stata studiata come sistema di prova, organizzando opportunamente i recettori su superfici solide e liquide. L'analisi quantitativa ha permesso di correlare l'orientamento medio dei ligandi con quello dei siti di legame, consentendo di ricostruire una geometria di inclusione *"on-axis"* dell'analita all'interno della cavità del cavitando. Per il riconoscimento molecolare in fase gassosa, i cavitandi chinossalinici sono stati trasferiti tramite metodo di Langmuir-Schaefer su *self-assembled monolayer* (SAM) di octadecyltrichlorosilane (OTS), N,N-dimethyl-N-octadecyl-3-aminopropyltrimethoxysilylchloride (DMOAP) e su SAM misti di octyltrichlorosilane/OTS (1: 1) su substrati di silice fusa. Le architetture molecolari dei monolayer e dei bilayer ibridi QxCav-SAM all'interfaccia solido-gas sono state dedotte e correlate mediante SFVS. I risultati hanno evidenziato che il QxCav è sempre in una configurazione chiusa, detta *vase*, e orienta la bocca della cavità verso la fase gas, mentre la molecola ospite è complessata con il suo asse principale parallelo a quello del recettore, orientando la parte aromatica verso l'interno della cavità per via dell'interazione $CH-\pi$ aromatica. Lo stesso tipo di geometria di complessazione *on-axis* è stata ricostruita per l'interazione di un composto aromatico con un derivato del QxCav all'interfaccia liquido/gas. Nel caso specifico, un monolayer di cavitandi QxBOX, la cui cavità è bloccata in una configurazione *vase* permanente attraverso linker alifatici, è stato utilizzato per studiare le interazioni con un analita disperso in fase acquosa a diverse concentrazioni. L'esperimento ha permesso di dedurre l'angolo polare medio di recettori e ligandi, chiarendo che la geometria di inclusione della

molecola all'interno della cavità dipende solo dalla conformazione dello strato sovrastante di cavitandi e non è influenzata dalla concentrazione dell'analita in fase liquida.

In questo contesto, lo studio può essere esteso a diversi sistemi recettore-ligando aprendo ad una vasta gamma di possibili applicazioni. I cavitandi tetrafosfonati, ad esempio, hanno dimostrato un'alta selettività nella complessazione di alcune delle droghe più comuni, come metanfetamine ed eroina. Gli stessi recettori, inoltre, formano complessi anche con un aminoacido come la sarcosina, considerato un *marker* per il tumore alla prostata. Tale proprietà li rende degli ottimi candidati per applicazioni di ambito biologico e medico. Parallelamente, cavitandi chinossalinici con gruppi funzionali specifici, come il carbossile, hanno dimostrato una forte affinità verso composti esplosivi nitroaromatici, offrendo una nuova strategia per il loro rilevamento in aria o nel terreno.

Questo lavoro propone un nuovo approccio allo studio delle interazioni recettore-ligando alle interfacce sfruttando i vantaggi che una tecnica come la spettroscopia vibrazionale a somma di frequenza offre. La sua specificità verso le superfici e la sua sensibilità all'ordine polare permettono di studiare *in-situ* i fenomeni di complessazione correlandoli all'architettura molecolare dei recettori. Questo tipo di analisi è in grado di guidare una sintesi più razionale dei recettori e l'ottimizzazione delle loro prestazioni di complessazione in funzione della conformazione e dell'organizzazione all'interfaccia.

Abstract

Molecular recognition is among the most important chemical events in living systems and has been emulated in supramolecular chemistry, driven by chemical and biochemical sensing potential. Identifying host–guest association *in-situ* at the interface, between the substrate-bound receptors and the analyte-containing media, is essential to predict complexation performances in term of the receptor conformation, orientation and organization. Herein, the first sum-frequency vibrational spectroscopy studies of receptor molecular architecture and recognition event at the solid-gas and liquid-gas interfaces are reported. The binding capability of tetraquinoxaline cavitand toward volatile aromatic compounds in gas and in liquid phase is investigated as test system. The selective complexation of the receptors toward aromatic compounds is proved, organizing them on solid and liquid surfaces. Quantitative analysis allows to correlate the average orientations of the guest molecules and the host binding pockets, establishing "on-axis" complexation of the analyte within the cavitand cavity.

For the molecular recognition in gas phase, Quinoxaline cavitands (QxCav) are transferred by Langmuir-Schaefer method on selfassembled monolayers (SAMs) of octadecyltrichlorosilane (OTS), N,N-dimethyl-N-octadecyl-3- aminopropyltrimethoxysilyl chloride (DMOAP) and mixed octyltrichlorosilane/OTS (1:1) on fused silica substrates. The molecular architectures of both the hydrophobic SAMs templates and the hybrid cavitand-organosilanes bilayers at the solid–air interface are investigated and correlated by sum-frequency vibrational spectroscopy. The results show that QxCav is always in the closed *vase* configuration and orient its cavity mouth toward the gas phase, while the guest molecule is engulfed with its main axis parallel to that of the receptor.

This "on-axis" inclusion is also deduced for the *complexes* formation at the liquid/gas interface, where a Langmuir film of QxBOX cavitands, whose cavity mouth is blocked in a permanent *vase* configuration through aliphatic linkers, is probed by SFVS to show the first evidence of complexation of an aromatic guest dissolved in water phase at different concentrations. In particular, the experiment allows to deduce the average polar orientation of both receptors and guest molecules, elucidating that the molecule-within-molecule configuration only depends on the uppermost receptor layer and it is not affected by the concentration of the analyte in the liquid phase.

In this context, this study can be extended to several receptor-ligand systems, opening to a wide range of possible applications. Tetraphosphonate cavitands, for example, have demonstrated high selectivity in the complexation of some of the most common illicit drugs, as methamphetamine and heroin. The same receptors form also *complexes* with aminoacids as sarcosine, considered a marker for prostate cancer. Such properties make them excellent candidates for biological and medical applications. In parallel, quinoxaline cavitands with specific functional groups at the upper rim, such as COOH-QxCav, have shown a strong affinity towards nitroaromatic explosives, providing a new strategy for their detection in air and soil.

This work proposes a new approach to the study of receptor-ligand interactions at the interfaces exploiting the benefits that a technique as SFVS offers. Its intrinsic surface-specificity and its sensitivity to polar order allow to study the complexation phenomena *in-situ,* correlating them to the receptor molecular architecture. This analysis can lead to a more rational synthesis of the receptors and to the optimization of their complexation capability as a function of the conformation and organization at the interfaces.

Contents

List of Figures

List of Tables

Chapter 1

Introduction

Molecular recognition is one of the most important chemical process in nature. The biological mechanisms between receptors and ligands, such as antigen-antibody, RNA-ribosome and DNA-protein, relies on specific binding interactions between two or more molecules. The high selectivity of the receptor is guaranteed by the complementarity in size and shape and by the strong chemical affinity toward a specific class of ligands. These recognition events in living systems regulate many biological processes as, for example, the regulation of sleep and wakefulness, due to the selective interaction between melatonin and its receptors, and control of growth, related to the somatotropin hormone and its interaction with membrane receptors.

Taking inspiration from biological systems, in the last decades a large number of different chemical compounds have been synthesized trying to reproduce the binding properties of such receptors. The supramolecular chemists designed and synthesized a large variety of different host molecules for various applications. From detection of illicit drugs [1], to monitoring of environmental pollution [2], preventive diagnosis of diseases [3] and entrapment of biologically active molecules [4], synthetic receptors demonstrated a great versatility in many fields and for a large area of applications. Their use in chemical detection could lead, thus, to the development of more precise and reliable chemosensors.

In this scenario, the so called *Cavitands* have attracted considerable attention in the last years. Being host-molecules with an open-ended cavity of molecular dimension, they are able to selectively trap specific classes of ligands. Several types of cavitands have been widely studied by different research groups that produced a rich scientific literature, focusing on their synthetic strategies and complexation capabilities [5–7]. Their abilities to entrap guests have been characterized in solid state [8, 9], in solution [10] and in gas phase [11, 12] with different techniques such as NMR spectroscopy and X-rays diffraction. In view of using them for the realization of sensing devices, the host-guest interaction mechanisms at the interfaces require a thorough understanding. An investigation of the binding properties of these host molecules

directly at the interface lacks. Their conformation, indeed, can affect their performance in complexing guests and, in addition, their selectivity and sensitivity at the interface have to be verified. A powerful technique, able to provide at the same time both chemical and structural information, with sub-monolayer sensitivity, high surface specificity, non-invasive and applicable *in-situ* to all systems accessible by light, is Sum Frequency Vibrational Spectroscopy (SFVS). This technique exploits a second-order non-linear optical process called Sum Frequency Generation (SFG).

In the last decades SFVS has been used as a versatile analytical tool to study different types of surfaces and interfaces accessible by light. From Chemistry to Biology and Medicine, SFVS allowed to investigate systems as liquid [13–15] and buried [16–18] interfaces, polymers[19–21], molecular films [22]and membranes [23–26].

The pioneering work of Shen and co-workers led to the first experimental demonstration of SFG from a surface [27] whose basic principles can be found in a wide range of scientific publications [28–33]. It is a second-order non-linear optical process that, under the electric dipole approximation, occurs in non-centrosymmetric media and at the interfaces where the bulk symmetry is naturally broken. The resulting surface specificity of SFVS and its sensitivity to polar order, make it one of the best surface spectroscopy to study molecular systems. SFVS differs from other surface sensitive spectroscopies (LEED, Auger and mass spectroscopy, etc.) since it allows to work *in-situ* without particular experimental conditions (eg ultra-high vacuum). Moreover, it also enables to probe systems such as liquid interfaces, polymer films and membranes to determine their conformation. This thesis will be devoted to the study of cavitand-decorated solid and liquid surfaces. In particular, the molecular architectures of these receptors will be investigated and the molecular recognition events, due to the specific host-guest interactions, will be pointed out.

In the second chapter the investigation of a cavitand-decorated solid substrate is reported. A quinoxaline cavitand (QxCav) [34] layer is transferred on a fused silica substrate coated with an organosilane self sssembled monolayer (SAM), forming a Solid Supported Hybrid Bilayer (SSHB). The QxCav is known for its selectivity toward aromatic compounds and its properties have been widely studied in solution [35] and in solid state [2, 36]. A thorough understanding of its complexation mechanism, directly at the interfaces, is the first mandatory step to elucidate how the molecular architecture affects its sensing capabilities. For example, a very disordered cavitand film can reduce the number of binding sites and promotes the non-specific interactions with the surface, that could misrepresent the recognition event. In this regard, a technique as SFVS can drive the realization of a more efficient organization of these receptors, in order to still preserve their selectivity and sensitivity from solution (or solid state) to the interfaces. The molecular architecture of such membrane-like structure is characterized

by SFVS and its conformation is deduced. Complementary techniques, as Atomic Force Microscopy and Contact Angle Measurements, are employed to obtain additional morphological information.

The SSHB is then used to show the first evidence of molecular recognition of an aromatic compound at the solid/gas interface. The QxCav capability to entrap aromatic guests, probed by SFVS, is proved and reported in the third chapter. Its selectivity toward aromatics is due to the four quinoxaline wings that form the cavity of the receptor and that can assume a *vase* or *kite* conformation in which they are close or open, respectively. The *vase-to-kite* switching can be controlled with external parameters as pH [37, 38] or temperature [39] and can affect the engulfing properties of the receptor. The QxCav, indeed, is able to complex guests only in the vase conformation, thanks to the interactions between the analyte and the quinoxaline wings. In this regard, the *vase-or-kite* conformation of the QxCav in SSHB is deduced and its average orientation is compared with that of complexed guest, elucidating the geometry of molecule-within-molecule configuration, in which the analyte is engulfed with its main axis parallel to that of the receptor. In addition, the selectivity of the QxCav toward aromatic compounds is tested to verify if it is still preserved at the interface. For the SSHB exposed to an aliphatic analyte, no significant interaction occurred, demonstrating that the absence of specific host-guest bindings does not promote any net polar orientation of the analyte.

Besides the interest in the development of chemical sensors for detection of target molecule in the gas phase, the pollution of water sources, the diffusion of illicit drugs and the need of new methods for preventive diagnosis of diseases, require selective and sensitive devices that are able to work in liquid environment. In particular, good stability and efficiency under pH or temperature variation, presence of charged ions or different molecular species are pivotal. In this regard, the fourth chapter is focused on the molecular recognition at cavitand-decorated liquid interface. A new QxCav derivative, namely QxBOX, is used for detecting aromatic guests. Thanks to its rigid structure, QxBOX demonstrated a good thermal resistance and an insensitivity to pH variation, due to its cavity mouth blocked in a vase configuration [40]. The host-guest interactions are studied by SFVS and the average orientation of both receptors and ligands is deduced from SF spectra at different concentrations of the analyte in solution, in order to test the ability of QxBOX in engulfing aromatic guests at liquid/air interface.

1.1 Sum-Frequency Vibrational Spectroscopy

The work of Blombergen *et al.* in 1962 led to the first theoretical demonstration of the Sum Frequency Generation (SFG) [41]. In the same years, Bass and coworkers reported the first observation of SFG in a crystal of triglicyne sulfate [42], where two laser beams at ω_1 and

ω_2 interacted in a non-linear medium and generated a SF radiation as the consequence of a non-linear polarization. In 1986 Shen and coworkers, reported the first surface vibrational SF spectrum from a monolayer of Coumarin on glass [43]. This work opened a new scenario for the Surface Science, because demonstrated the possibility to investigate surfaces and interfaces with a non-invasive optical technique able to yield chemical and conformational information. The intrinsic sensitivity and selectivity toward surfaces and interfaces makes Sum Frequency Vibrational Spectroscopy (SFVS) one of the most prominent optical technique for the *in-situ* investigation of molecular architecture at the interfaces.

1.2 Theory of Sum Frequency Generation

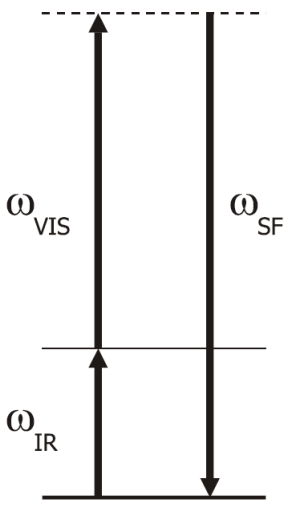

Figure 1.1: SFG process

The Sum Frequency Generation (SFG) [44–47] is a two-photon process in which absorption of an IR photon promotes an excitation to the first vibrational level and the *upconversion* due to the anti-Stokes Raman scattering with a visible photon leads the system in a virtual state. The resulting emission of a coherent SF photon $\omega_{SF} = \omega_1 + \omega_2$ is the consequence of a process that is both IR and Raman-active. In other words, the medium behaves like a collection of oscillating dipoles which emit radiation at ω_{SF}. Both energy $\omega_{SF} = \omega_1 + \omega_2$ and momentum $\overrightarrow{k}_{SF} = \overrightarrow{k}_1 + \overrightarrow{k}_2$ conservation have to be satisfied.

Sum Frequency Generation (SFG) is a coherent non-linear optical process due to a second order polarization $\overrightarrow{P}^{(2)}_{eff}$ induced in a medium by two incident electric fields $\overrightarrow{E}(\omega_1)$ and $\overrightarrow{E}(\omega_2)$:

$$\overrightarrow{P}^{(2)}_{eff}(\omega = \omega_1 + \omega_2) = \overrightarrow{P}^{(2)}(\omega) - \nabla \cdot \overrightarrow{Q}^{(2)} + \frac{c}{i\omega}\nabla \cdot \overrightarrow{M}^{(2)}(\omega) + \ldots \tag{1.1}$$

The three terms in eq. 1.1 that contribute to second order polarization are due to electric dipole, electric quadrupole and magnetic dipole, respectively. The $\overrightarrow{P}^{(2)}(\omega)$ term vanishes in media with inversion symmetry while it becomes dominant at the interfaces where the symmetry of the system is naturally broken. This makes SFG highly surface-specific. The

other two terms are in general non-vanishing also for media with inversion center and they give a bulk contribution. Under electric dipole approximation, these two terms can be neglected and $\vec{P}^{(2)}(\omega)$ can be written as:

$$\vec{P}^{(2)}(\omega_1+\omega_2) = \varepsilon_0 \overleftrightarrow{\chi}^{(2)} : \vec{E}(\omega_1)\vec{E}(\omega_2) \tag{1.2}$$

where $\vec{E}(\omega_1)$ and $\vec{E}(\omega_2)$ are the two incident electric fields that oscillate at ω_1 and ω_2, typically visible and IR frequencies when SFG is used for vibrational spectroscopy. In eq. 1.2, $\overleftrightarrow{\chi}^{(2)}$ is the surface second-order non-linear susceptibility that is tightly related to the electronic and molecular structure of the medium and does not depend on external factors related to the experimental setup. The SF intensity in reflection geometry is given by eq. 1.3:

$$I(\omega_{SF}) = \frac{\omega_{SF}^2}{8\varepsilon_0 c^3 cos^2\beta_{SF}} |\chi_{eff}^{(2)}|^2 I(\omega_1) I(\omega_2) \tag{1.3}$$

where $I(\omega_i)$ is the beam intensity at ω_i, $\chi_{eff}^{(2)}$ is the effective non-linear susceptibility and β_{SF} is the exit angle of the SF radiation. In contrast to linear processes as Raman scattering, the emitted SF radiation is coherent and generated in defined direction β_{SF}, that can be calculated from the phase matching condition in the surface plane, where only the parallel components of the wave vectors of the input/output beams are considered (fig. 1.2):

$$k_{||}(\omega_1) + k_{||}(\omega_2) = k_{||}(\omega_{SF}). \tag{1.4}$$

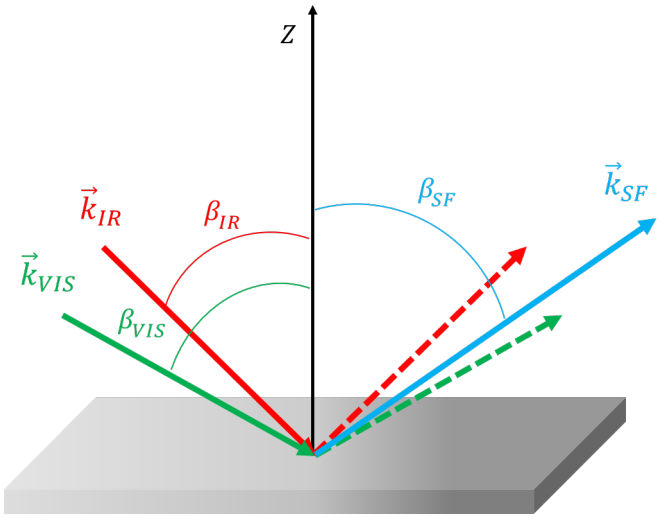

Figure 1.2: Schematic view of the SFG reflection geometry

The eq. 1.4 can be also written as a function of the refractive index of the medium $n(\omega_i)$ and of the angle β_i the beam at frequency ω_i as shown in eq. 1.5.

$$\omega_1 n(\omega_1) sin\beta_1 + \omega_2 n(\omega_2) sin\beta_2 = \omega_{SF} n(\omega_{SF}) sin\beta_{SF}. \tag{1.5}$$

The effective second-order non-linear susceptibility that appears in eq. 1.3 can be defined as:

$$\chi^{(2)}_{eff} = \left[\overleftrightarrow{L}(\omega_{SF}) \cdot \hat{e}_{SF}\right] \cdot \overleftrightarrow{\chi}^{(2)} : \left[\overleftrightarrow{L}(\omega_1) \cdot \hat{e}_1\right] \left[\overleftrightarrow{L}(\omega_2) \cdot \hat{e}_2\right] \tag{1.6}$$

where $\hat{e}_i$ and $\overleftrightarrow{L}(\omega_i)$ are the unit polarization vector of the electric field and Fresnel factor at frequency ω_i. The Fresnel factors $\overleftrightarrow{L}(\omega_i)$ can be obtained from the following relations [44]:

$$\begin{aligned}
L_{xx}(\omega_i) &= \frac{2n_1(\omega_i)cos\gamma_i}{n_1(\omega_i)cos\gamma_i + n_2(\omega_i)cos\beta_i} \\
L_{yy}(\omega_i) &= \frac{2n_1(\omega_i)cos\beta_i}{n_1(\omega_i)cos\beta_i + n_2(\omega_i)cos\gamma_i} \\
L_{zz}(\omega_i) &= \frac{2n_2(\omega_i)cos\beta_i}{n_1(\omega_i)cos\gamma_i + n_2(\omega_i)cos\beta_i} \left(\frac{n_1(\omega_i)}{n'(\omega_i)}\right)^2
\end{aligned} \tag{1.7}$$

where $n'(\omega_i)$, $n_1(\omega_i)$ and $n_2(\omega_i)$ are the refractive indexes of surface layer, first medium and second medium at frequency ω_i, respectively. β_i is the angle formed with the surface normal and γ_i is the refracted angle (that can be deduced from Snell's law $n_1(\omega_i)sin\beta_i = n_2(\omega_i)sin\gamma_i$) at frequency ω_i. The determination of the refractive index $n'(\omega_i)$ is crucial for a correct quantitative analysis of the SFG spectra [48].

1.3 Effective non-linear susceptibility

The second-order non-linear susceptibility, a third-rank tensor, reflects the structural symmetry of the medium. Under symmetry consideration, some of the 27 tensor elements vanish and others are dependent on each other. This reduces the total number of independent elements that have to be deduced. The SF signal coming from a non-centrosymmetric solid or from an interface also depends on external parameters (such as refraction indexes, input/output angles, polarizations of the beams, etc.) and, for this reason, it is useful to consider the effective second-order non-linear susceptibilities $\chi^{(2)}_{eff}$ for different polarization of the involved input/output beams. All the systems investigated in this thesis have an azimuthally isotropic symmetry and to deduce the elements of the second-order non-linear susceptibility tensor $\overleftrightarrow{\chi}^{(2)}$ at least three

polarization combinations, namely SSP, SPS and PPP are needed. The three capital letters indicate the SF, the visible and the IR polarization, respectively. S-polarized and P-polarized light means that the relative electric field oscillates in the sample plane and in the incidence plane, respectively. For this reason, the SSP and SPS polarization combinations can only excite vibrational modes whose IR dipole moment has a component parallel and perpendicular to the incidence plane, respectively.

1.3.1 $\chi^{(2)}_{eff}$ for azimuthally isotropic surface

In the case of an azimuthally isotropic surface (C_∞ symmetry), the number of independent and non-vanishing terms of $\overleftrightarrow{\chi}^{(2)}$ tensor can be reduced to only three:

$$\begin{aligned} &\chi^{(2)}_{xxz} = \chi^{(2)}_{yyz} \\ &\chi^{(2)}_{xzx} = \chi^{(2)}_{yzy} = \chi^{(2)}_{zxx} = \chi^{(2)}_{zyy} \\ &\chi^{(2)}_{zzz} \end{aligned} \tag{1.8}$$

expressed in the lab coordinates (X,Y,Z). Nevertheless, there are a lot of practical issues related to the determination of the susceptibility tensor elements. As mentioned above, since the SF intensity depends on the effective second-order non-linear susceptibility $\chi^{(2)}_{eff}$, it is useful to rewrite its terms as a function of $\overleftrightarrow{\chi}^{(2)}$ elements (through eq. 1.6), Fresnel factors and input/output angles as in eq. 1.9. At this point it is clear that the determination of refractive index of the surface layer n', which affects the calculation of $L_{zz}(\omega_i)$ terms (see eq. 1.7), is critical for the determination of the $\chi^{(2)}_{eff}$ and, as it will shown in sec. 1.4, of the correct orientational distribution of the molecular moieties.

$$\begin{aligned} \chi^{(2)}_{eff,SSP} &= L_{yy}(\omega_{SF})L_{yy}(\omega_1)L_{zz}(\omega_2)sin\beta_2\chi^{(2)}_{xxz} \\ \chi^{(2)}_{eff,SPS} &= L_{yy}(\omega_{SF})L_{zz}(\omega_1)L_{yy}(\omega_2)sin\beta_1\chi^{(2)}_{xzx} \\ \chi^{(2)}_{eff,PPP} &= \left\{ \begin{array}{l} L_{zz}(\omega_{SF})L_{zz}(\omega_1)L_{zz}(\omega_2)sin\beta_{SF}sin\beta_1sin\beta_2\chi^{(2)}_{zzz} + \\ -L_{xx}(\omega_{SF})L_{xx}(\omega_1)L_{zz}(\omega_2)cos\beta_{SF}cos\beta_1sin\beta_2\chi^{(2)}_{xxz} + \\ -L_{xx}(\omega_{SF})L_{zz}(\omega_1)L_{xx}(\omega_2)cos\beta_{SF}cos\beta_1sin\beta_2\chi^{(2)}_{xzx} + \\ +L_{zz}(\omega_{SF})L_{xx}(\omega_1)L_{xx}(\omega_2)sin\beta_{SF}cos\beta_1cos\beta_2\chi^{(2)}_{zxx} \end{array} \right\} \end{aligned} \tag{1.9}$$

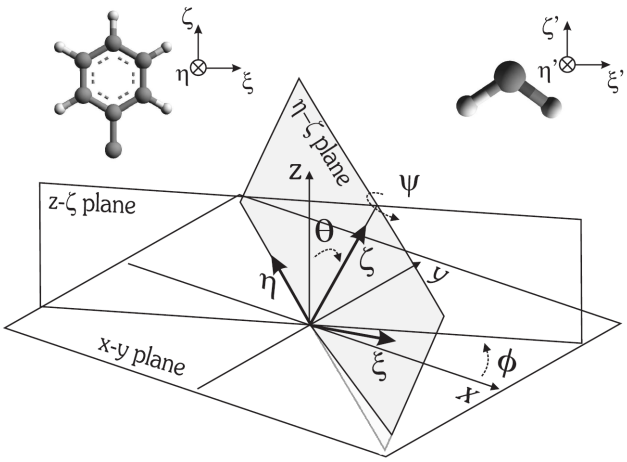

Figure 1.3: Sample and molecular frame for the phenyl and methylene groups.

1.4 Molecular hyperpolarizability

The surface non-linear susceptibility tensor $\overleftrightarrow{\chi}^{(2)}$ is a macroscopic quantity that describes the behavior a complex system and takes into account all the possible resonant modes of the molecular species involved in the process:

$$\chi^{(2)}_{ijk} = \chi^{(2)}_{NR,ijk} + \sum_q \frac{A_{q,ijk}}{\omega_2 - \omega_q + i\Gamma_q} \tag{1.10}$$

where $\chi^{(2)}_{NR,ijk}$ is the non-resonant contribution, while $A_{q,ijk}$, ω_q and Γ_q are the amplitude, the resonant frequency and the damping constant of the q-th vibrational mode, respectively.

The macroscopic resonant amplitude $A_{q,ijk}$ introduced in eq. 1.10 is related to the microscopic quantity $a_{q,lmn}$, that is the amplitude of the molecular hyperpolarizability expressed in the frame (ξ, η, ζ) (fig. 1.3) of the molecular group, through the eq. 1.11, in which the calculation of local-field correction (neglected in eq. 1.11) is postponed and addressed in the evaluation of surface refractive index n' [48].

$$A_{q,ijk} = N_s \sum a_{q,lmn} \left\langle \left(\hat{i}\cdot\hat{l}\right)\left(\hat{j}\cdot\hat{m}\right)\left(\hat{k}\cdot\hat{n}\right)\right\rangle \tag{1.11}$$

The term N_s is the surface density of the molecular moiety and the angular brackets represent the ensemble average over the orientational distribution function (ODF). The hyperpolarizability of a molecular group depends on the IR dipole moment derivative $\partial\mu_n/\partial Q$ and by the

Raman polarizability derivative $\partial\alpha^{(1)}_{lm}/\partial Q$ of the q-th vibrational mode as shown in eq. 1.12:

$$a_{q,lmn} = \frac{\triangle\rho_q}{2\omega_q}\frac{\partial\alpha^{(1)}_{lm}}{\partial Q}\frac{\partial\mu_n}{\partial Q} \tag{1.12}$$

where Q is the classical normal coordinate and $\triangle\rho_q$ is the population difference between the q-th vibrational mode and the ground state. It is important to remark that a resonance is SFG active if the q-th vibrational mode is both IR and Raman active or, equivalently, if the molecule does not have inversion center. If the visible and IR beams are far to induce electronic transitions, the Raman polarizability derivative tensor is symmetric under exchange of the indexes. This means that the first two indexes of the susceptibility tensor elements are interchangeable too. Thanks to this approximation the number of independent tensor elements has been already reduced in eq. 1.8.

The resonant amplitudes $A_{q,ijk}$, corresponding to the q-th resonant mode, allow to obtain information about the average orientation of the molecular moiety (eq. 1.11). For an azimuthally isotropic surface, the only three independent resonant amplitudes $A_{q,xxz}$, $A_{q,xzx}$ and $A_{q,zzz}$ can be obtained by the SF spectra for different polarization configurations SSP, SPS and PPP through the following relations (see eq. 1.9):

$$\begin{aligned}
A_{q,SSP} &= L_{yy}(\omega_{SF})\,L_{yy}(\omega_1)\,L_{zz}(\omega_2)\sin\beta_2\,A_{q,xxz}\\
A_{q,SPS} &= L_{yy}(\omega_{SF})\,L_{zz}(\omega_1)\,L_{yy}(\omega_2)\sin\beta_1\,A_{q,xzx}\\
A_{q,PPP} &= -L_{xx}(\omega_{SF})\,L_{xx}(\omega_1)\,L_{zz}(\omega_2)\cos\beta_{SF}\cos\beta_1\sin\beta_2\,A_{q,xxz}+\\
&\quad +[-L_{xx}(\omega_{SF})\,L_{zz}(\omega_1)\,L_{xx}(\omega_2)\cos\beta_{SF}\sin\beta_1\cos\beta_2+\\
&\quad +-L_{zz}(\omega_{SF})\,L_{xx}(\omega_1)\,L_{xx}(\omega_2)\sin\beta_{SF}\cos\beta_1\cos\beta_2]\,A_{q,xzx}+\\
&\quad +L_{zz}(\omega_{SF})\,L_{zz}(\omega_1)\,L_{zz}(\omega_2)\sin\beta_{SF}\sin\beta_1\sin\beta_2\,A_{q,zzz}
\end{aligned} \tag{1.13}$$

1.4.1 Bond additivity model: CH_3 case

The simplest way to estimate the hyperpolarizability of a certain molecular group, far from electronic resonances, is to assume an additivity model that takes into account all the contributions of each bonds of the moiety. An important role is played by the geometry of the group that, according to the symmetry of the system, affects the hyperpolarizability tensor. In this section the calculation of the hyperpolarizability tensor for the methyl (CH_3) group is reported to give an example of the bond additivity model application and because the results obtained will be used in the following chapters. The methyl group is, indeed, a good vibrational marker, whose symmetric stretching mode can be used for the determination of its average orientation.

Furthermore, in the following chapters the analysis on the methyl mode will allow to deduce the alkyl chains conformation of both surfactant monolayers and cavitand/surfactants hydrid bilayers. For the methyl (CH_3) group, each CH bond has an IR dipole moment derivative μ_0 along the bond axis and a Raman polarizability derivative tensor with a cylindrical symmetry:

$$\alpha_0 = \begin{pmatrix} \alpha_0 \cdot R & 0 & 0 \\ 0 & \alpha_0 \cdot R & 0 \\ 0 & 0 & \alpha_0 \end{pmatrix} \tag{1.14}$$

where the parameter R is related to the anisotropy of CH bond polarizability derivative. Its value can be determined from theoretical calculations ($R = 0.14$) [49] or deduced by Raman spectra [50] ($R = 0.18$). Because of the C_{3V} symmetry of the methyl group, it is convenient to choose the symmetry main axis of the moiety as the ζ axis of the molecular frame. To simplify the following calculations, one of the CH bond is supposed to lie in the $\xi\zeta$ plane (see fig. 1.4).

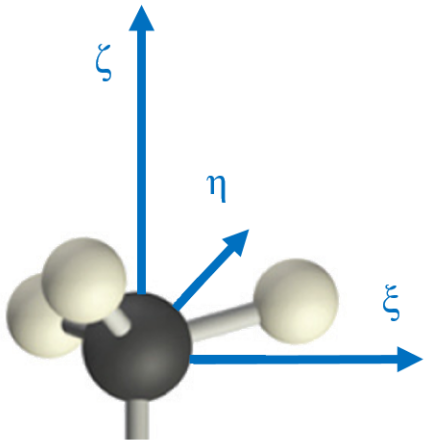

Figure 1.4: Methyl group in molecular frame (ξ, η, ζ)

For the total symmetric stretch of the methyl group the net IR dipole moment derivative is along the ζ axis:

$$\frac{\partial \mu_\zeta}{\partial Q} = \sum_{i=1}^{3} \frac{\partial \mu_\zeta}{\partial r_i} \frac{\partial r_i}{\partial Q} = \frac{1}{\sqrt{3}} \mu_0 \hat{\zeta} \tag{1.15}$$

where r_i identifies the direction of the single CH bond. In a similar way, it is also possible to get the Raman polarizability derivative tensor of the whole molecular group switching to

normal coordinate:

$$\begin{aligned}\frac{\partial \alpha_{\zeta\zeta}}{\partial Q} &= \sum_{i=1}^{3} \frac{\partial \alpha_{\zeta\zeta}}{\partial r_i}\frac{\partial r_i}{\partial Q} = \frac{1}{3\sqrt{3}}(1+8R)\,\alpha_0 \\ \frac{\partial \alpha_{\xi\xi}}{\partial Q} &= \frac{\partial \alpha_{\eta\eta}}{\partial Q} = \sum_{i=1}^{3} \frac{\partial \alpha_{\xi\xi}}{\partial r_i}\frac{\partial r_i}{\partial Q} = \frac{1}{3\sqrt{3}}(4+5R)\,\alpha_0\end{aligned} \tag{1.16}$$

At this point it is possible to write the nonvanishing hyperpolarizability elements as follows:

$$\begin{aligned}a^{(2)}_{\xi\xi\zeta} &= a^{(2)}_{\eta\eta\zeta} = \left(\frac{4+5R}{9}\right)\frac{\alpha_0\mu_0}{2\omega_q}\triangle\rho_q \\ a^{(2)}_{\zeta\zeta\zeta} &= \left(\frac{1+8R}{9}\right)\frac{\alpha_0\mu_0}{2\omega_q}\triangle\rho_q\end{aligned} \tag{1.17}$$

For the methyl group case it will prove useful defining a quantity as

$$r = \frac{a^{(2)}_{\xi\xi\zeta}}{a^{(2)}_{\zeta\zeta\zeta}} \simeq 2.2\,, \tag{1.18}$$

[51] called depolarization ratio.

1.5 Experimental setups

To carry out the experiments two different experimental setups have been used: a broad band (BB) and a narrow band (NB) SF scheme. The BB-SF setup produces femtosecond IR laser pulses with a large bandwidth ($\simeq$150 cm^{-1}) that allows to obtain a portion of the vibrational spectrum without tuning the IR central frequency. On the contrary, the visible laser pulses have a narrow band ($\simeq$10 cm^{-1}) for a good resolution of the SF spectra. The NB-SF scheme generates picosecond IR and visible pulses with a spectral resolution of $\simeq$6 cm^{-1}. For both the setups the SF signal is generated in reflection geometry by the impinging IR and visible beams.

1.5.1 BB-SFG setup

A femtosecond Ti:sapphire oscillator (MIRA 900F, Coherent Inc.), with center wavelength at 800 nm, is the seed laser for a regenerative amplifier (Legend FHE, Coherent Inc.) which produces 120 fs pulses at 1kHz repetition rate and pulse energy up to 2.5 mJ. The amplifier output

is then split into two beams. The first one is used to pump an Optical Parametric Amplifier (OPerA, Coherent Inc.), which coupled with a DFG extension (based on Difference Frequency Generation) generates the mid-IR beam with a pulse energy of ~ 7 μJ. The remaining part of the seed laser is used as the VIS beam, whose bandwidth is narrowed by passing through a pulse shaper that allows to achieve a bandwidth of $\simeq 10\ cm^{-1}$ with a larger temporal width of 4 ps. The IR (2.5-12 μm) and visible (800 nm) beams, in a co-linear geometry, are spatially and temporally overlapped on the sample stage with an angle of 52° with respect to the surface normal and the SF output signal is spectrally dispersed with a spectrograph and detected by a scientific-grade CCD camera. A schematic view of the setup is showed in figure 1.5.

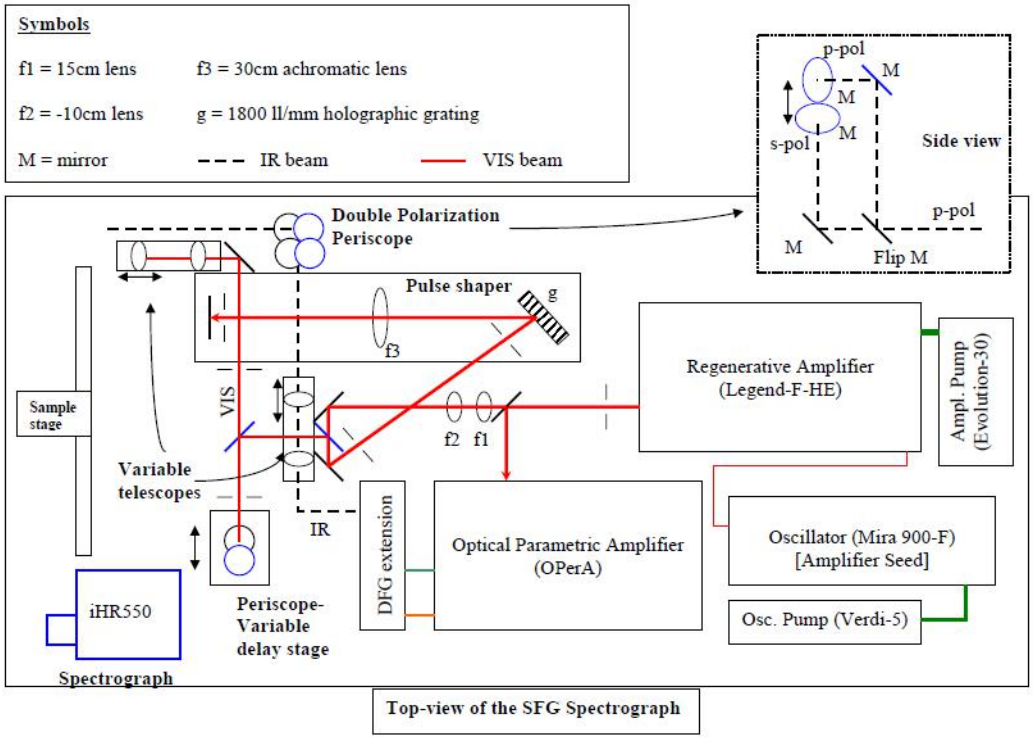

Figure 1.5: BB-SFG scheme

1.5.2 NB-SFG setup

A picosecond Nd:YAG laser (PL2251, 80mJ, 30 ps, 20Hz, EKSPLA) coupled with an harmonics unit (SFGH1000-2H, Ekspla) generates the Vis beam used in the SF-VS setup and the 1064nm and 532nm beams used to generate the IR beam through an Optical Parametric Generator (OPG) coupled with an Optical Parametric Amplifier (OPA). The OPG/OPA system produces parametric radiation at 680-1064 nm (Signal) and 1064-2300 nm (Idler) via non-linear optical process through two BBO crystals. The Idler is then mixed with the funda-

mental radiation to have an IR beam covering the 2.3-10 μm range by Difference Frequency Generation (DFG) in a AgGaS crystal. Both IR and visible beams have a pulse duration of 30 ps and a repetition rate of 20 Hz. The incidence angles with respect to the surface normal are 55° and 60° for the IR and the visible beam, respectively. A basic scheme of the setup is reported in figure 1.6.

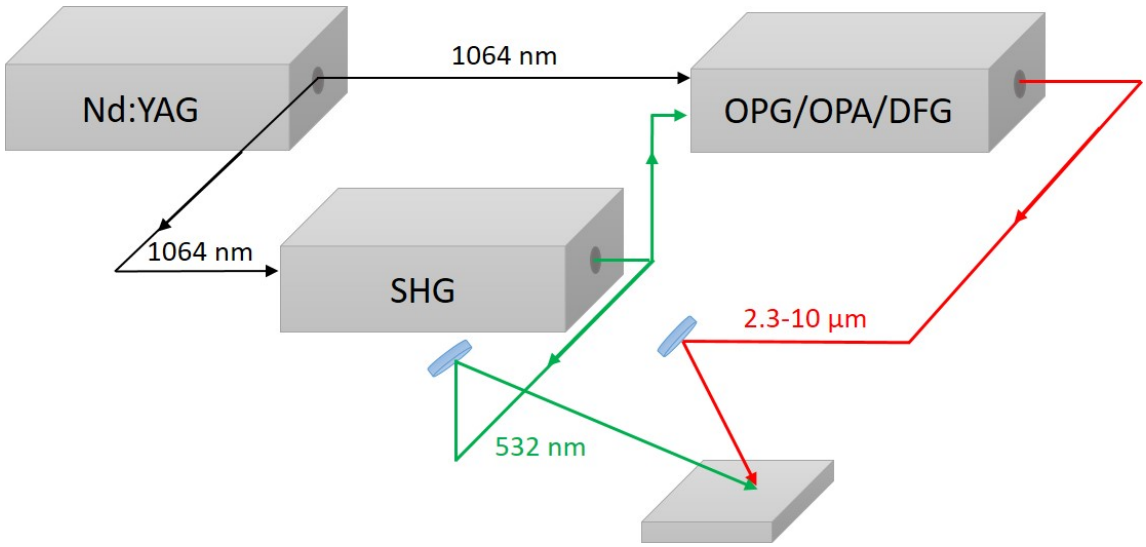

Figure 1.6: NB-SFG setup

1.5.3 Quartz reference

To compare SF spectra with known results in literature, to give a concrete physical meaning to the quantitative analysis, it is pivotal to present the measurements in meaningful units. In many cases it is not a simple operation, because SF intensity depends on the intensities of the impinging beams, detector efficiency, geometry, etc. The SF spectra reported in this thesis are normalized with respect to the SF signal generated by a Z-cut quartz crystal. Due to the lack of inversion symmetry, quartz crystal exhibits a strong non-linear optical response mainly from the bulk. For the normalization of the SF spectra, it is needful to calculate the effective second-order non-linear susceptibility of the quartz crystal. For its D_3 symmetry the non-vanishing

elements of the $\overleftrightarrow{\chi}^{(2)}$ tensor are:

$$\begin{aligned}
&\chi^{(2)}_{xxx} = -\chi^{(2)}_{xyy} = -\chi^{(2)}_{yyx} = -\chi^{(2)}_{yxy} \equiv \chi^{(2)}_{q} \\
&\chi^{(2)}_{xyz} = -\chi^{(2)}_{yxz} \\
&\chi^{(2)}_{xzy} = -\chi^{(2)}_{yzx} \\
&\chi^{(2)}_{zxy} = -\chi^{(2)}_{zyx}
\end{aligned} \tag{1.19}$$

The elements equal to $\chi^{(2)}_q$ are the larger ones and all the other elements will be neglected in the following calculations. The second-order non-linear susceptibility terms in the first row of eq. 1.19 is $\chi^{(2)}_q \approx 1.6 \cdot 10^{-12} m/V$. The effective second-order non-linear susceptibility terms for SSP, SPS and PPP polarization configurations, thus, can be written as follows:

$$\begin{aligned}
&\chi^{(2)}_{eff,SSP} = L_{yy}(\omega_{SF}) L_{yy}(\omega_1) L_{xx}(\omega_2) cos\beta_2 \chi^{(2)}_q l_c \\
&\chi^{(2)}_{eff,SPS} = L_{yy}(\omega_{SF}) L_{xx}(\omega_1) L_{yy}(\omega_2) cos\beta_1 \chi^{(2)}_q l_c \\
&\chi^{(2)}_{eff,PPP} = L_{xx}(\omega_{SF}) L_{xx}(\omega_1) L_{xx}(\omega_2) cos\beta_{SF} cos\beta_1 cos\beta_2 \chi^{(2)}_q l_c
\end{aligned} \tag{1.20}$$

In eq. 1.20 l_c is the coherence length, that in reflection geometry can be calculated as:

$$l_c = \left(2\pi \left(\frac{\sqrt{n(\omega_{SF})^2 - sin^2\beta_{SF}}}{\lambda_{SF}} + \frac{\sqrt{n(\omega_1)^2 - sin^2\beta_1}}{\lambda_1} + \frac{\sqrt{n(\omega_2)^2 - sin^2\beta_2}}{\lambda_2} \right) \right)^{-1}. \tag{1.21}$$

l_c determines the uncertainty range $1/l_c$ in which the momentum conservation needs to be satisfied. In the following tables (1.1 and 1.2) the Fresnel factors and the effective susceptibility elements of quartz crystal are calculated in two different frequency ranges of the IR beam. The calculations have been reported for both the SF setups.

NB scheme	ω_{SF}	ω_1	ω_2
λ[nm]	460	532	3400
n	1.552	1.547	1.490
β	59°	60°	55°
L_{xx}	1.02	1.03	0.99
L_{yy}	0.57	0.56	0.63
$\chi^{(2)}_{eff,SSP} = 0.82 \cdot 10^{-20} m^2/V$			
$\chi^{(2)}_{eff,SPS} = 0.85 \cdot 10^{-20} m^2/V$			
$\chi^{(2)}_{eff,PPP} = 0.70 \cdot 10^{-20} m^2/V$			

BB scheme	ω_{SF}	ω_1	ω_2
λ[nm]	650	800	3400
n	1.543	1.539	1.490
β	52°	52°	52°
L_{xx}	0.94	0.95	0.96
L_{yy}	0.64	0.64	0.65
$\chi^{(2)}_{eff,SSP} = 1.50 \cdot 10^{-20} m^2/V$			
$\chi^{(2)}_{eff,SPS} = 1.53 \cdot 10^{-20} m^2/V$			
$\chi^{(2)}_{eff,PPP} = 1.28 \cdot 10^{-20} m^2/V$			

Table 1.1: Fresnel factors and effective susceptibility elements for Z-cut quartz crystal in the *CH* stretching region for the NB and BB scheme .

NB scheme	ω_{SF}	ω_1	ω_2
λ[nm]	470	532	4400
n	1.552	1.547	1.490
β	59°	60°	55°
L_{xx}	1.02	1.03	0.99
L_{yy}	0.57	0.56	0.63
$\chi^{(2)}_{eff,SSP} = 0.85 \cdot 10^{-20} m^2/V$			
$\chi^{(2)}_{eff,SPS} = 0.88 \cdot 10^{-20} m^2/V$			
$\chi^{(2)}_{eff,PPP} = 0.73 \cdot 10^{-20} m^2/V$			

BB scheme	ω_{SF}	ω_1	ω_2
λ[nm]	680	800	4400
n	1.541	1.539	1.490
β	52°	52°	52°
L_{xx}	0.95	0.95	0.96
L_{yy}	0.64	0.64	0.65
$\chi^{(2)}_{eff,SSP} = 1.57 \cdot 10^{-20} m^2/V$			
$\chi^{(2)}_{eff,SPS} = 1.60 \cdot 10^{-20} m^2/V$			
$\chi^{(2)}_{eff,PPP} = 1.33 \cdot 10^{-20} m^2/V$			

Table 1.2: Fresnel factors and effective susceptibility elements for Z-cut quartz crystal in the *CN* stretching region for the NB and BB scheme.

All the spectra reported in this thesis are normalized with respect to the quartz SF signal according to eq. 1.3 in order to present them in meaningful units [52]:

$$\left(\chi^{(2)}_{eff,sample}\right)^2 = \frac{I_{sample}}{I_{Qz}} \cdot \left(\chi^{(2)}_{eff,Qz}\right)^2 \tag{1.22}$$

where I_{sample} and I_{Qz} are the SF intensities from the sample and from the quartz crystal, respectively, while $\chi^{(2)}_{eff,sample}$ and $\chi^{(2)}_{eff,Qz}$ are the corresponding nonlinear susceptibilities.

Chapter 2

Cavitand–Organosilane Hybrid Bilayers

2.1 Synthetic receptors for chemical sensing

Molecular recognition in living systems is involved in the most important cellular mechanisms such as catalysis, transport of nutrients and ions inside the cell and synthesis of DNA. All these processes are ruled by specific chemical interactions between molecular receptors and ligands. In supramolecular chemistry the molecular containers are synthetic cavities that mimic the specificity, selectivity and geometry of receptor binding sites in Nature [53]. The ambitious goal of being able to design receptors of desired size, shape and chemical properties has led in recent years to the synthesis of a wide range of compounds which may find application in chemistry, medicine, biology and pharmacology [10, 54–58]. They can act as "nanometer-size" cups, flasks and bottles [59] for chemical sensing applications, drug delivery, environmental monitoring, prevention of biological risks and preventive diagnosis of diseases. Molecular containers are mainly synthesized starting from calixarenes, resorcinarenes and their relatives [60, 61]. Beyond the differences in size, shape and chemical properties, all the molecular containers are characterized by a concave surface to entrap guests. Properties and behavior of these molecules can be monitored with conventional techniques such as NMR and X-rays, but the study of the host-guest interactions at the interface is required in order to understand the mechanisms between the receptor and the ligand at the molecular scale. For this reason, a nonlinear optical technique as SFVS can provide, at the same time, information about the organization of receptors and molecular recognition at the interface, with an *in-situ* and noninvasive analysis yields valuable information that can lead to a more rational synthesis of receptors in order to improve their entrapment capabilities of guests. Among all these classes of synthetic receptors, this thesis will be focused on the understanding of conformation, selectivity and sensitivity of *cavitand* films at interfaces.

2.2 Cavitands as supramolecular receptors

Cavitands are organic hosts with an open-ended enforced cavity [62] of molecular dimension able to engulf specific classes of ligands with which they have strong chemical affinity and complementarity in size and shape [1, 3, 63, 64]. Complexes of cavitands are called *caviplexes*. One of the most common protocol to synthesize cavitands involves the extension of the aromatic walls of resorcinarene, as happens for the quinoxaline cavitand (QxCav) reported in image 2.1. QxCav has a lipophilic cavity large enough to entrap aromatic guests as

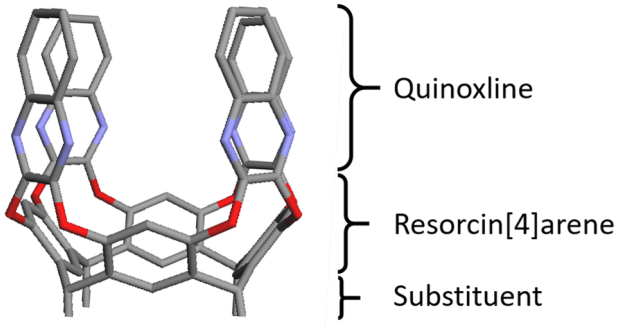

Figure 2.1: Structure of quinoxaline cavitand from X-ray diffraction analysis.

demonstrated in reference [60], where X-Ray structure of QxCav and its complex is reported. The binding energy for aromatic guests is $2-3\,kcal\,Mol^{-1}$ and it is due to weak interactions such as hydrogen bonding, $CH-\pi$, $\pi-\pi$ and cation-dipole interactions (fig. 2.2). In order to stabilize the cavitand structure, hydrogen bonding is used to favor the vase-conformation and to avoid opening of the walls, therefore creating an energy barrier that prevents the release of the guests. This fact makes QxCav a molecule with a switchable structure, that can change its conformation with an external control such as temperature, pH or both. As shown in references [37, 38, 65], the *vase-to-kite* conformational switch of QxCav has been observed by changing the pH of the water solution. This property also opens to a large area of applications, because a controlled release of the guests with external factors can be achieved [34]. A great number of works about QxCav have been reported in literature. Its strong selectivity toward airborne aromatic hydrocarbons at ppb levels [2] makes it a good candidate for a thorough detection of the most common pollutants in air such as benzene, toluene, ethylbenzene and xylene (BTEX).

Different QxCav derivatives have been synthesized specifically to increase their selectivity toward other classes of aromatic guests. For example, a carboxylic group $COOH$ at the upper rim can increase the efficiency of complexation of nitro-aromatic volatile compounds, denoting the presence of TNT, due to the formation of an additional H-bonding interaction with the NO_2 group [66] as showed in fig. 2.4-a . Recently, a QxCav derivative for selective detection

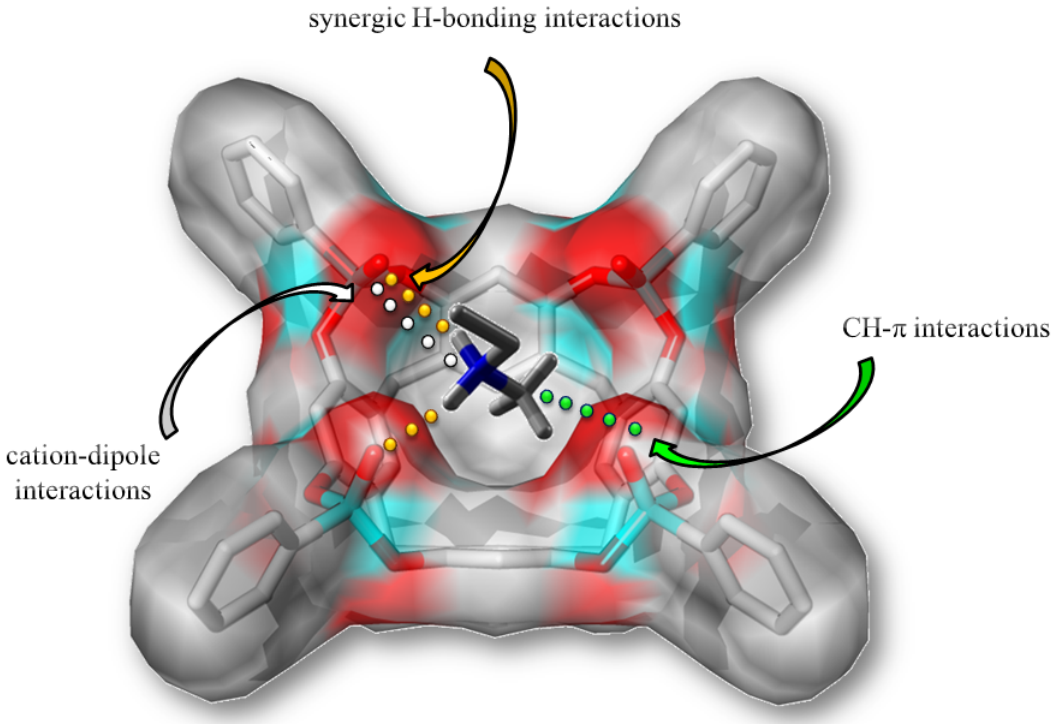

Figure 2.2: Weak interactions involved in the recognition event.

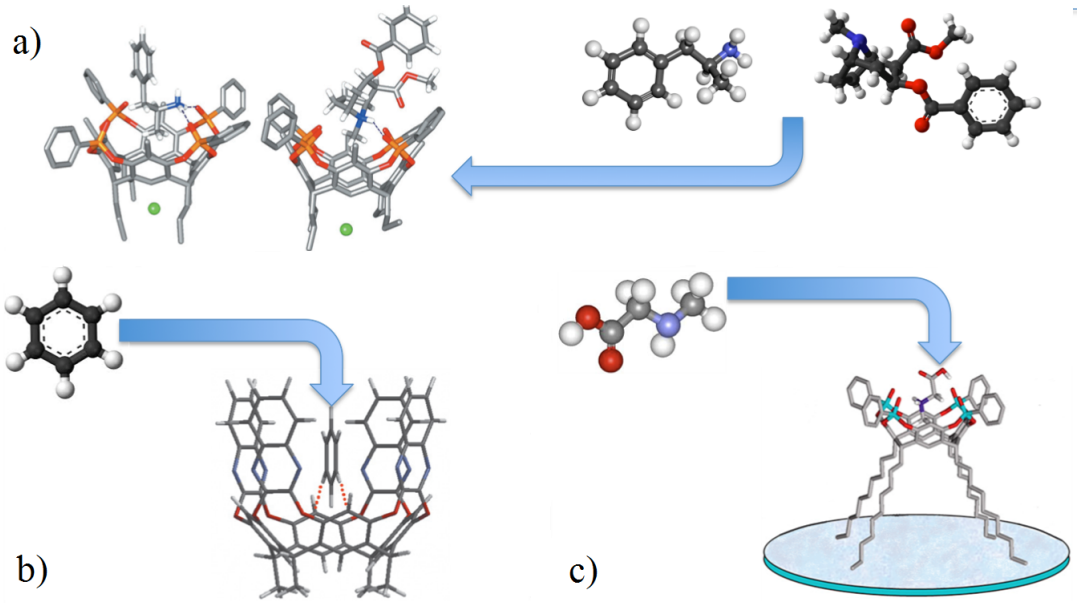

Figure 2.3: Representation of host-guest interactions between a) phosphonate cavitand and common illicit drugs [1], b) QxCav and benzene [2] and c) phosphonate cavitand and sarcosine [3].

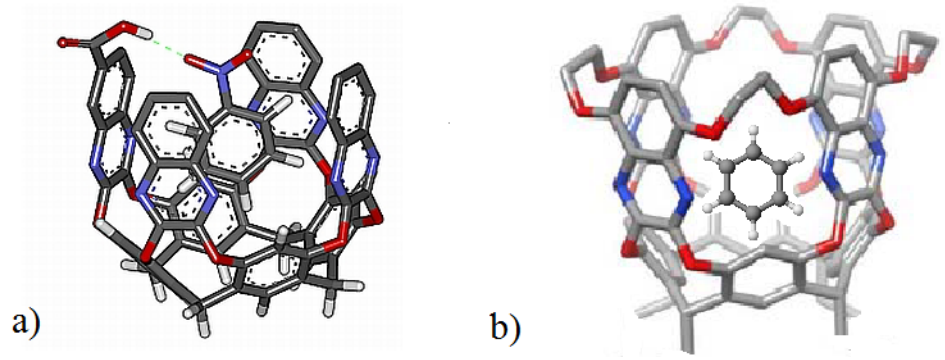

Figure 2.4: Complexation of a) nitrobenzene in COOH-QxCav cavity and b) benzene inside the conformtionally-blocked cavity mouth of the Et-QxBOX.

of BTEX compounds, namely QxBOX, has been synthesized. Its fixed walls, that do not allow the vase-to-kite switch, form a rigid structural arrangement due to aliphatic linkers that tighten the cavity mouth. The rigidity of structure guarantees a more efficient entrapment of the guest molecules (see fig. 2.4-b).

However, for the recognition of compounds as inorganic cations, methylammonium and pyridinium salts, neutral molecules and alchools, tetraphosphonate cavitands (Tiiii) have proven a remarkable versatility, especially in the aqueous phase[6, 67]. This results, for example, in potential medical application for the detection of amino acid such as sarcosine [3], whose high levels in the urine can be a symptom of prostate cancer [68].

This chapter will be devoted to the conformational study of QxCav film at air/solid interface.

2.3 Solid Supported Hybrid Bilayer (SSHB)

A crucial step toward real sensing application of chemical receptors consists in their integration on a proper solid support in order to be able to study their complexation capabilities in air or liquid phase, with a particular attention on the efficiency of selective interactions and sensitivity at very low concentrations of target molecule. Hybrid molecular architectures that mimics the properties of biological systems are of great interest for the study of membranes [69], micelles [70] and vesicles [71]. In this regard, instead of covalent grafting of cavitands onto solid surfaces [1, 63, 64, 72], an alternative approach was pioneered. To realize a SSHB, a QxCav layer was transferred on a solid support covered with a hydrophobic self-assembled monolayer (SAM) of organosilane molecules. The surfactants, whose head group covalently attaches to a substrate (i.e. fused silica, quartz, gold, silicon ...), form a well ordered and

packed molecular film (fig. 2.5). To be able to anchor the QxCav receptors on the SAM, the hydrophobic interactions between the QxCAv chains and the SAM have been exploited.

The selectivity and the sensitivity of the QxCav organized in such hybrid bilayer system can be affected by the molecular density of receptors and their conformations. In this regard, a technique as SFVS is preferred to other ones, because it offers the possibility to obtain all the chemical and structural information about receptors, if properly organized, directly at the interface. In other words, the investigation of QxCav conformation at air/solid interface is a crucial step to understand how molecular architecture of receptors can affect sensing capabilities of the sensitive layer. For the hydrophobic template, a SAM of *Octadecyltrichlorosi-*

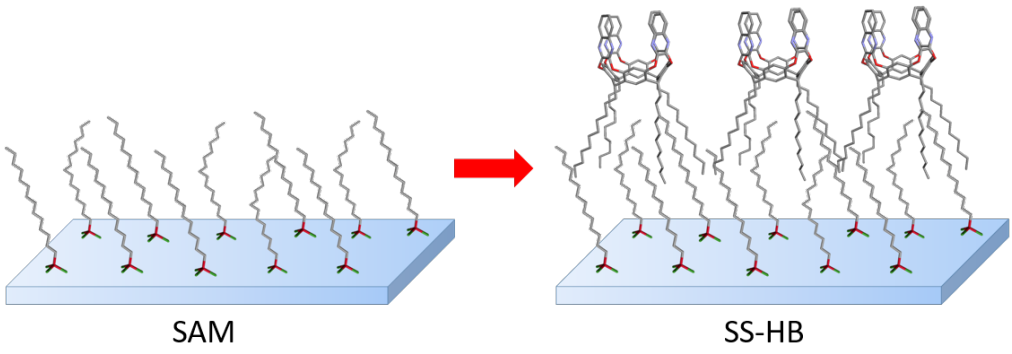

Figure 2.5: Hydrophobic SAM and SS-HB of QxCav on fused silica

lane (OTS) on fused silica is realized. OTS is an amphiphilic molecule with a long alkyl chain ($C_{18}H_{37}-$) and a polar head group ($SiCl_3-$) which has been widely studied in SF spectroscopy and provides a benchmark for the stretching of the aliphatic CH groups in the region $2800-3000\,cm^{-1}$ [29, 73, 74].

The optically polished fused silica substrates (NHI-1200, Helios Italquartz s.r.l.) were first cleaned with acetone and then soaked for 24 h at room temperature in an oxidizing acid solution, that is, a mixture of a solid oxidizer (NoChromix, Godax Laboratories) and concentrated sulfuric acid (95-98%, Sigma-Aldrich), to remove organic and inorganic contaminants from the surface. The substrates were then rinsed thoroughly with ultrapure water ($18.2M\Omega \cdot cm@25°C$, Synergy UV Millipore) and blown dry with a jet of nitrogen. The activation of the hydroxyl groups of the glass surface was finally performed with a plasma-cleaner for 8 minutes. The hydroxylated substrates were immersed in a 2 mM solution of OTS ($CH_3(CH_2)_{17}SiCl_3$, 90%, Sigma-Aldrich) in hexane (90%) and chloroform (10%) for 10 minutes, then exposed to air for 5 minutes and finally baked in an oven at 120 °C for 45 minutes in order to promote cross-linking between molecules and covalent bond formation with the surface. The substrate was left to cool to room temperature and then was soaked in an

ultrasonic bath in chloroform for 10 minutes to remove all the excess of OTS molecules that are not covalently bonded to the surface.
In addition to the OTS template, a different hydrophobic monolayer was arranged on the bare fused silica substrate using a different surfactant called *N,N-dimethyl-N-octadecyl-3-aminopropyltrimethoxysilylchloride* (DMOAP, $CH_3(CH_2)_{17}(CH_3)_2N^+(CH_2)_3Si(CH_3O)_3Cl-$, 72% in methanol, Sigma-Aldrich). This compound has an alkyl chain of the same length of the OTS but a larger polar head. The main goal is to compare two different hydrophobic templates with different peculiarities (as molecular density and conformation of the alkyl chains) and put in evidence differences in the transfer of the receptor layer and its conformation in relation to the underlayer. For this reason the protocol optimized for the production of the OTS film was extended to the case of DMOAP [75].
To assemble the SS-HB, a film of QxCav is transferred on the hydrophobic substrates (both OTS and DMOAP) adopting a Langmuir-Scheafer deposition procedure. To favor the formation of a compact monolayer of receptors at the air/water interface of a commercial Langmuir Trough (KSV NIMA), few drops of a 1 μM solution of QxCav in chloroform were spread on the water subphase. The QxCav molecules, being amphiphilic, are oriented with their alkyl chains pointing to the gas phase and with the polar head towards the aqueous phase. After waiting for 30 minutes the solvent was completely evaporated, the QxCav film was compressed until it reached the liquid-condensed phase (2.6) at a surface pressure of 20 mN/m.

The hydrophobic templates were then put in contact with the film of $C_{11}H_{23}-$footed QxCav molecules for 5 minutes (2.7-a) and afterwards the samples were slowly raised up by compressing the barriers to maintain a constant surface pressure. Due to the dispersion interactions among alkyl chains, part of the Langmuir film is transferred on the hydrophobic substrate 2.7-b. The coverage percentage of the sample with the QxCav monolayer can be estimated from the area of the Langmuir trough before and after the deposition and comparing it with the one of the substrate. Therefore, it is possible to estimate a coverage of about 10% and 25% for the OTS and the DMOAP templates, respectively.

2.4 Molecular architecture at air/solid interface

In this section the molecular architectures of both OTS and DMOAP templates and their corresponding SSHBs have been deduced from the study of SF spectra and compared with the complementary results obtained with other investigation techniques. The information deduced from SF measurements allows to reconstruct a more complete physical picture of such systems, elucidating the conformation of receptors at the interface in relation to different tem-

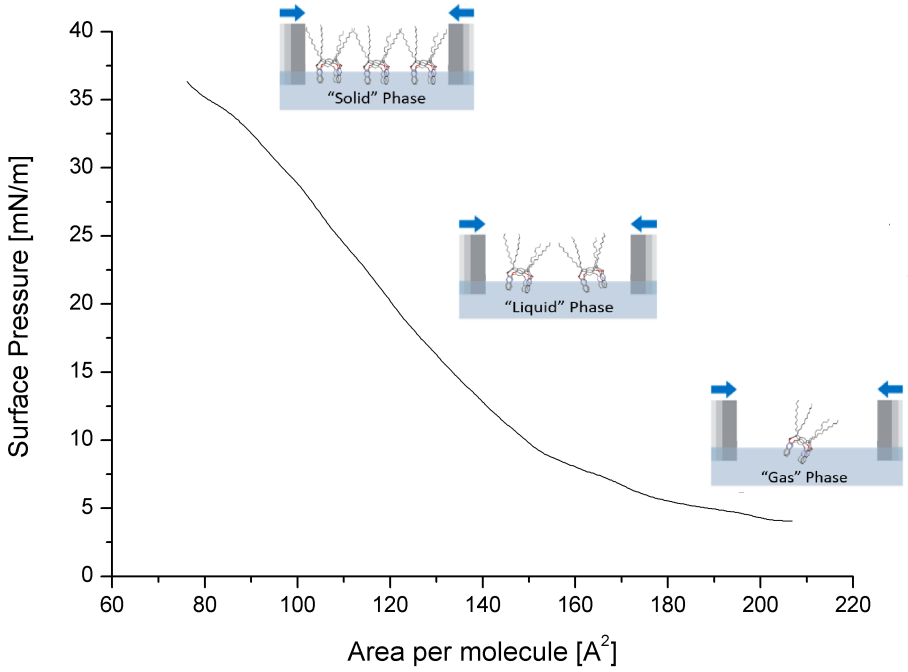

Figure 2.6: Isotherm of a Langmuir film of QxCav molecules

plates.

2.4.1 Characterization of OTS and DMOAP templates

Static contact angle measurements were performed on both DMOAP and OTS templates to appreciate the quality of the silanized fused silica substrates. The hydrophilic bare glass showed a contact angle of $21° \pm 2°$, typical of hydroxylated surfaces [76]. Because of their strong hydrophobic behavior, surfactant-coated substrates showed contact angles of $91° \pm 2°$ and $102° \pm 2°$ for DMOAP and OTS, respectively. These measurements are comparable with those of compact monolayers, whose theoretical densities are $3.5\, chains/nm^2$ and $2.5\, chains/nm^2$ for OTS and DMOAP SAM, respectively. [22, 29, 31]. These values of contact angles suggest, thus, the formation of monolayers with high coverage for both SAMs.

The silanized substrates were morphologically characterized by Atomic Force Microscopy (AFM) in air by a Nanoscope IIIa (Bruker, CA) operating in tapping mode. Silicon probes (Bruker, CA) with resonance frequency 150-300 kHz, cantilever length $125\,\mu m$ and tip radius of curvature $10\,nm$, were used. DMOAP and OTS templates 2.8-a,b exhibit a similar behavior with a quite uniform morphology, except for the small agglomerates on the DMOAP surface with size of few tens of nm and height of $\simeq 6\,nm$. The measured roughness, $0.45\,nm$ for

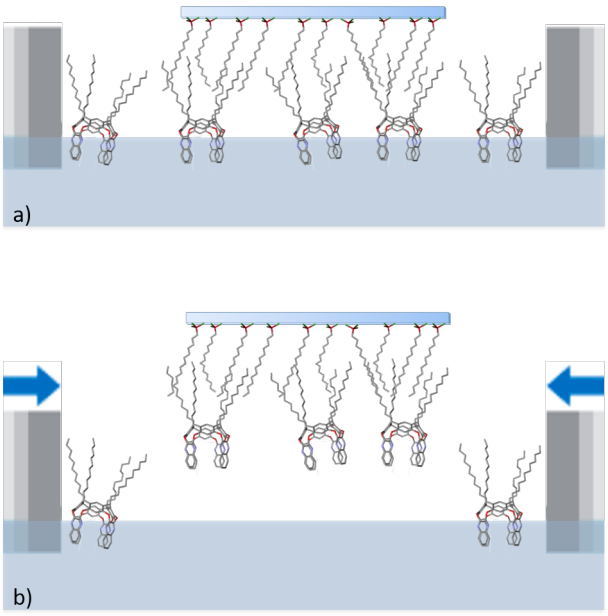

Figure 2.7: Langmuir-Scheafer procedure for deposition of QxCav film on hydrophobic monolayer deposited on fused silica

DMOAP and 0.25 nm for OTS template, proves the homogeneity of the organosilane SAMs as assumed after the preliminary contact angle measurements. The SFG characterization has been carried out with the SFG-BB scheme (1.5.1) in the spectral range of the aliphatic CH stretch ($2800-3000\,cm^{-1}$) in order to deduce the conformation of alkyl chains. In fig. 2.9 the SF spectra of both OTS (in black) and DMOAP (in red) are reported for SSP, SPS and PPP polarization configuration. The five peaks in the spectra are related to the symmetric stretching ($2851\,cm^{-1}$, d^+) and antisymmetric stretching ($2918\,cm^{-1}$, d^-) stretch mode of the methylene (CH_2) groups, and the symmetric ($2877\,cm^{-1}$, r^+), antisymmetric ($2964\,cm^{-1}$, r^-) and Fermi resonance ($2942\,cm^{-1}$, r^+_{FR}) of the methyl groups. The break of the centrosymmetry along the chains, due to the formation of *gauche* defects, makes the CH_2 modes visible in the SFVS. The presence of more prominent CH_2 resonances for the DMOAP template is indicative of a higher disorder of the alkyl chains with respect to the OTS template. In a first qualitative description, the OTS monolayer seems to be more ordered, fully-packed and with most of the alkyl chains in an *all-trans* configuration, as the virtually absent methylene resonances suggest. In addition to this first experimental evidence, the methyl symmetric stretch $r^+$is more prominent in the SSP spectrum than in the SPS one, hinting a net polar orientation of the methyl group with its main axis close to the surface normal. Deducing the average orientation of the methyl group can help to trace back, in a more quantitative way, to the conformation of the alkyl chains. This is physically relevant in the case of the OTS template, while it is trickier for the DMOP case,

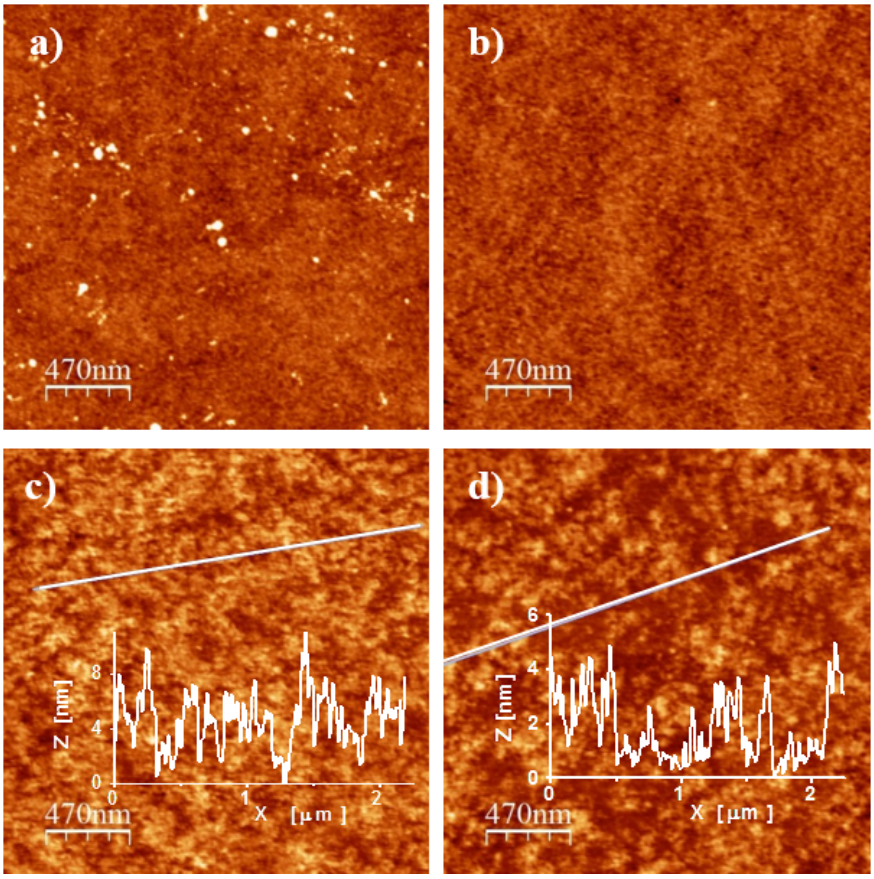

Figure 2.8: AFM images ($2 \times 2\,\mu m^2$) of a) DMOAP, b) OTS, c) DMOAP-QxCav and d) OTS-QxCav that show the topography of the samples.The height profiles in panel c and d were measured for the SSHBs along the white line.

where the presence of a high number of *gauche* defects does not allow to relate the average orientation of the methyl group with the one of the whole molecule.

To figure out the average orientation of the CH_3 group for the two templates, the resonant amplitudes $A_{q,ijk}$ in lab coordinates must be related to their counterparts $a_{q,lmn}$ in molecular coordinates. Through an opportune coordinate transformation and supposing an orientational distribution function (ODF) $f(\Omega)$ for the methyl group, the eq. 1.10 can be written as:

$$A_{q,ijk} = N_S \int \sum_{lmn} a_{q,lmn} \left(\hat{i}\cdot\hat{l}\right)\left(\hat{j}\cdot\hat{m}\right)\left(\hat{k}\cdot\hat{n}\right) f(\Omega)\, d\Omega \tag{2.1}$$

where $\Omega = (\phi, \theta, \psi)$ indicates the Euler angles. From data fit, the resonant amplitudes can be deduced and related to their theoretical values in order to obtain the angles and thus the average orientation of the methyl group. For the r^+ vibrational mode, three resonant amplitudes are necessary to get the average orientation of the group, because of the C_∞ symmetry of the OTS

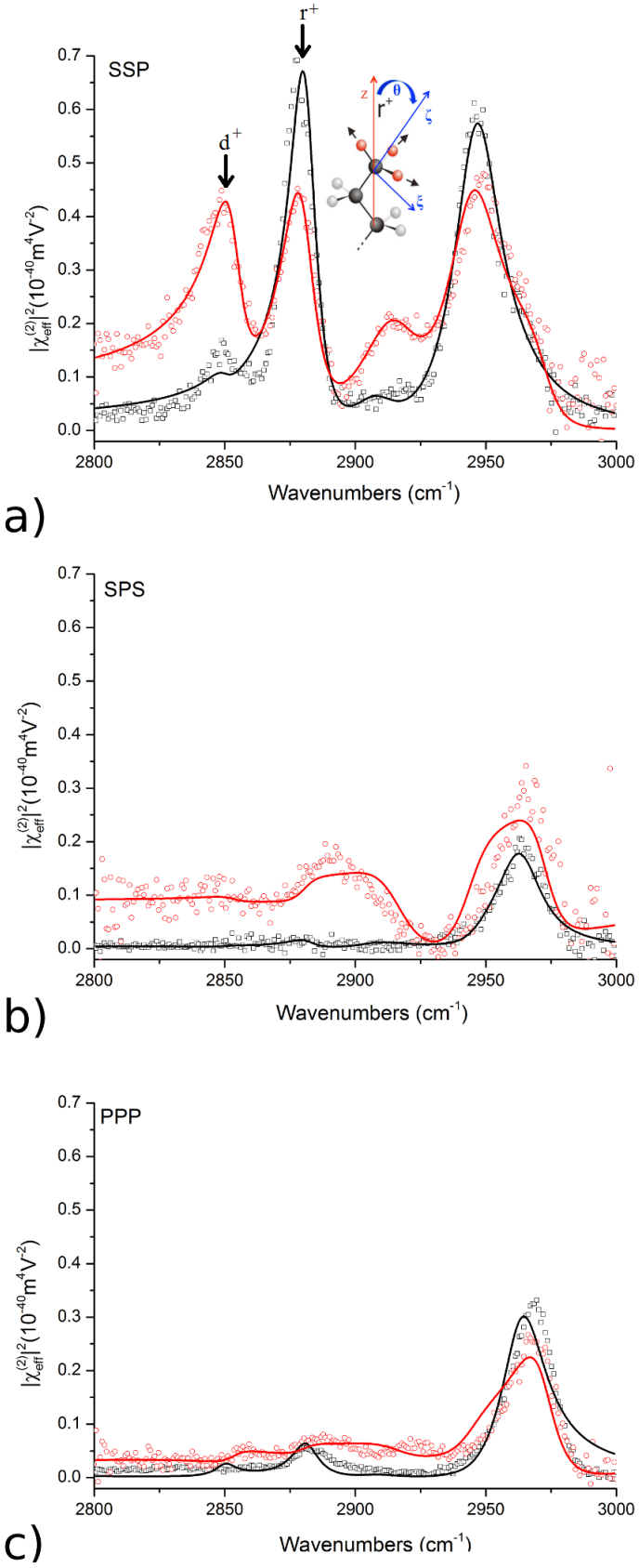

Figure 2.9: SFG spectra (scatters) and relative curve fits (solid line) of OTS (in black) and DMOAP (in red) templates in the aliphatic *CH* stretching region. The inset in fig. a) shows the symmetric stretch of the methyl group with the net dipole moment along ζ axis, forming an angle θ with respect to the Z axis in the lab frame.

and DMOAP templates. These terms can be written through eq. 2.1 as:

$$\begin{aligned} A_{r^+,xxz} &= \frac{1}{2} N_{CH_3} \alpha_{r^+,\zeta\zeta\zeta} \left[(1+r_{r^+}) \langle cos\theta \rangle - (1-r_{r^+}) \left\langle cos^3\theta \right\rangle \right] \\ A_{r^+,xzx} &= \frac{1}{2} N_{CH_3} \alpha_{r^+,\zeta\zeta\zeta} (1-r_{r^+}) \left[\langle cos\theta \rangle - \left\langle cos^3\theta \right\rangle \right] \\ A_{r^+,zzz} &= N_{CH_3} \alpha_{r^+,\zeta\zeta\zeta} \left[r_{r^+} \langle cos\theta \rangle + (1-r_{r^+}) \left\langle cos^3\theta \right\rangle \right] \end{aligned} \tag{2.2}$$

where r_{r^+} is the depolarization ratio for the symmetric stretch of the CH_3 group, θ is the polar angle in Euler notation, N_{CH_3} is the surface density of the methyl groups and the angular brackets represent the ensemble average over the ODFs f(Ω). These theoretical expressions must be compared with their corresponding experimental values deduced from the fit of the data through the relations 1.13.

The Fresnel factors for the organosilane monolayers on fused silica substrates are reported in tab. 2.1, where a surface refractive index $n' = 1.21$ [48] has been considered. The theoretical

BB-scheme	$\lambda\,(nm)$	$\beta\,(deg)$	n	L_{xx}	L_{yy}	L_{zz}
ω_{SF}	650	52	1.457	0.98	0.67	0.70
ω_1	800	52	1.453	0.97	0.67	0.70
ω_2	3400	52	1.409	0.98	0.69	0.70

Table 2.1: Fresnel factors for organosilane monolayers on fused silica substrates.

curves of the amplitude ratios $A_{r^+,SPS}/A_{r^+,SSP}$ and $A_{r^+,PPP}/A_{r^+,SSP}$ are reported in fig. 2.10 as a function of the polar angle θ in the simple case of Dirac delta ODF for a value of the depolarization ratio $r_{r^+} = 2.2$ (as valued in expression 1.18). The amplitude ratios showed in fig. 2.10 give an idea on their dependence from the polar angle. Instead of a Dirac delta ODF, a more realistic distribution, as the one shown in eq. 2.3, is assumed:

$$\begin{cases} f(\theta) = \frac{1}{4\pi^2(\cos\theta_{min} - \cos\theta_{max})} & \text{for } \theta_{min} \leq \theta \leq \theta_{max} \\ f(\theta) = 0 & \text{elsewhere} \end{cases} \tag{2.3}$$

where isotropic distribution is assumed for ψ and ϕ angles. With the experimental amplitudes listed in tab. 2.2 for the r^+ mode through the eq. 1.13, the calculated values for the polar angle are $0° \leq \theta_{CH_3,OTS} \leq 54°$ and $30° \leq \theta_{CH_3,DMOAP} \leq 87°$ for the OTS and DMOAP template, respectively. For the OTS monolayer, because of the predominant *all-trans* configuration of the alkyl chains, the orientational information obtained for the methyl groups can be used to deduce those of the OTS molecules. Considering the average value $\left\langle \theta_{CH_3,OTS} \right\rangle \simeq 36°$ and

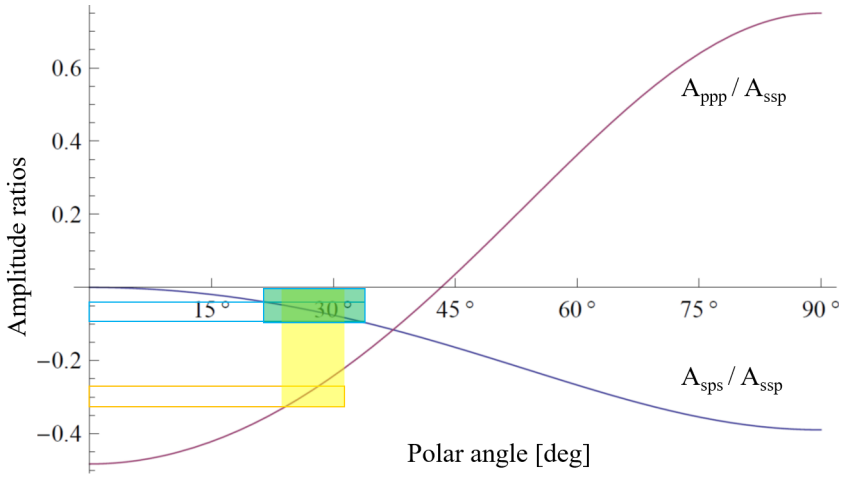

Figure 2.10: Amplitude ratios $A_{r^+,SPS}/A_{r^+,SSP}$ (in blue) and $A_{r^+,PPP}/A_{r^+,SSP}$ (in purple) for the r^+ mode as a function of the polar angle θ in the simple case of Dirac delta ODF. Green and yellow area represent the experimental ranges for OTS SAM.

that the methyl group forms an angle of about 35° with the main axis of the molecule [28], it is reasonable to conclude that the OTS molecules are mostly in a straight configuration with their axis close to the surface normal. The larger polar angle range of the methyl groups for the DMOAP SAM, with an average value of $\langle \theta_{CH_3,OTS} \rangle \simeq 63°$, and the more prominent methylene resonance d^+ in the SSP spectrum, are evidence of a larger density of gauche defects in the alkyl chains.

OTS	$\omega\,[cm^{-1}]$	$\Gamma\,[cm^{-1}]$	A_{SSP}	A_{SPS}	A_{PPP}	DMOAP	$\omega\,[cm^{-1}]$	$\Gamma\,[cm^{-1}]$	A_{SSP}	A_{SPS}	A_{PPP}
d^+	2850	5	0.2	0.1	0.9	d^+	2854	7.3	2.5	0.1	-0.3
r^+	2881	6.4	4.6	-0.6	-1.5	r^+	2881	8.1	4.0	-0.4	0.3
d^-	2908	12	1.7	-1.3	-0.6	d^-	2916	15	4.4	3.1	0.8
r^+_{FR}	2946	11	8.3	-1.4	0.4	r^+_{FR}	2944	13	7.9	-3.4	-1.3
r^-	2963	11	0.2	4.8	-5.7	r^-	2972	10	-4.4	2.8	4.1

Table 2.2: Fit parameters for the OTS and DMOAP template

From this analysis it is also possible to assess the ratio between the surface densities of the two templates $N^{DMOAP}/N^{OTS} \simeq 0.7$ by the direct comparison between the corresponding amplitudes $A_{r^+,xxz}$ through eq. 2.2 and the ODF. The reason for such difference is due to the different size of the polar head, that is bigger in the case of DMOAP molecule. This implies a lower surface density of the alkyl chains for the DMOAP template that favors a more disordered configuration and promotes the formation of a larger number of *gauche* defects.

2.4.2 SS-HBs: orientation of receptors at interface

After the organosilane template characterization, a monolayer of QxCav was transferred by LS procedure on top of both OTS and DMOAP coated substrates. A preliminary AFM analysis (2.8-c,d) showed a different morphology after the deposition of cavitand films. For both OTS-QxCav and DMOAP-QxCav samples the roughness increases to $1.2\,nm$ and $2.0\,nm$, respectively. Moreover, the analysis revealed the presence of island-like structures for both SAMs, demonstrating the fact that the outermost QxCav layer is not perfectly uniform. In the inset of fig. 2.8 the height profiles are in agreement with the nominal length of the QxCav molecule (2.4 nm), endorsing the hypothesis of a single layer coating for the most of the surface. In fig. 2.11 the SF spectra of the OTS-QxCav and DMOAP-QxCav bilayers in the range $2800-3100\,cm^{-1}$ are reported. Up to $3000\,cm^{-1}$ all the stretching modes of both methyl and methylene groups are present as in the case of bare SAMs in fig. 2.9. In addition to these, two new resonances appear at 3024 (ν_7) and $3064\,cm^{-1}$ (ν_2), relative to the aromatic *CH* stretching modes of the quinoxaline wings [75, 77]. By a first qualitative comparison with the spectra of SAMs (see fig. 2.12), there are no significant changes in the part of the spectra relative to the vibrational modes of the methyl and methylene groups. This may be due to the low density of the cavitand films on both SAMs and to the high disorder of QxCav chains (as shown in ref. [38], due to the shorter chain length with respect to the organosilane ones). This clarification is necessary because, in a configuration in which the cavitand layer was compact and with all the alkyl chains in straight configuration, the SF signals of the methyl groups of QxCav layer (pointing downward) and SAM (pointing upward) should cancel each other. At a closer look, it is possible to notice an increased intensity of the d^+ mode for the OTS-QxCav sample in SSP spectrum due to a higher disorder of the alkyl chains introduced by the QxCav layer. The DMOAP-QxCav sample, on the contrary, exhibits an overall increasing of the signal probably due to the increased total density of the more disordered alkyl chains. In addition to the conformational information of the alkyl chains, the aromatic ν_2 peak (relative to the total symmetric *CH* stretch of the quinoxaline wings) appears more prominent in the case of DMOAP template. This experimental evidence suggests a higher cavitand transfer on the DMOAP monolayer, in which the lower surface density could favor a more efficient intercalation of the QxCav chains.

All these arguments are supported by the quantitative analysis over the ν_2 mode, to deduce the average orientation of the receptor layer. In tab. 2.3 the fit parameters of both OTS-QxCav and DMOAP-QxCav bilayers for the SF spectra in fig. 2.11 are reported. Carrying out a similar analysis to the previous r^+case, through eq. 2.1 the amplitudes for the ν_2 mode of the

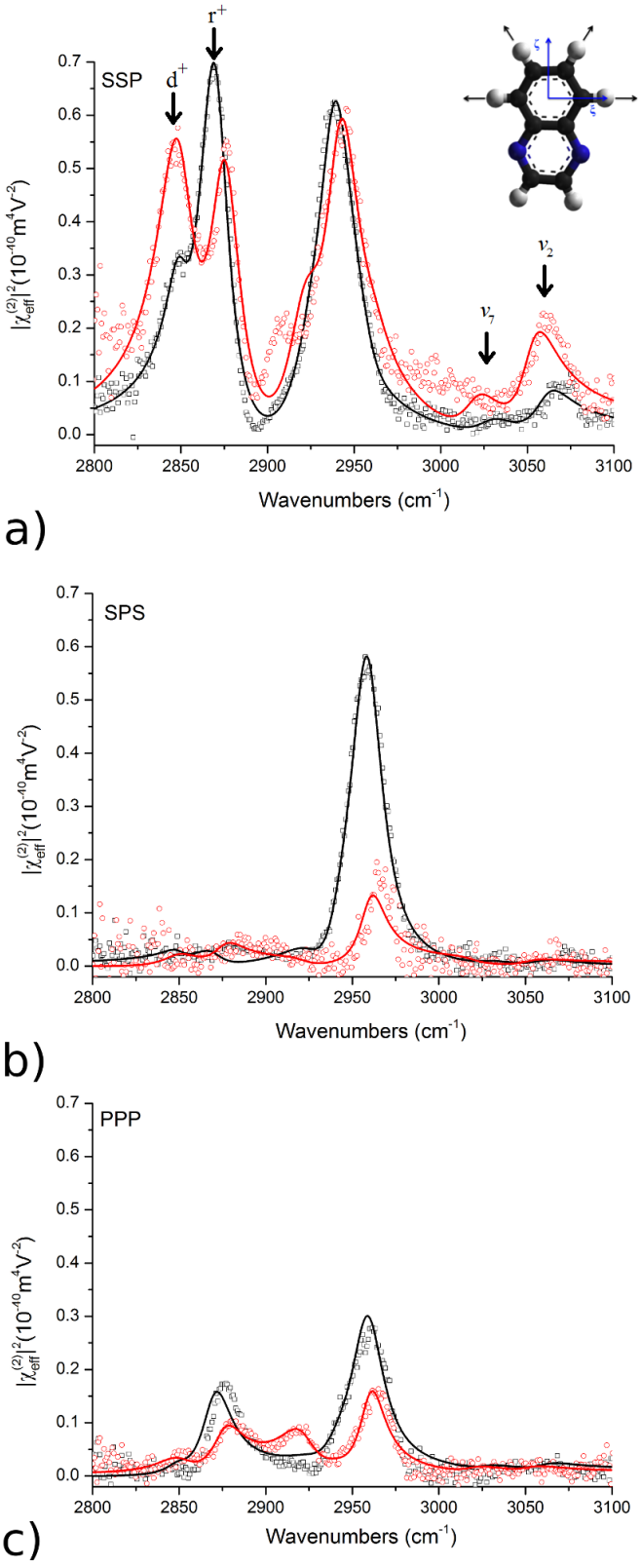

Figure 2.11: SFG spectra (scatters) and relative curve fits (solid line) of OTS-Qx (in black) and DMOAP-Qx (in red) SS-HB in the *CH* stretch (aliphatic and aromatic) region. The inset in fig. a) shows a quinoxaline wing in the molecular frame and its symmetric *CH* stretching mode ν_2.

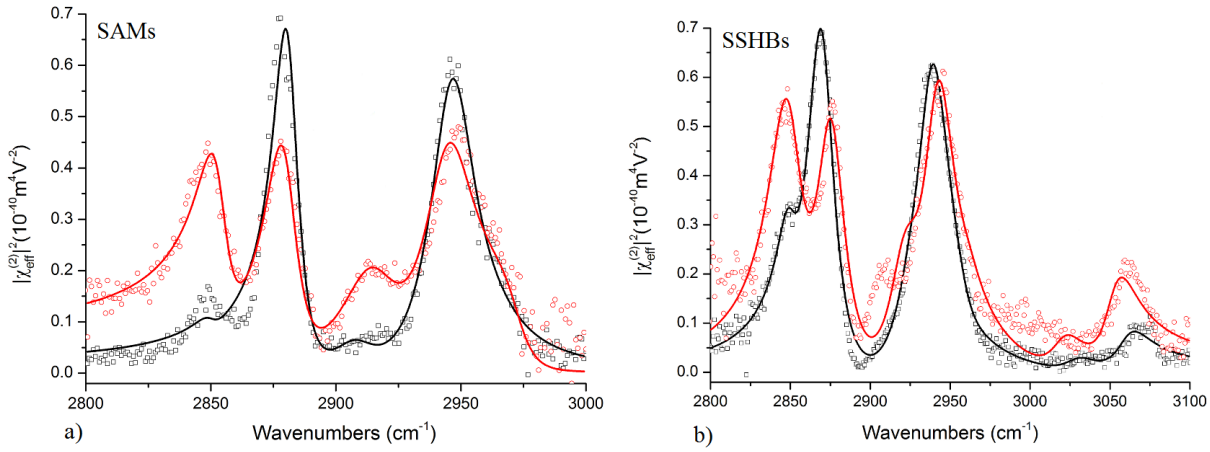

Figure 2.12: SSP spectra of: a) OTS (black markers) and DMOAP SAMs (red markers) and b) OTS/QxCav (black markers) and DMOAP/QxCav (red markers) SSHBs. Solid lines are the corresponding best curve fits.

OTS-Qx	$\omega\,[cm^{-1}]$	$\Gamma\,[cm^{-1}]$	A_{SSP}	A_{SPS}	A_{PPP}
d^+	2850	7.8	1.4	0.4	-0.5
r^+	2870	11	7.8	1.1	-3.8
d^-	2925	13	2.0	1.0	1.1
r^+_{FR}	2938	13	8.1	-2.1	3.9
r^-	2958	11	-0.9	8.6	-6.9
ν_2	3024	10	1.1	0.4	0.4
ν_7	3062	12	2.4	0.7	0.5

DMOAP-Qx	$\omega\,[cm^{-1}]$	$\Gamma\,[cm^{-1}]$	A_{SSP}	A_{SPS}	A_{PPP}
d^+	2852	12	-5.6	-0.6	-2.1
r^+	2878	11	-6.1	-1.0	-2.5
d^-	2926	13	-4.1	-2.0	1.7
r^+_{FR}	2944	12	-7.0	1.1	-0.1
r^-	2965	12	-1.1	-4.4	4.5
ν_2	3024	10	2.0	0.2	0.8
ν_7	3062	12	-5.0	-1.2	1.2

Table 2.3: Fit parameters for the OTS-Qx and DMOAP-Qx SS-HB.

quinoxaline wings can be written as follows [38]:

$$
\begin{aligned}
A_{\nu_2,xxz} &= \frac{1}{8} N_{Qx} a_{\nu_2,\xi\xi\zeta} \left\langle \cos\theta \left[3 + \cos 2\theta + 2\sin^2\theta \left(2r_{\nu_2} - \cos 2\psi\right)\right]\right\rangle \\
A_{\nu_2,xzx} &= -\frac{1}{4} N_{Qx} a_{\nu_2,\xi\xi\zeta} \left\langle \cos\theta \sin^2\theta \left(1 - 2r_{\nu_2} + \cos 2\psi\right)\right\rangle \\
A_{\nu_2,zzz} &= N_{Qx} a_{\nu_2,\xi\xi\zeta} \left\langle \cos\theta \left(\cos^2\psi \sin^2\theta + r_{\nu_2}\cos^2\theta\right)\right\rangle
\end{aligned}
\tag{2.4}
$$

where the angles θ and ψ are the polar and the torsion Euler angle, respectively [75] and N_{Qx} is the surface density of the quinoxaline moeties. $r_{\nu_2} = a_{\nu_2,\zeta\zeta\zeta}/a_{\nu_2,\xi\xi\zeta} = 2.4$ [38] is the depolarization ratio for the quinoxaline moiety expressed in the group frame (ξ,η,ζ), whose hyperpolarizability tensor has only two nonvanishing independent terms. In the following

calculations, an ODF as the one reported in eq. 2.5 was assumed, considering an isotropic distribution for the ϕ angle:

$$\begin{cases} f(\Omega) = \frac{\delta\left(\psi - \pi/2\right)}{2\pi(\cos\theta_{min} - \cos\theta_{max})} & \text{for } \theta_{min} \leq \theta \leq \theta_{max} \\ f(\Omega) = 0 & \text{elsewhere} \end{cases} \tag{2.5}$$

The ψ angle was fixed to $\pi/2$, according to the symmetry of the QxCav molecule, as shown in fig. 2.13-a. It is pivotal to specify that in the model chosen to derive eq. 2.4, QxCav molecules are supposed to have their main axis perpendicular to the surface and the angle θ is the opening angle of Qx wings with respect to the QxCav main axis. This assumption may appear too rough, but in first approximation it is reasonable to assume that the QxCav molecules of the Langmuir monolayer, intrinsically well ordered and fully-packed, maintain their average orientation even after the transfer on the substrate preferring, thus, an orientation with the cavity facing upwards. A more realistic model for the QxCav will be discussed in the chapter 3. However, even with this simplified model it is possible to derive significant information about the average orientation of Qxcav molecules.

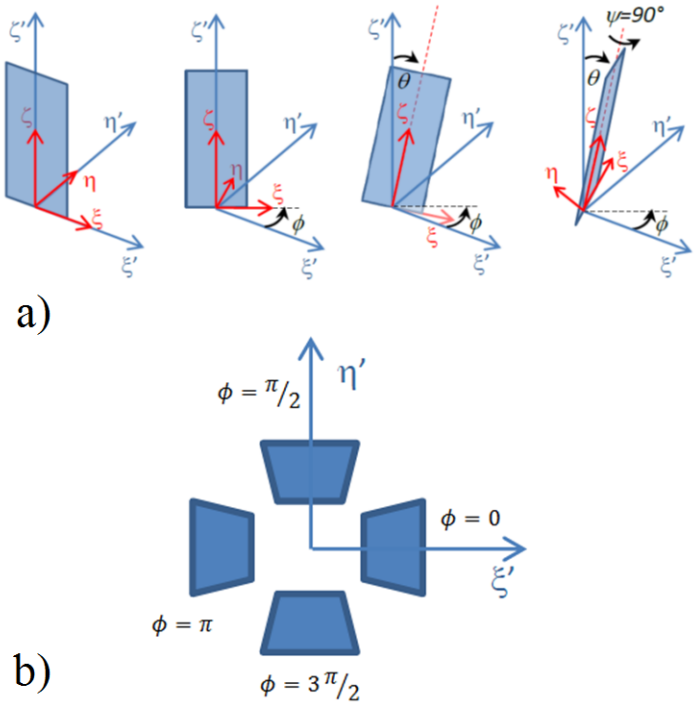

Figure 2.13: a) Z-Y-Z convention for Euler angles and b) top view of a QxCav molecule with the typical C_{4V} symmetry of its quinoxaline wings.

The expressions in eq. 2.4 were compared with the experimental amplitudes of the ν_2 mode

reported in tab. 2.3, passing through relations 1.13. From the analysis of the total symmetric stretch of the quinoxaline moiety, the polar angular ranges obtained for both OTS-QxCav and DMOAP-QxCav bilayer are $0° \leq \theta_{Qx(OTS)} \leq 34°$ and $0° \leq \theta_{Qx(DMOAP)} \leq 33°$, respectively. These results are in agreement with those of the ref. [38], in which a Langmuir film of QxCav on water is investigated. This accordance highlights that the QxCav molecules are in a vase configuration with their main axis parallel to the surface normal and pointing towards the gas phase for both the templates. Also in this case, the relative surface density of the QxCav layer on both the OTS and DMOAP SAMs, estimated from the ratio between the amplitudes $A_{\nu_2,xxz}$, is $N_{Qx}^{(DMOAP)}/N_{Qx}^{(OTS)} \simeq 2.5$. This result is in agreement with the QxCav transfer ratios for OTS (10%) and DMOAP (25%) templates obtained during the LS deposition. The reason of this disparity is most probably related to the different surface density of the two SAMs, that is lower for the DMOAP template and promotes a more efficient intercalation of QxCav alkyl chains through the organosilane layer. Therefore, a better cavitand transfer is possible for the DMOAP template, demonstrating that the surface density of the underlayer can affect that of the uppermost QxCav coating. The advantage given by the lower molecular density in the DMOAP SAM could be partially compensated by its lower ordering. Indeed, the presence of trans−gauche defects and the wider average polar angle of the outer fragments of the DMOAP alkyl chains could somewhat hamper the intercalation of the cavitand molecules by steric hindrance, thus reducing the potential upload of a conceivable template with comparable molecular density but with straight alkyl chains. A mixed SAM of long and short aliphatic organosilanes, with proper molar fraction and chains lengths, could improve the LS transfer efficiency, combining the benefits of loosely packed outer alkyl chain fragments, while still being straight and aligned with the surface normal. This could favor a denser packing in the lower part of the SAM, avoiding formation of too many defects, and a lower density in the upper part, in order to have a more efficient transfer of QxCav. This strategy will be adopted in chapter 3 for the realization of SS-HB, with an higher coverage of cavitands, for molecular recognition of aromatic hydrocarbons.

Chapter 3

Molecular recognition at solid/gas interface

Despite the large variety of synthetic receptors, their application in the real world presents common practical issues. The technology of chemical sensors is based, indeed, on the coupling of a receptor-decorated surface with a transduction mechanism, that enables to convert the specific chemical interaction between the receptor and the analyte in a readable signal. In this regard, it is pivotal to study recognition events at the interfaces, where receptors are organized. This allows to achieve a molecular-level understanding of the complexation processes that can suggest how to optimize receptor molecular architecture to improve the sensor performance in terms of accuracy and sensitivity. Furthermore, the study of host-guest *complexes* at the interfaces, in the widest range of possible operating conditions, can help in the design of synthetic receptors aiming to improve their selectivity toward target molecules and their organization for an efficient transduction scheme.

When receptors are transferred at interfaces, preservation of their selectivity and sensitivity is not irrelevant. Although their capabilities in molecular recognition have been widely studied in solution or in solid phase, their study directly at the interfaces requires additional investigations. SFVS is an *in-situ* analytical technique that allows to study both organization of receptors and host-guest interactions in real-world gas sensor operating conditions.

In this chapter, a QxCav-decorated solid substrate is studied by SFVS to elucidate the complexation of monosubstituted benzene guest. Such physico-chemical investigation provides a microscopic picture of the host-guest interaction directly at the interface, pointing out the conformation and the orientation of the QxCav molecule and the complexation geometry of the analyte inside the receptor cavity [78].

3.1 Chemical sensing of Volatile Organic Compounds

The class of Volatile Organic Compounds (VOCs) includes a large set of molecules with various functional groups and different chemical and physical properties. These chemical compounds are characterized by a high vapor pressure at ordinary room temperature that favors their considerable evaporation or sublimation in the environment. In the class of VOCs there are common organic solvents as fuels and paint diluents. The aromatic and aliphatic hydrocarbons, oxygen- and chlorine-based compounds, aldehydes, ethers, alcohols, esters, chlorofluorocabons and hydrofluorocarbons also belong to this class. In this huge variety of chemicals, the aromatic hydrocarbons known with the acronym BTEX (Benzene, Toluene, Ethylbenzene and Xylene) have strong negative effects on the central nervous system. Their presence in common substances, such as gasoline, favors the accidental exposure to these hazardous chemicals increasing the risks of correlated pathologies. Moreover, the BTEX compounds are known because of the contamination of soil, air and water sources they produce, especially in the vicinity of oil refineries and storage tanks.

Benzene and other aromatic compounds have a high toxicity and genotoxicity and are the causes of many diseases and pathologies that affect human and animal health. Because of the unavoidable exposition, due to the increasing amount of these aromatic pollutants in the environment, a continuous monitoring of BTEX concentrations is strongly required. Institutions for global health and security, in many parts of the world, have adopted different strategies and formulated many regulations for reducing the contamination of the atmosphere and water resources by these compounds. Benzene is widely used in the chemical industry as antiknock component in gasoline, but it is also naturally present in crude oil and in some petroleum derivatives. The effect due to its excessive contamination threatens global security especially for the high genotoxicity of its metabolites. Previous works, about the effects generated by the exposition to benzene, point out its behavior as myelotoxic and leukemogenic substance that decreases the production of leukocytes with a consequent weakening of the immune system, due to its accumulation in the bone marrow [79, 80]. Its various phenolic metabolites leads to the production of active oxygen that can produce carcinogenic and mutagenic effects on human DNA [81] inducing hereditary mutations and promoting pathologies as benzolism [82].

The employment of cavitands to work out new chemical sensors, due to their high selectivity and sensitivity, could play an important role in the environmental monitoring of these harmful compounds. For this reason, in order to safeguard global health, it is necessary to have precise and reliable methods for the monitoring of these substances into the environment. In this regard, quinoxaline cavitands have been proposed as viable synthetic receptors for BTEX [2, 83, 84] thanks to their selective detection of aromatic compound even in presence of inter-

ferents [40]. Their sensitivity and selectivity toward aromatic cyclic compounds make them ideal candidates for chemical sensing applications.

3.2 SS-HB characterization

The QxCav SS-HB, introduced in sec. 2.3, has been widely characterized in the second chapter and its molecular architecture has been deduced comparing two different organosilane templates. Starting from the results of that analysis, in order to achieve a higher QxCav transfer without increase in the disorder of the alkyl chains, the advantages offered by a mixed organosilane template have been exploited. Using a mixed SAM of two alkylsiloxanes with different chain length, a 30% cavitand transfer ratio (higher than that obtained for the DMOAP template) was achieved on the fused silica substrate without further increase of disorder. As shown in fig. 3.1, the high chain density at the lower rim avoids the formation of *gauche* defects, while the lower packing at the upper rim favors a better QxCav transfer. The mixed SAM combines, indeed, the advantages of a fully-packed SAM (as for the sole OTS SAM) with those of a less dense monolayer (as for the DMOAP case). To this purpose, both octadecyltrichlorosilane (OTS, $CH_3(CH_2)_{17}SiCl_3$) and octyltrichlorosilane ($CH_3(CH_2)_7SiCl_3$) (1:1) were used to prepare the hydrophobic template following the protocol used in sec. 2.3 for the sole OTS SAM. The SF measurements reported in this chapter have been carried out with the NB-SFG setup, described in sec. 1.5.2.

3.2.1 Mixed alkylsiloxane template

In fig. 3.2 the SF spectra from the mixed SAM (whose schematic picture is shown in fig. 3.1) are reported for SSP, SPS and PPP polarization configurations in the aliphatic *CH* stretching region $2800-3000\,cm^{-1}$. All the methyl and methylene modes, previously discussed in the sec. 2.4.1 for the OTS and DMOAP templates (fig. 2.9), are present [47, 75].

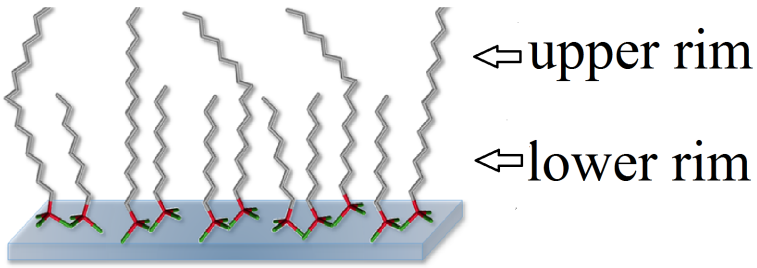

Figure 3.1: Schematic view of the mixed SAM

Comparing the SSP spectrum of the mixed SAM with those of OTS and DMOAP templates (inset of fig. 3.2), it appears more similar to the DMOAP SAM (red squares). The presence of a prominent d^+peak suggests, indeed, the formation of *gauche* defects, probably due to the lower density of the mixed SAM in the upper rim (see fig. 3.1). As mentioned in chapter 2, the theoretical surface density for a compact OTS monolayer is $3.5\,chains/nm^2$. This means that for the mixed SAM a density of about $1.8\,chains/nm^2$ is expected at the upper rim. Despite this chain density is also less than that of DMOAP (about $2.5\,chains/nm^2$), the mixed SAM does not show a more disordered conformation thanks to the higher packing at the lower part. This discussion is supported below by quantitative analysis on the r^+ mode, that allows to deduce the average polar orientation of the methyl group.

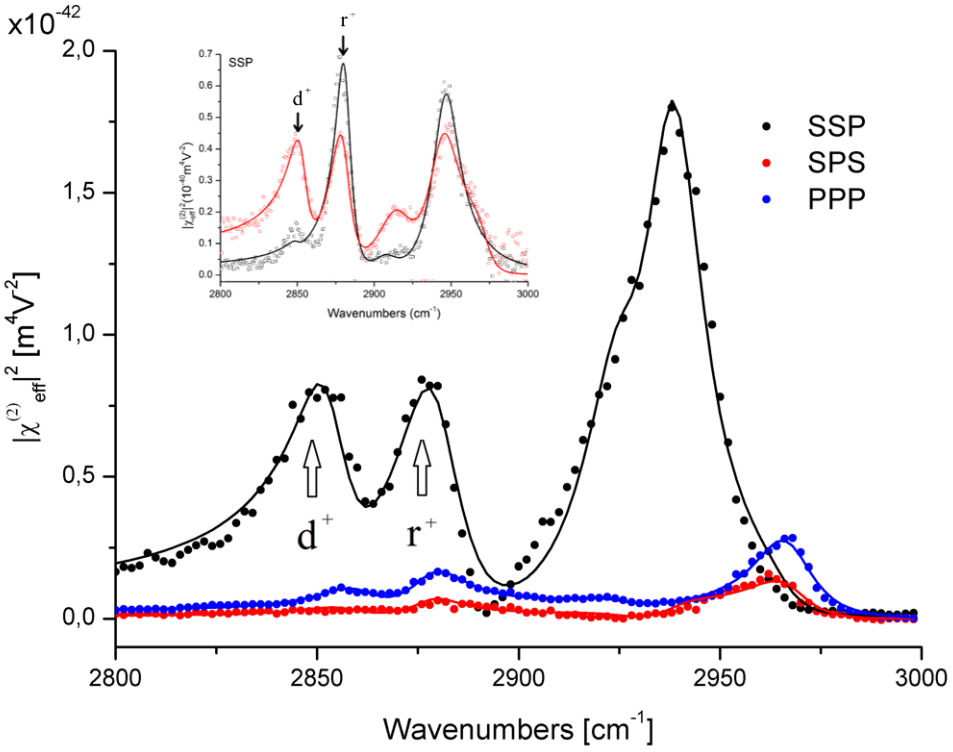

Figure 3.2: SF spectra from mixed $CH_3(CH_2)_{17}-$ and $CH_3(CH_2)_7-$silane (1:1) SAM (in the inset of the graph) in SSP, SPS and PPP polarization configurations. Solid lines are the corresponding best curve fits. In inset the SSP spectra of OTS (black squares) and DMOAP (red squares) templates.

The fit parameters of the mixed OTS SAM (solid lines in fig. 3.2) are reported in table 3.1. From the resonant amplitudes of the methyl mode r^+ an the average orientation of the methyl group has been evaluated $\langle\theta_{CH_3,OTS}\rangle \simeq 61° \pm 4°$ (see fig. 2.10), assuming an ODF $f(\Omega) = \delta(\theta - \theta_{CH_3}) / (4\pi^2 \sin\theta_{CH_3})$. The polar angle of the CH_3 group is close to that obtained for

mixed OTS	$\omega\,[cm^{-1}]$	$\Gamma\,[cm^{-1}]$	A_{SSP}	A_{SPS}	A_{PPP}
d^+	2854	8	0.4	0.2	-0.4
r^+	2880	10	0.7	-0.2	0.4
d^-	2925	9	0.5	0.0	0.6
r^+_{FR}	2938	9	1.0	-0.1	-0.4
r^-	2967	9	-0.2	0.3	5.7

Table 3.1: Fit parameters for mixed OTS SAM

the DMOAP SAM, supporting what discussed above. The mixed SAM offers, indeed, a lower chain density at the upper rim with respect to the DMOAP template without affecting more the alkyl chain conformation.

3.2.2 Orientational analysis of receptors

After the quantitative analysis on the mixed SAM, a QxCav-alkylsiloxane bilayer 3.3 was realized with the LS procedure described in sec. 2.3. The mixed SAM of $CH_3(CH_2)_{17}-$ and $CH_3(CH_2)_7-$OTS (1:1), preferred in order to increase the QxCav coverage without increasing the disorder of the alkyl chains, promotes a QxCav transfer ratio of about 30% as estimated during the LS deposition, performed in the liquid-condensed phase at about 20 mN/m. This results confirms that the choice of a mixed SAM favors a enhanced QxCav transfer with respect to both the pure OTS (10%) and DMOAP (25%). Further investigations have been planned in order to optimize the ordering of the SAM and promote even higher transfer, by varying both aliphatic chain lenght and molar ratio in the alkylsilane solution.

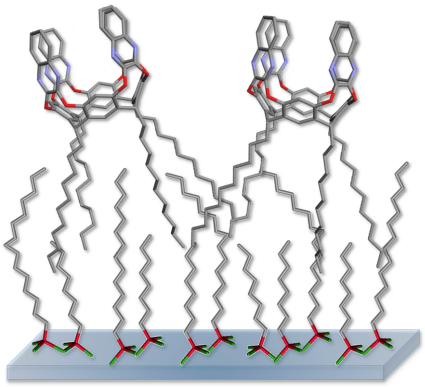

Figure 3.3: SS-HB of QxCav deposited on a mixed alkylsiloxane SAM of $CH_3(CH_2)_{17}-$ and $CH_3(CH_2)_7-$silane (1:1) (1:1)

The SF spectra of the QxCav-alkylsiloxane sample are reported in fig. 3.4 for SSP, SPS and

PPP polarization configurations in the $2800-3100\,cm^{-1}$ range, in which both aliphatic and aromatic *CH* stretch modes are expected. The resonant modes in the aliphatic range are due to the alkyl chains of both SAM and QxCav molecules and are assigned to symmetric stretching, asymmetric stretching and Fermi resonance of methylene and methyl groups. Three aromatic resonances can be distinguished in the range $3000-3100\,cm^{-1}$ and attributed to the asymmetric stretch ν_7 ($3038\,cm^{-1}$) and the symmetric stretches ν_2 and ν_{20} (3066 and $3080\,cm^{-1}$) of the quinoxaline wings [75, 77]. In the inset of fig. 3.4, an enlargement of the spectra in the aromatic *CH* stretching region is reported with the vector diagrams of symmetric ν_2 and ν_{20} modes. From the curve fits on these experimental data (solid lines in inset of fig. 3.4), it is possible to deduce the resonant amplitudes for the total-symmetric stretch ν_2 needed to deduce the average orientation of the the QxCav molecules [38, 75, 85]. We have carried

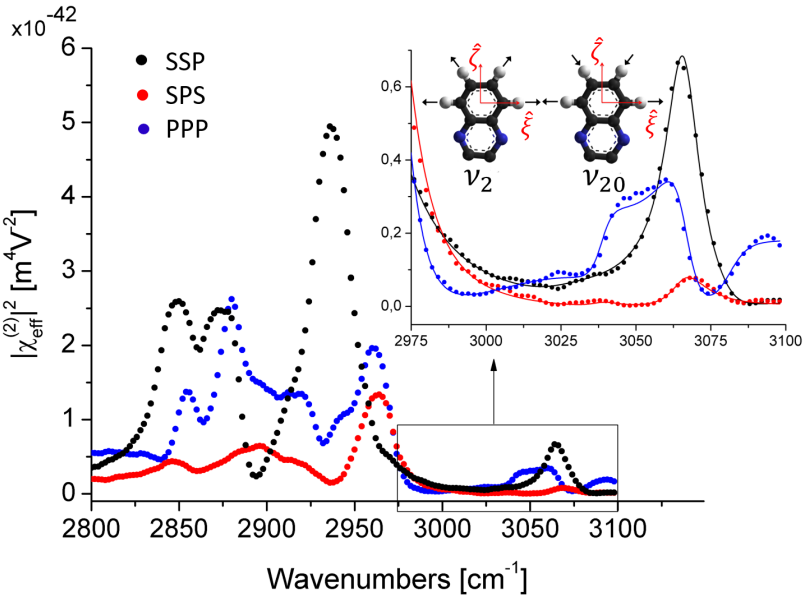

Figure 3.4: SF spectra of QxCav-organosilane bilayers for SSP, SPS and PPP polarization configurations. The inset shows an enlargement of the spectra in the aromatic *CH* stretching region and their best curve fits. The vector diagrams for ν_2 and ν_{20} modes are also reported.

out spectral analysis for the aromatic *CH* stretch mode ν_2 of the quinoxaline (Qx) group to deduce information about the aperture angle θ_m of the Qx wings and the average polar orientation θ_p of the QxCav (fig. 3.5). In order to write the three independent non-vanishing resonant amplitudes $A_{\nu_2,ijk}$ in term of the two non-vanishing hyperpolarizability amplitudes $a_{\nu_2,\xi\xi\xi}$ and $a_{\nu_2,\zeta\zeta\zeta} = r_{\nu_2} a_{\nu_2,\xi\xi\xi}$ of the Qx group ($r_{\nu_2} \simeq 2.4$), we should consider that each QxCav molecule comprises four Qx wings (C_{4v} symmetry in the closed vase conformation) which contribute to the hyperolarizability of the whole molecule. The effective hyperpolariz-

ability amplitudes $a_{\nu_2,l'm'n'}$ for the QxCav in its molecular frame (ξ',η',ζ') can be calculated considering the Euler angles of each quinoxaline moiety and their hyperpolarizability elements $a_{\nu_2,lmn}$ expressed in its group frame (ξ,η,ζ). In fig. 2.13 a schematic representation of the Euler angles for the Qx moiety is shown. The hyperpolarizability terms of the QxCav in its frame (ξ',η',ζ') can be calculated taking into account the four quinoxaline contributions using the bond additivity model (explained in sec. 1.4) as reported in eq. 3.1.

$$\begin{aligned}
&a_{\nu_2,\xi'\xi'\zeta'} = a_{\nu_2,\eta'\eta'\zeta'} = 2a_{\nu_2,\xi\xi\zeta}\cos\theta_m\left(1+r_{\nu_2}\sin^2\theta_m\right)\\
&a_{\nu_2,\xi'\zeta'\xi'} = a_{\nu_2,\zeta'\xi'\xi'} = a_{\nu_2,\eta'\zeta'\eta'} = a_{\nu_2,\zeta'\eta'\eta'} = 2r_{\nu_2}a_{\nu_2,\xi\xi\zeta}\sin^2\theta_m\cos\theta_m\\
&a_{\nu_2,\zeta'\zeta'\zeta'} = 4r_{\nu_2}a_{\nu_2,\xi\xi\zeta}\cos^3\theta_m
\end{aligned} \tag{3.1}$$

In the expressions above, θ_m is the aperture angle of the Qx wings with respect to the QxCav main axis ζ'. Now the macroscopic resonant amplitudes $A_{\nu_2,ijk}$ can be written in the sample frame (X,Y, Z) as follows:

$$\begin{aligned}
A_{\nu_2,xxz} &= 2N_{QxCav}a_{\nu_2,\xi\xi\zeta}\left\langle\cos\theta\cos\theta_m\left[1+r_{\nu_2}\sin^2\theta_m-\sin^2\theta\sin^2\phi\left(1-2r_{\nu_2}+5r_{\nu_2}\sin^2\theta_m\right)\right]\right\rangle\\
A_{\nu_2,xzx} &= 2N_{QxCav}a_{\nu_2,\xi\xi\zeta}\left\langle\cos\theta\cos\theta_m\left[r_{\nu_2}\sin^2\theta_m-\sin^2\theta\sin^2\phi\left(1-2r_{\nu_2}+5r_{\nu_2}\sin^2\theta_m\right)\right]\right\rangle\\
A_{\nu_2,zzz} &= 2N_{QxCav}a_{\nu_2,\xi\xi\zeta}\left\langle\cos\theta\cos\theta_m\left[\sin^2\theta\left(1+3r_{\nu_2}\right)+r_{\nu_2}\cos^2\theta_m\left(5\cos^2\theta-3\right)\right]\right\rangle
\end{aligned} \tag{3.2}$$

where N_{QxCav} is the surface density of QxCav molecules and θ is the polar angle the QxCav main axis ζ' forms with the Z axis, as shown in fig. 3.5, and the angular brackets denote the average over the ODF of the QxCav molecules. Because of the symmetry of the system, isotropic orientational distribution is assumed with respect to the azimuth ϕ and torsion ψ Euler angles and the normalized ODF can be written as:

$$f(\Omega) = \frac{\delta(\theta-\theta_p)}{4\pi^2\sin\theta_p} \tag{3.3}$$

NB-scheme	$\lambda\,(nm)$	$\beta\,(deg)$	n	L_{xx}	L_{yy}	L_{zz}
ω_{SF}	460	59	1.459	1.04	0.61	0.66
ω_1	532	60	1.458	1.05	0.60	0.65
ω_2	3400	55	1.409	1.00	0.67	0.69

Table 3.2: Fresnel factors calculated for the SS-HB in the CH stretching region, for NB-SFS setup

The evaluation of the terms in angular brackets of eqs. 3.2 allows to write the macroscopic resonant amplitudes $A_{\nu_2,ijk}$ as:

$$A_{\nu_2,xxz} = \frac{1}{4}N_{QxCav}a_{\nu_2,\xi\xi\zeta}\cos\theta_p\cos\theta_m\left[\left(2+r_{\nu_2}\right)\left(3+\cos 2\theta_p\right)+r_{\nu_2}\left(1-5\cos 2\theta_p\right)\cos 2\theta_m\right]$$

$$A_{\nu_2,xzx} = \frac{1}{4}N_{QxCav}a_{\nu_2,\xi\xi\zeta}\cos\theta_p\cos\theta_m\left[r_{\nu_2}\cos 2\theta_m-2+3r_{\nu_2}+\cos 2\theta_p\left(2+r_{\nu_2}-5r_{\nu_2}\cos 2\theta_m\right)\right] \tag{3.4}$$

$$A_{\nu_2,zzz} = \frac{1}{2}N_{QxCav}a_{\nu_2,\xi\xi\zeta}\cos\theta_p\cos\theta_m\left[-\left(2+r_{\nu_2}\right)\cos 2\theta_p+5r_{\nu_2}+2+r_{\nu_2}\left(-1+5\cos 2\theta_p\right)\cos 2\theta_m\right]$$

The eqs 3.4 enable to carry out a quantitative analysis on the ν_2 to deduce both orientation and conformation of the QxCav molecules.

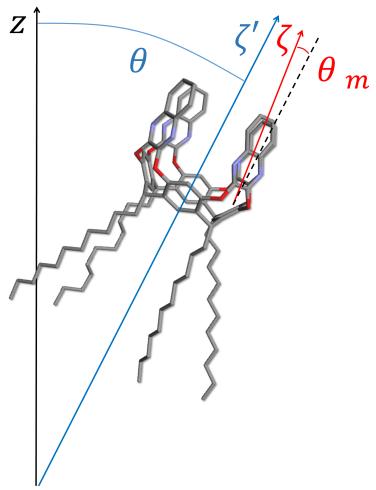

Figure 3.5: Representation of QxCav in sample frame, where θ_m is the aperture angle of the quinoxaline moiety with respect to the cavitand main axis ζ', while θ indicates the polar angle that the whole QxCav molecule forms with the Z axis.

Through eqs. 3.4, in relation to the Fresnel factors reported in tab. 3.2 and to the angles of

input and output beams, it is possible to compare theoretical values of the resonant amplitudes $A_{\nu_2,ijk}$ with their experimental values, obtained from the fits of the SF data reported in tab. 3.3.

SS-HB	$\omega\,[cm^{-1}]$	$\Gamma\,[cm^{-1}]$	A_{SSP}	A_{SPS}	A_{PPP}
ν_7	3038	4.3	0.1	0.2	-0.7
ν_2	3066	7.2	6.3	1.7	2.9
ν_{20}	3080	7.5	-2.0	0.3	-0.7

Table 3.3: Fit parameters for the SF spectra of SS-HB in the aromatic *CH* stretching region.

In fig. 3.6 the ratios between the amplitudes $A_{\nu_2,SPS}/A_{\nu_2,SSP}$ and $A_{\nu_2,PPP}/A_{\nu_2,SSP}$, calculated through eq. 1.13, are reported as a function of the angles θ_m and θ_p. From the quantitative

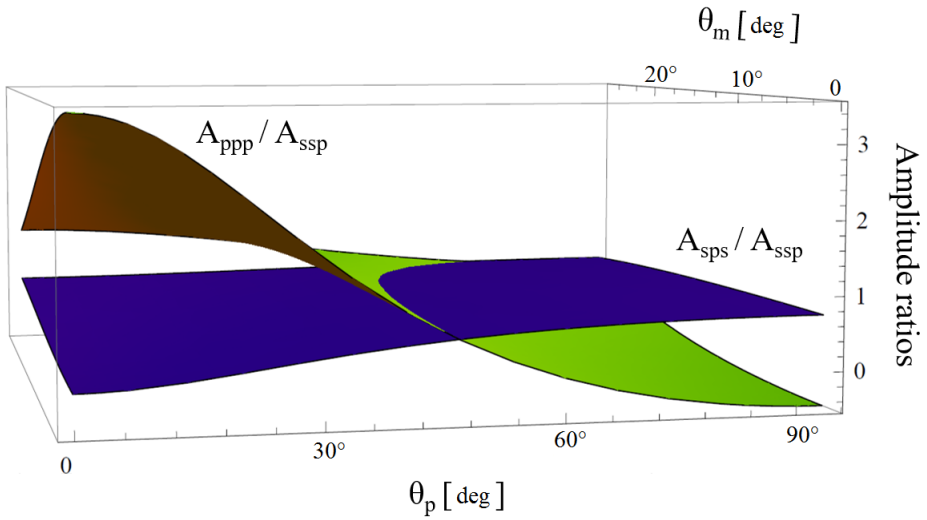

Figure 3.6: Amplitude ratios $A_{\nu_2,SPS}/A_{\nu_2,SSP}$ and $A_{\nu_2,PPP}/A_{\nu_2,SSP}$ as a function of the aperture θ_m and polar θ_p angles.

analysis the polar angle $\theta_p = (48° \pm 11°)$ and the aperture angle $\theta_m = (13° \pm 2°)$ are deduced, confirming that the QxCav molecules keep the *vase* configuration, the most favourite one for guest complexation. [38]. The polar angle $\theta_p \simeq 48°$ suggests that the QxCav molecules point towards the gas phase, but with their main axis exhibiting a significant deviation from the surface normal.

3.3 Sensing at air/solid interface

To have evidence of analyte complexation at the gas/solid interface, the SS-HB was exposed to vapors of an aromatic compound. In particular, benzonitrile (C_6H_5CN) was chosen as the

target molecule because of the strong chemical affinity of its aromatic part with the QxCav. Furthermore, the *CN* group is a strong vibrational marker whose resonant frequency does not overlap with those of the aliphatic and aromatic *CH* stretching modes. Taking into account the *CN* stretching mode, the average orientation of the analyte can be deduced and the geometry of complexation can be reconstructed. To this purpose, the QxCav-alkylsiloxane SSHB is placed in a gastight chamber (triangle) and exposed to saturated C_6H_5CN vapor in air (see fig. 3.7) at normal temperature and pressure. The chamber is equipped with two barium fluoride windows (in yellow), transparent in the spectral range of the input and output beams. SSP (S-polarized SF output, S-polarized visible, and P-polarized IR inputs) polarization combination is shown. The beams angles θ_i are reported versus the surface normal.

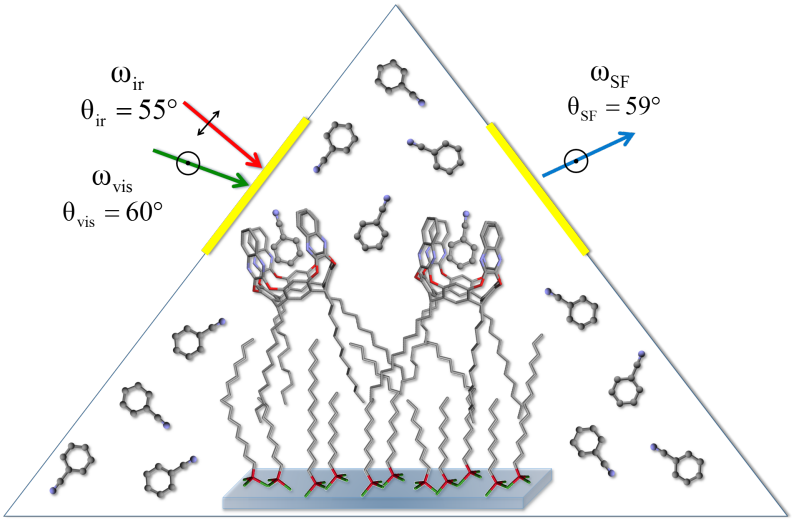

Figure 3.7: Schematic view of the gastight chamber (triangle) used for the SF measurements performed in benzonitrile vapor. The two windows (in yellow) are transparent in the spectral range of the input and output beams. The SSP polarization configuration is shown.

In fig. 3.8 the SF spectra of both the SS-HB and bare SAM exposed to vapor of benzonitrile are reported in the *CN* stretching range $2200-2300\,cm^{-1}$ [86, 87] for SSP, SPS and PPP polarization configurations. A prominent peak at $\sim 2240\,cm^{-1}$ in the SSP spectrum of SS-HB (black circles), relative to the stretching mode of the *CN* group, attests the occurred complexation of the analyte, while it appears less intense in SPS and PPP spectra. This difference between SSP, SPS and PPP spectra suggests that the "$\widehat{\zeta}$" axis of the analyte (see inset of fig. 3.8-a) has a significant projection along the surface normal. In the case of the bare SAM exposed to benzonitrile vapor, the *CN* peak in the spectra (red circles) is virtually absent. This experimental evidence indicates that the SS-HB promotes a net polar orientation of the complexed benzonitrile molecules at the solid-vapor interface, while for the bare template the much lower *CN* peaks can be attributed to non-specific interactions between the alkyl

chains and the analyte. Thus, the QxCav layer increases the sensitivity of the sample due to the specific host-guest interactions with the benzonitrile molecules.

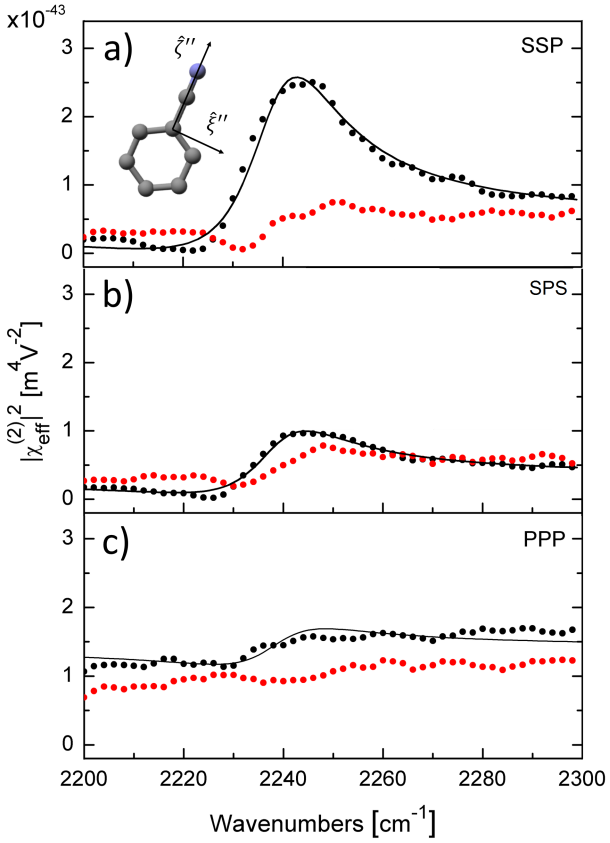

Figure 3.8: SF spectra in the *CN* stretching range of QxCav SS-HB (black circles) and alkylsiloxane template (red circles) exposed to saturated vapor of benzonitrile in air. The black lines are the best curve fits on the QxCav SS-HB spectra. The insets shows the benzonitrile molecule in the molecular frame (ξ'', η'', ζ''), where the ζ'' axis is along the *CN* bond and the phenyl ring in the $\xi'' - \zeta''$ plane.

This qualitative analysis is supported by spectral fitting of the SS-HB exposed to benzonitrile vapors, whose best curves and fit parameters are reported in fig. 3.8 and tab. 3.4, respectively.

The orientation of the analyte chemisorbed at the SS-HB surface has been evaluated from the amplitudes of the *CN* stretching mode (reported in tab. 3.4) and the corresponding three

SS-HB	$\omega\,[cm^{-1}]$	$\Gamma\,[cm^{-1}]$	A_{SSP}	A_{SPS}	A_{PPP}
CN	2238	11	4.6	2.4	-0.75

Table 3.4: Fit parameters for the SF spectra of SS-HB exposed to benzonitrile vapors in the *CN* stretching range.

NB-scheme	$\lambda\,(nm)$	$\beta\,(deg)$	n	L_{xx}	L_{yy}	L_{zz}
ω_{SF}	470	59	1.459	1.03	0.62	0.66
ω_1	532	60	1.458	1.05	0.60	0.65
ω_2	4400	55	1.409	1.00	0.67	0.68

Table 3.5: Fresnel factors for SS-HB in the CN stretching region

nonvanishing amplitudes of the resonant contribution to the nonlinear susceptibility.

$$\begin{aligned} A_{CN,xxz} &= \frac{1}{2} N_{CN} a_{CN,\zeta''\zeta''\zeta''} \left[(1+r_{CN}) \langle cos\theta \rangle - (1-r_{CN}) \langle cos^3\theta \rangle \right] \\ A_{CN,xzx} &= \frac{1}{2} N_{CN} a_{CN,\zeta''\zeta''\zeta''} (1-r_{CN}) \left[\langle cos\theta \rangle - \langle cos^3\theta \rangle \right] \\ A_{CN,zzz} &= N_{CN} a_{CN,\zeta''\zeta''\zeta''} \left[r_{CN} \langle cos\theta \rangle + (1-r_{CN}) \langle cos^3\theta \rangle \right] \end{aligned} \tag{3.5}$$

where N_{CN} is the surface density of *CN* groups, and thus of benzonitrile molecules, $r_{CN} = a_{CN,\xi''\xi''\zeta''}/a_{CN,\zeta''\zeta''\zeta''} = 0.26$ is the depolarization ratio [47, 86, 87], θ is the polar angle between ζ'' axis of the analyte (see inset of fig. 3.8) and the surface normal and the angular brackets denote an average over the assumed ODF $f(\Omega) = \delta(\theta - \theta_{CN})/4\pi^2 \sin\theta_{CN}$. In fig. 3.9 the theoretical ratios between the resonance amplitudes of the *CN* stretching mode are reported as a function of the polar angle according to Fresnel factors in tab. 3.5 and eqs. 3.5 and 1.13 . Comparing the theoretical amplitudes with the fitted parameters of tab. 3.4, a value for the polar angle of $\theta_{CN} = (43° \pm 15°)$ is deduced.

The perfect overlap between the average polar angle of the analyte (θ_{CN}) and the cavitand (θ_p) suggests a *on-axis* complexation of the analyte within the QxCav cavity, which therefore engulfs the benzonitrile molecule with its major axis along ζ'. However, this analysis does not allow to distinguish between the two possible orientations of the *CN* group, which can point towards the cavity of the receptor $\hat{\zeta}'' \cong -\hat{\zeta}'$ or toward the gas phase $\hat{\zeta}'' \cong \hat{\zeta}'$ (as shown in fig. 3.10). To establish the absolute orientation of the complexed molecules, an analysis of the aromatic *CH* modes of the sample exposed to air and to benzonitrile vapors is required.

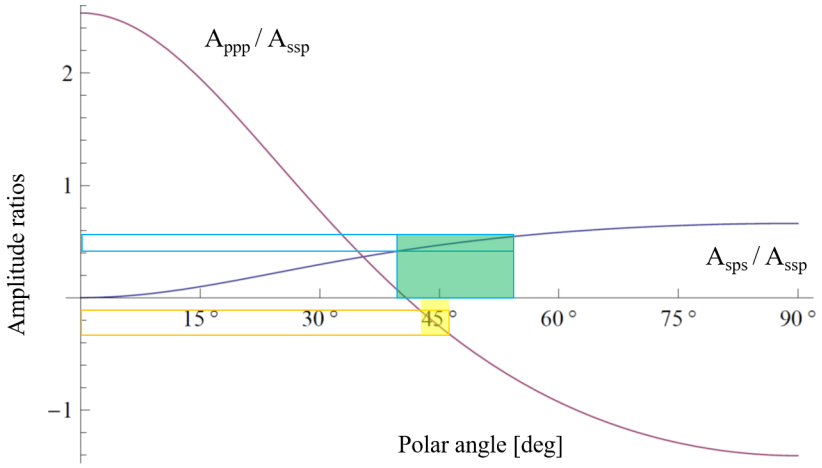

Figure 3.9: Amplitude ratios $A_{CN,SPS}/A_{CN,SSP}$ (blue line) and $A_{CN,PPP}/A_{CN,SSP}$ (purple line) as a function of polar angle θ. Green and yellow area represent the experimental ranges for CN stretch amplitude ratios.

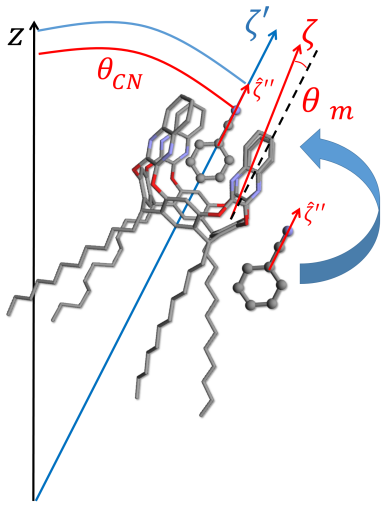

Figure 3.10: Representation of the complexation of benzonitrile molecule inside the receptor cavity. θ_{CN} is the polar angle between the main axis of the analyte ζ" and the Z axis.

To clarify what is the absolute orientation of the analyte, the SF spectra of the SS-HB exposed to air (solid circles) and to benzonitrile vapors (open circles) with their relative curve fit (black lines) are shown 3.11 in the range $3000 - 3100\,cm^{-1}$. The single contributions of the symmetric stretching modes ν_{20} (blue line) and ν_2 (red line), with their relative sign, to the SSP spectrum are reported in fig. 3.11-a for the sample exposed to air (solid lines) and to benzonitrile vapors (dashed lines).

The amplitude of the ν_2 mode for the SS-HB exposed to air (red solid line) goes to zero

after the exposure to benzonitrile vapors (red dashed line).

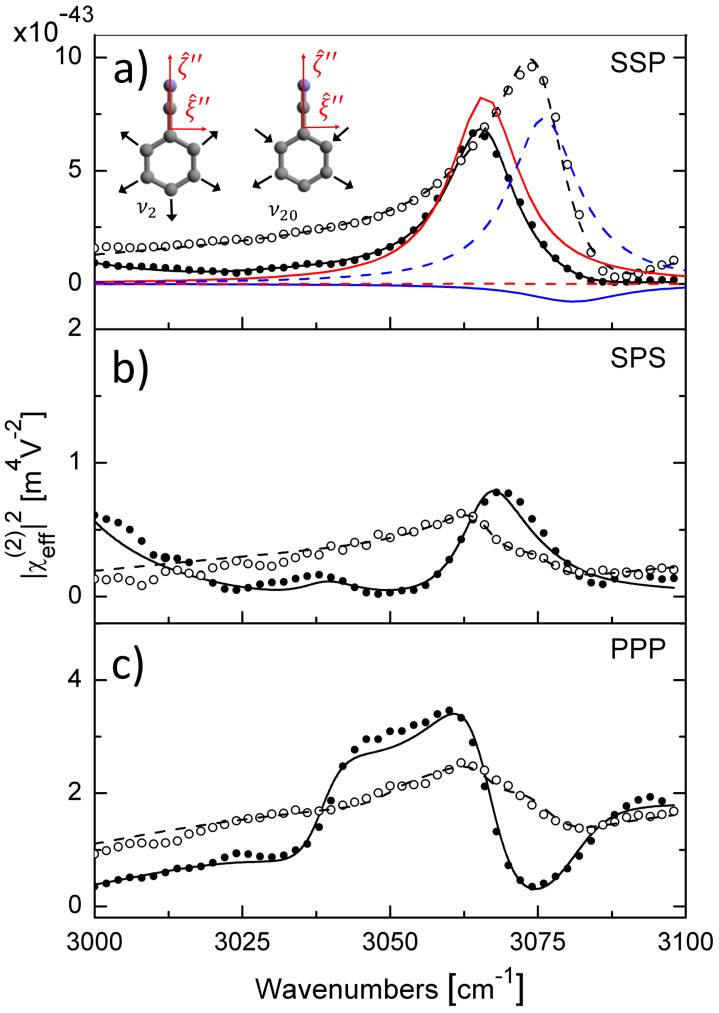

Figure 3.11: SF spectra of QxCav SS-HB exposed to air (solid circles) and to saturated vapor of benzonitrile in air (open circles) with their best curve fits (solid and dashed lines, respectively) in the aromatic CH stretching range. The red and blue lines reported in a) are the ν_2 and ν_{20} vibrational modes, respectively, that contribute to the spectra of bilayer exposed to air (solid lines) and to saturated vapor of benzonitrile in air (dashed lines).

This is the result of the destructive interference between the quinoxaline wings and the aromatic moieties of the benzonitrile molecules, whose resonance frequencies are overlapped to the quinoxaline ones. Also the amplitude of the ν_{20} mode (blue solid line) decreases and changes sign after the exposition to the analyte (blue dashed line) due to the destructive interference between the host and the guest. The suppression of both the ν_2 and ν_{20} amplitudes is a confirmation that the analyte prefers to be complexed with the aromatic part inside the cavity

of the QxCav and with the *CN* group that points toward the gas phase. This is not surprising because the specific host-guest interactions are due to the strong chemical affinity of QxCav with aromatic compounds, as confirmed by studies about the complexation of monosubstituted benzene guests [60] in solid state and solution.

The analysis performed on the *CN* stretching mode allowed to deduce the average orientation of the complexed benzonitrile molecules, while the analysis carried out on the aromatic stretching modes permitted to distinguish between the two possible configurations: *up* ($\hat{\zeta}'' \cong \hat{\zeta}'$) or *down* ($\hat{\zeta}'' \cong -\hat{\zeta}'$). The obtained results provided a complete physical picture of the complexation mechanism highlighting the geometry of host-guest interaction.

3.3.1 Testing selectivity of QxCav

In order to test the selectivity of the QxCav SS-HB in the chemical recognition of aromatic compounds, the sample was exposed to acetonitrile (CH_3CN) vapors. The presence of the same *CN* group allows to compare the SF spectra of the sample exposed to benzonitrile and acetonitrile in the *CN* stretching region, as reported in fig. 3.12.

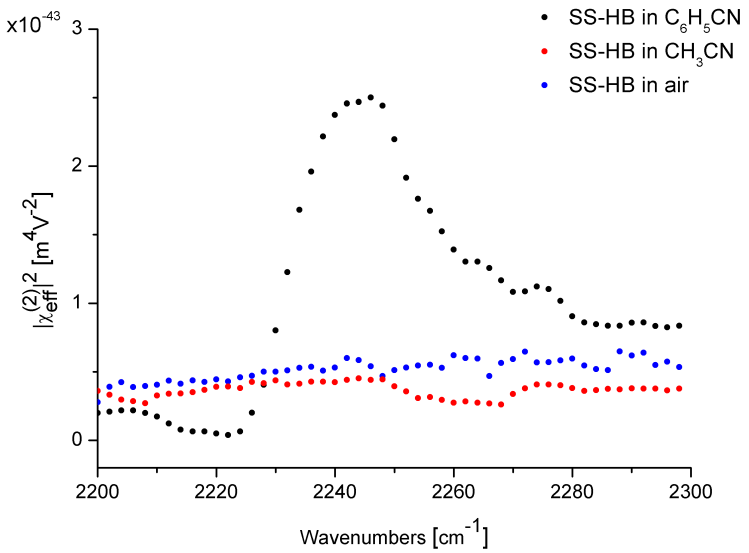

Figure 3.12: SF spectra of QxCav SS-HB, in SSP polarization configuration, exposed to air (blue circles) and to saturated vapor of benzonitrile (black circles) and acetonitrile (red circles) in the CN stretching region.

The SSP spectrum of the SS-HB exposed to benzonitrile vapors (black circles) exhibits a prominent peak relative to the *CN* stretching mode, while the same resonance is virtually

absent for the sample exposed to acetonitrile vapors (red circles). Such evidence signifies that CH_3CN molecules do not show any preferential ordering imposed by the uppermost QxCav layer. They are either not adsorbed or simply physisorbed without ordering at the interface, as expected because of the their low chemical affinity with QxCav. This experimental evidence proves that the selectivity of QxCav towards aromatic compounds is maintained at the solid/gas interface.

3.4 High non-resonant susceptibility substrates

The analysis presented in this chapter has put in evidence the difficulty in deducing *absolute* orientation of molecules at interface. For the benzonitrile case, for example, a supplementary analysis on the ν_2 mode has been necessary to distinguish between the *up* or *down* orientation of the nitrile group. The reason is that each resonant mode has a proper phase, being the resonant part of the $\overleftrightarrow{\chi}^{(2)}$ tensor a complex quantity, but SFG intensity is proportional to the square modulus of the effective nonlinear susceptibility (eq 1.3). Therefore, phase information is often not easily accessible. This problem can be overcome with different approaches [88, 89]. A substrate with a high nonlinear optical response, that contributes significantly the total second-order non-linear susceptibility $\overleftrightarrow{\chi}^{(2)}$, can offers advantages in deducing absolute phases, and thus orientation, of molecules. The overall susceptibility depends, indeed, on both resonant and non-resonant contribution as:

$$\chi^{(2)}_{ijk} = \left|\chi^{(2)}_{NR,ijk}\right| e^{i\varphi_{NR}} + \left|\chi^{(2)}_{R,ijk}\right| e^{i\varphi_R} \tag{3.6}$$

where the terms $\left|\chi^{(2)}_{NR,ijk}\right|$ and $\left|\chi^{(2)}_{R,ijk}\right|$ are the magnitudes of the non-resonant and resonant susceptibility, respectively, while φ_{NR} and φ_R indicate the corresponding phases. Assuming a resonant susceptibility with only one non-zero component to simplify the following calculations, the SF intensity can be written as:

$$I_{SF} \propto \left|\left|\chi^{(2)}_{NR,ijk}\right| e^{i\varphi_{NR}} + \left|\chi^{(2)}_{R,ijk}\right| e^{i\varphi_R}\right|^2 =$$

$$\left|\chi^{(2)}_{NR,ijk}\right|^2 + \left|\chi^{(2)}_{R,ijk}\right|^2 + 2\cdot\left|\chi^{(2)}_{NR,ijk}\right|\cdot\left|\chi^{(2)}_{R,ijk}\right|\cdot\cos(\varphi_{NR}-\varphi_R) \tag{3.7}$$

For many centrosymmetric dielectric substrates, for example fused silica and glass surfaces, $\left|\chi^{(2)}_{NR,ijk}\right|$ is almost zero, because both IR and visible frequencies are far from electronic, vibrational or phonon modes. On the contrary, materials like metals and crystals (i.e.

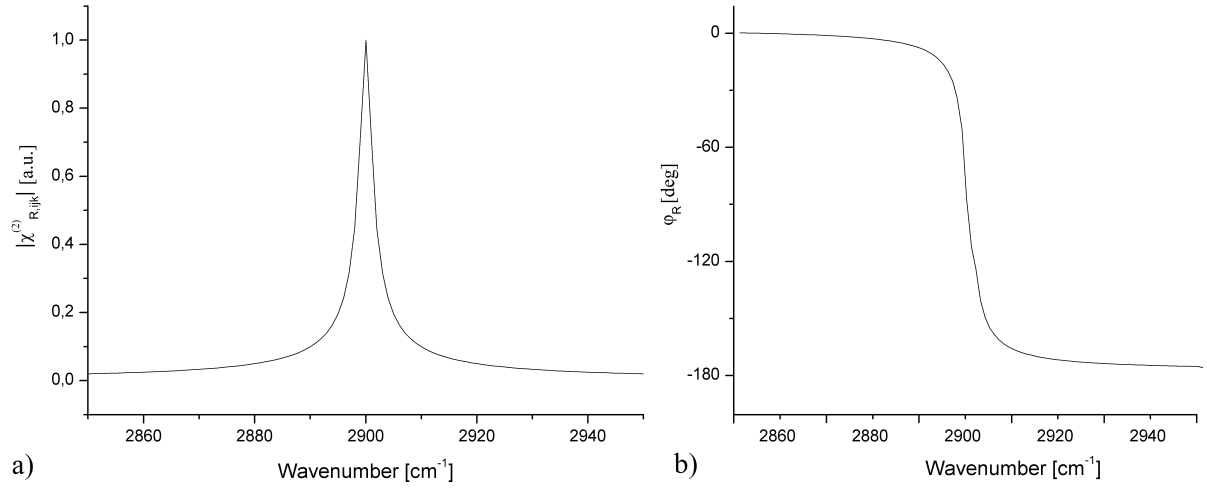

Figure 3.13: a) Magnitude and b) phase of $\chi^{(2)}_{R,ijk}$ for an arbitrary resonance centered at $\omega_q = 2900\,cm^{-1}$ with amplitude $A_q = 1$ and damping constant $\Gamma_q = 1$.

gold, silver and quartz), far from interband transition, exhibit a strong non-resonant response with a constant phase, enhancing the overall SF signal and acting as a reference. The term $\cos(\varphi_{NR} - \varphi_R)$ affects the SF intensity due to the interference between resonant and non-resonant terms. For example, when resonant and nonresonant contributions are out of phase, a reduction of the SF intensity occurs and the corresponding resonance in the spectrum appears as a deep (see fig. 3.4).

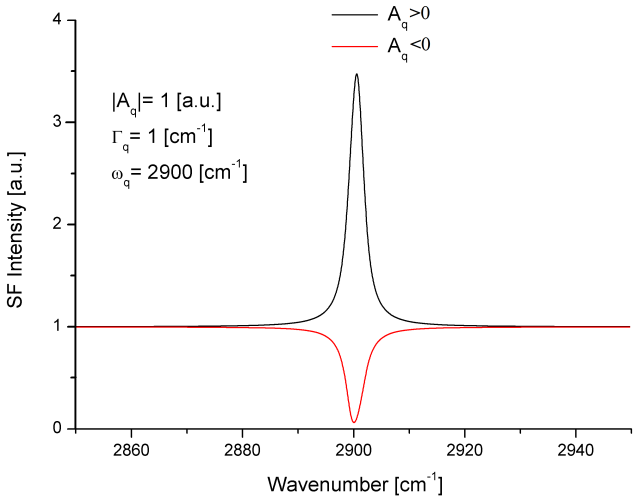

Figure 3.14: Calculated SFG spectra assuming $\left|\chi^{(2)}_{NR,ijk}\right| = 1$ and $\varphi_{NR} = -\pi/2$, and an arbitrary resonance centered at $\omega_q = 2900\,cm^{-1}$ with amplitude $|A_q| = 1$ and damping constant $\Gamma_q = 1$.

Furthermore, the possibility to anchor cavitands directly on metals or crystals can combine the advantages offered by SFVS with those related to the transduction mechanism. The chemical host-guest interaction, indeed, has to be converted into a readable optical or electrical signal. For instance, metal substrates can act as intermediate in transduction process and can be easily integrated into opto-electronic devices. Gold, for example, is widely used in Surface Plasmonic Resonance (SPR) studies for chemical sensing applications [90] and functionalized quartz crystals are already used in Quartz Crystal Microbalance (QCM) as sensors [91]. Another strategy to deduce the phases associated to the vibrational modes is offered by the Phase-Sensitive SFVS, that uses a SF generator (e.g. quartz) to obtain a reference SF signal, allowing spectral measurements of both amplitude and phase of the susceptibility tensor $\overleftrightarrow{\chi}^{(2)}$ [74].

In previous studies the advantages offered by semiconductor, metal and crystal substrates, properly coated with synthetic receptors, have been exploited [1, 72, 92–96]. With proper functionalities at the lower rim, indeed, cavitands can be covalently grafted on technologically relevant surfaces.

In this section the investigation of a SAM of alkylthiols deposited on a gold substrate is reported. This is a preliminary analyis that wants to drive to a more rational functionalization of gold substrate. The final goal, indeed, is to anchor cavitands with proper functional groups at the lower rim on gold substrates.

3.4.1 SAM on gold surface

The non-resonant contribution of a gold substrate provides an internal reference that obviates the need for an external reference, usually called local oscillator, necessary for phase-sensitive SFVS such as quartz plate. In this regard, a gold film, with a thickness of about 200 nm, was evaporated on a glass substrate on which a thinner layer of Nickel (about 8 nm) was previously deposited to increase gold adhesion. The substrate was then immersed in a 2mM solution of dodecanethiol ($CH_3(CH_2)_{11}SH$, 98% Sigma Aldrich) in ethanol for about 20 h [97]. Static contact angle measurements were performed on both bare and dodecanethiol-coated gold surfaces to verify the quality of the SAM. Contact angle of $\theta = 40°$ and $\theta = 108°$ were found for the gold substrate before and after SAM formation, respectively, as shown in fig. 3.15. The contact angle found for the dodecanethiol (DCT) SAM is in agreement with that of a compact monolayer [98].

In fig. 3.16 the SF spectra of DCT SAM on gold substrate are reported in the aliphatic CH stretching region for SSP, SPS and PPP polarization configurations together with their corresponding best curve fits. The alkyl chain of the DCT molecules exhibit the same methyl and methylene modes previously observed for OTS and DMOAP SAMs, but the non-resonant

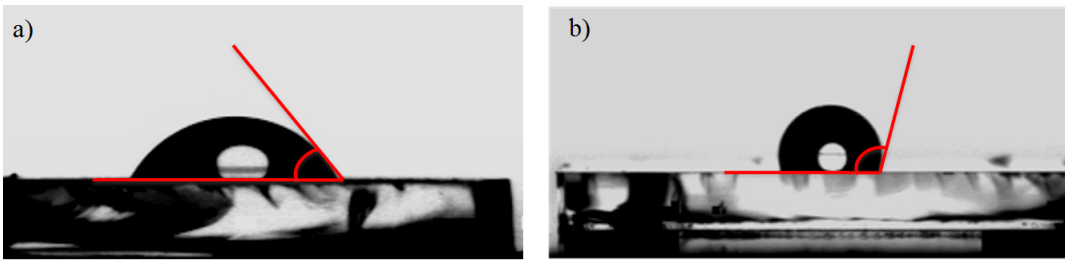

Figure 3.15: Contact angle measurements of a) bare gold and b) dodecanethiol-coated gold surface

NB-scheme	$\lambda\,(nm)$	$\beta\,(deg)$	n	L_{xx}	L_{yy}	L_{zz}
ω_{SF}	460	59	1.418	0.39	0.38	0.66
ω_1	532	60	0.467	0.17	0.11	0.29
ω_2	3400	55	2.052	0.40	0.48	0.69

Table 3.6: Fresnel factors for DCT on gold.

contribution is, in this case, much greater. This increases the square modulus of the effective susceptiptibility tensor, resulting in an global enhancement of the SF signal [99].

From the fit of the data the resonant amplitudes of the r^+ stretching mode of the methyl group can be deduced (see tab. 3.7). Assuming an ODF as $f(\Omega) = \delta(\theta - \theta_{CH_3}) / \left(4\pi^2 \sin\theta_{CH_3}\right)$, an average orientation for the methyl group of about $\theta_{CH_3} \simeq 62°$ is found. In fig. 3.17 the theoretical amplitude ratios for the methyl group are reported for the assumed ODF.

Considering that methyl group forms an angle of about 35° with the main axis of the aliphatic chain, an angle of about $\theta \simeq 27°$ is deduced for the DCT molecule with respect to the surface normal (a schematic picture of the DCT orientation on gold surface is shown in fig. 3.18). This is in agreement with previous results in literature for a compact DCT monlayer [100, 101]. In addition, information about the absolute orientation of the CH_3 group can be deduced. Accordingly to ref. [33], a phase of $-\pi/2$ has been assumed for the gold substrate [102]. Because of the r^+ peak in SSP spectrum appears as a deep, this means that a destructive interference with the substrate occurs and, thus, a phase of about $\pi/2$ can be deduced for r^+

	$\omega\,[cm^{-1}]$	$\Gamma\,[cm^{-1}]$	A_{SSP}	A_{SPS}	A_{PPP}
d^+	2856	11.5	0.02	0.16	0.52
r^+	2879	5.9	-0.22	0.06	-0.82
d^-	2935	5	-0.20	0.0	-2.1
r^+_{FR}	2945	15	0.55	0.37	1.3
r^-	2964	5	0.08	0.05	-0.37

Table 3.7: CH_3 resonant amplitudes deduced from the fit of data in fig. 3.16

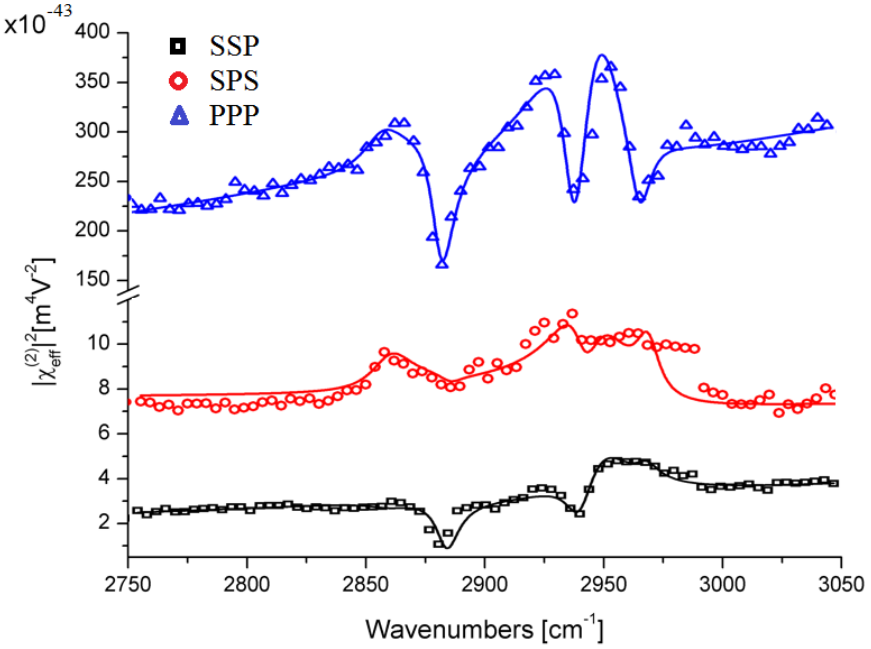

Figure 3.16: SSP (black), SPS (red) and PPP (blue) spctra of DCT SAM on gold surface in aliphatic *CH* stretching region and their best curve fits.

mode from eq. 3.7. This is in agreement with a configuration of the methyl group that orients toward the gas phase [102].

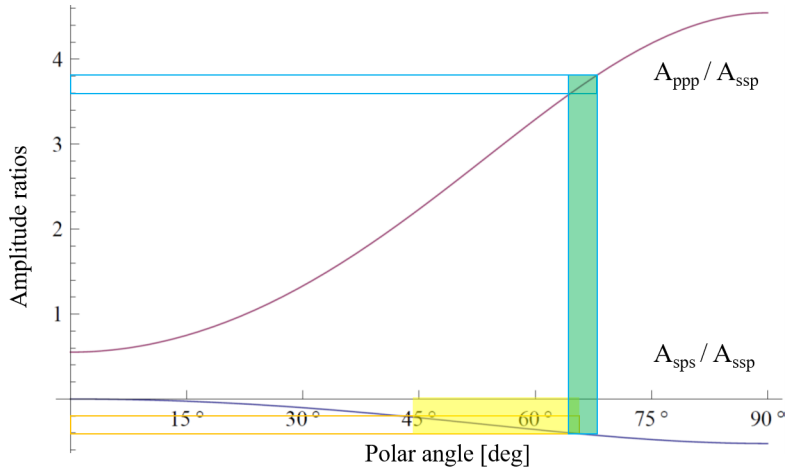

Figure 3.17: Theoretical amplitude ratios as a function of the polar angle θ_{CH_3} for the methyl group. Green and yellow area represent the experimental ranges of the amplitude ratios for r^+ mode.

Based on the reported results, future works will concern the investigation of molecular architectures of SSHB of alkyl-footed cavitands and direct grafting of properly functionalized cavitands, with proper substitution at the lower rim such as tioctic acid, on gold surfaces [63, 93].

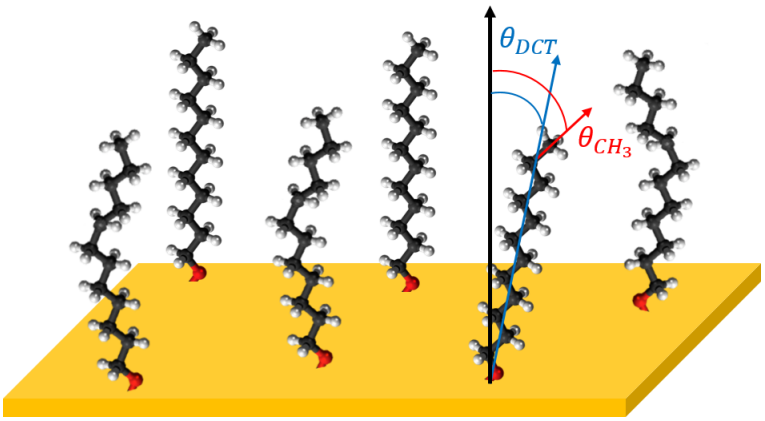

Figure 3.18: Schematic picture of the DCT orientation on gold surface.

Chapter 4

Host-guest complexation at liquid/gas interface

Molecular recognition in liquid phase is widely diffused in living systems, in which the molecular receptors preserve their complexation ability under various conditions as pH or temperature variation, presence of ions or different molecular species. It is not simple for synthetic receptors to reproduce their stability, selectivity and sensitivity in real world operating conditions. Many external factors can affect their performances and, for this reason, the study of recognition events in liquid environment is pivotal to understand how the capability of receptors to engulf guests can be affected. In other words, a thorough understanding of the complexation events is required. In this regard, Langmuir films offer an advantageous model system to study properties of organic films organized on liquid subphases. Being two-dimensional ordered systems of molecules, they have been widely studied in literature allowing to investigate molecular layer directly at the liquid/gas interface under variation of pH [37, 38], temperature [103] and charged molecular species [104]. In this regard, Langmuir films of receptors allow to probe host-guest interactions directly at the interface in the widest possible range of operating conditions. Coupled with SFVS as investigation tool, these give the possibility to deduce structural information and to study complexation capabilities of receptors. In particular molecular conformation of the film, recognition event and host-guest interactions can be studied. For example, QxCav Langmuir films have been previously investigated with SFVS [38] and Second Harmonic Generation (SHG) [37]. In these works the *vase-to-kite* transition of the QxCav has been induced at very low pH, and conformational changes have been observed. In the *kite* configuration, indeed, because of the aperture of the quinoxaline walls, the QxCav loses its capability to engulf guests. In this regard, the conformationally blocked QxCav, namely QxBOX, has been designed and synthesized to be insensitive to temperature and pH variations. Its cavity mouth is bound in the vase configuration in which a rigid con-

formation is achieved with four methylenoxy or ethylenoxy bridges that link the quinoxaline walls to the corresponding neighboring ones. This receptor can be helpful in liquid systems for the control of BTEX critical concentrations in water sources. Its strong sensitivity toward benzene and its derivatives and its strong thermal stability have been demonstrated in a recent work [40, 105]. In this regard, a molecular-level understanding of the host-guest interactions in liquid phase can give information about the receptor efficiency in terms of external factors such as pH, temperature, analyte concentration or presence of different molecular species.

A preliminary investigation of the complexation ability of QxBOX toward aromatic compounds at liquid/gas interface is reported in this chapter. In particular, a QxBOX Langmuir film is realized on the water surface to study the complexation of an aromatic guest dissolved in water phase at different concentrations. The evidence of molecular recognition is reported and the orientation of both cavitand and analyte is deduced from SF spectra, elucidating the geometry of the guest engulfing.

4.1 QxBOX at liquid/gas interface

The QxBOX cavitand is QxCav derivative in which the cavity mouth is blocked in the vase configuration with the addition of four ethylenoxy (or alternatively methylenoxy) bridges that link the quinoxaline walls to the adjacent ones. Reported in fig. 4.1, the molecular structure of the QxBOX with an aromatic guest as toluene engulfed in the cavity mouth thanks to $CH-\pi$ interactions. The *vase*-blocked conformation makes this cavitand insensitive to pH variation and increases its thermal stability [40]. In order to study its complexation capability, it is organized at water/air interface forming a compact and ordered monolayer.

To this purpose, a home-made Langmuir through was designed and built up expressly for the NB-SFG spectrograph. A schematic view of the system is shown in fig. 4.2. A teflon through (a), with a mechanical control of the barrier performed with a microcontroller (b, Arduino UNO R3 + Stepper motor driver Easydriver V44), is coupled with a balance (c, Radwag AS 220.R2) and a Wilhelmy plate (d, Whatman F319-04 filter paper) for the monitoring of the surface pressure. The whole system is controlled with a LabVIEW software (e).

$18\,\mu L$ of 1mM solution of QxBOX in chloroform were spread drop-by-drop on the ultrapure water ($18.2 M\Omega \cdot cm @ 25°C$, Synergy UV Millipore) subphase in the Langmuir through and left for 30 min to allow for complete evaporation of the solvent. The molecules were then compressed to the liquid-condensed phase at a surface pressure of about 20 mN/m (see black line in fig. 4.5). The QxBOX molecules orient their polar head toward the water phase, while the strongly hydrophobic alkyl chains point out to the air. A representation of the QxBOX

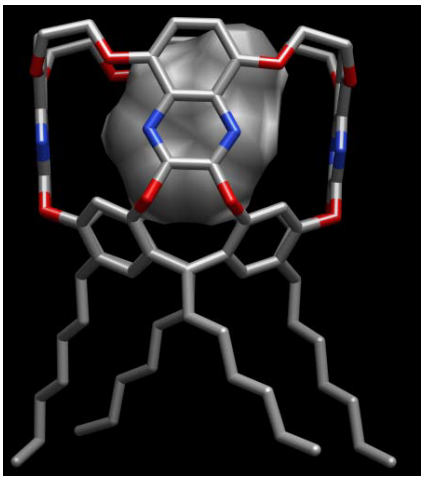

Figure 4.1: Molecular structure of QxBOX-toluene complex (Jakub Waldemar Trzciński, PhD thesis).

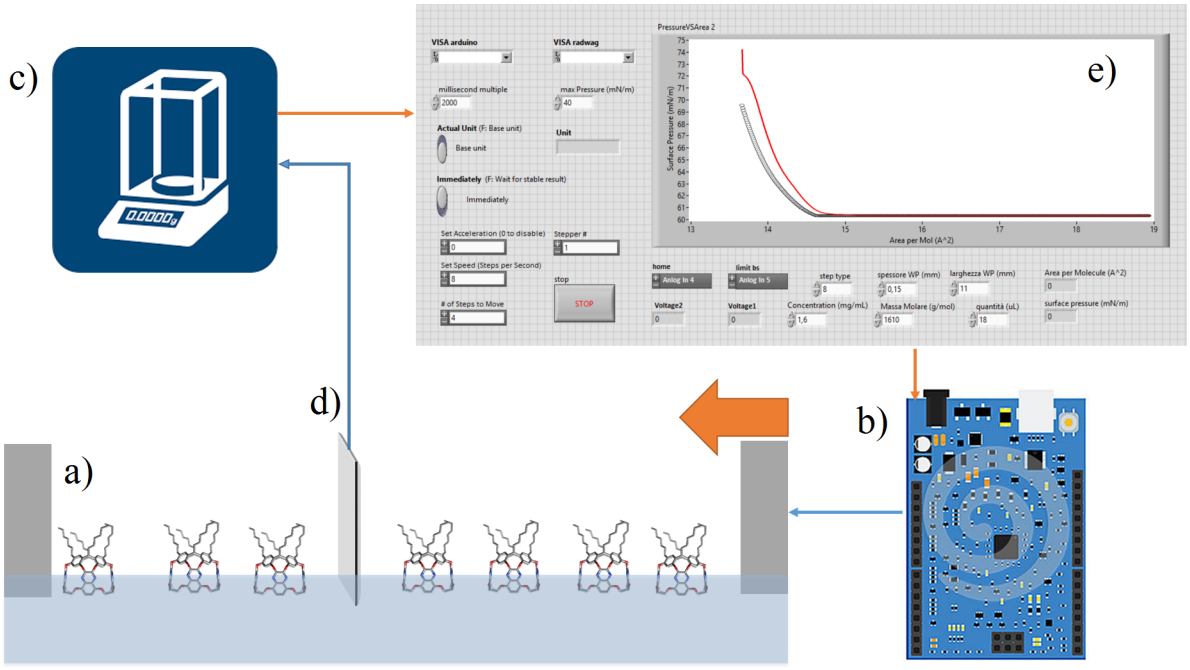

Figure 4.2: Langmuir through coupled with balance and microcontroller connected through LabVIEW interface

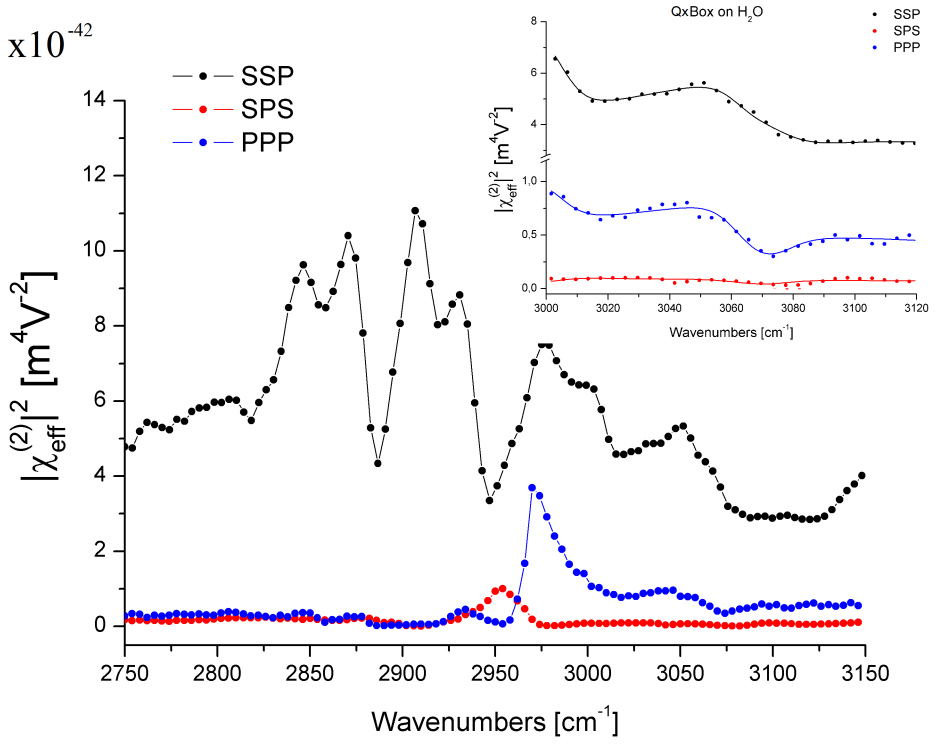

Figure 4.3: SF spectra of a) QxBOX film on ultrapure water at surface pressure of 20 mN/m in the CH stretching region. The inset b) is an enlargement of the spectra in the aromatic stretching region (circles) with their corresponding best curve fits (solid lines).

film is reported in fig. 4.2-a. The SSP, SPS and PPP SF spectra of the QxBOX monolayer in the aliphatic and aromatic CH stretching region $2750-3150\,cm^{-1}$ are reported in fig. 4.3. All the resonances relative to the symmetric and asymmetric stretches of methyl and and methylene groups are present in the range $2750-3000\,cm^{-1}$, due to the alkyl chains of the QxBOX molecules. The CH aromatic stretch in the region $3000-3150\,cm^{-1}$ is assigned to the symmetric stretch mode ν_2 ($3062\,cm^{-1}$) of the quinoxaline walls.

The SSP spectrum in the CH aliphatic region exhibits a prominent symmetric stretch peak of the methylene group, suggesting the presence of *gauche* defects along the alkyl chains, as found for the QxCav Langmuir film [38]. The presence of a peak corresponding to the symmetric stretch ν_2 of quinoxaline moieties is evidence of a net polar orientation of receptors at water/air interface, as expected for an ordered two-dimensional system.

A fit of the data in the CH aromatic range was performed to get information about the molecular orientation of the QxBOX cavity at air/water interface. In particular, the resonant amplitudes of total symmetric stretch ν_2 of the quinoxaline moieties were used for the quantitative analysis. In tab. 4.1 the fit parameters of the spectra shown in inset of fig. 4.3 are

reported.

QxBOX film	$\omega\,[cm^{-1}]$	$\Gamma\,[cm^{-1}]$	A_{SSP}	A_{SPS}	A_{PPP}
ν_2	3062	15	0.56	0.18	0.50

Table 4.1: Fit parameters of SF spectra reported in inset of fig. 4.3

To calculate the average orientation of the QxBOX molecules, the model used in sec. 3.2.2 for the QxCav was assumed. In this particular case, the aperture angle was kept at $\theta_m \simeq 6°$, in agreement with the X-ray analysis [40], because of the *vase*-blocked conformation of the cavity mouth. Using eqs. 3.4 and 1.13 (corresponding Fresnel factors are reported in tab. 4.2) the average orientation of QxBOX cavity can be deduced.

NB-scheme	$\lambda\,(nm)$	$\beta\,(deg)$	n	L_{xx}	L_{yy}	L_{zz}
ω_{SF}	460	59	1.336	1.05	0.67	0.68
ω_1	532	60	1.334	1.07	0.66	0.67
ω_2	3400	55	1.456	0.99	0.65	0.72

Table 4.2: Fresnel factors for QxBOX film at air/water interface

In fig. 4.4 the amplitude ratios as a function of the polar angle θ_p are shown, assuming and ODF $f(\Omega) = \delta(\theta - \theta_p)/4\pi^2 \sin\theta_p$. The resonant amplitudes for the total symmetric stretch of the quinoxaline walls give an average orientation of the QxBOX molecules of about $\theta_p \simeq 37° \pm 6°$ with respect to the surface normal, as shown in inset of fig. 4.4.

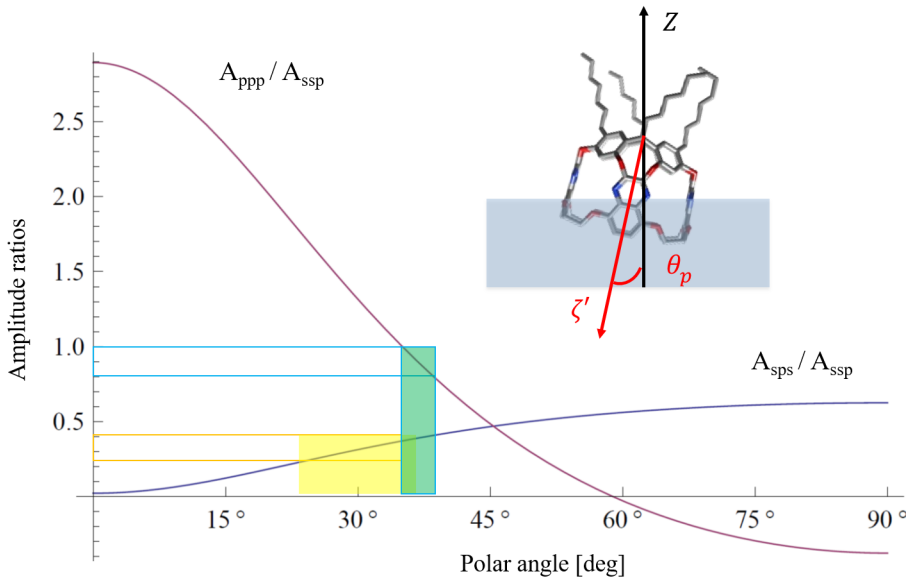

Figure 4.4: Amplitude ratios $A_{\nu_2,SPS}/A_{\nu_2,SSP}$ (in blue) and $A_{\nu_2,PPP}/A_{\nu_2,SSP}$ (in purple) for the ν_2 mode as a function of the polar angle θ in the simple case of Dirac delta ODF. The inset is a representation of QxBOX average orientation at air/water interface.

4.2 Molecular recognition at water/air interface

After the characterization of the Langmuir film, the QxBOX monolayer was compressed on a benzonitrile solution in water to have evidence of molecular recognition of aromatic guests dispersed in the water phase at water/air interface. Benzonitrile solutions were prepared at different concentrations: 8, 20 and 40 mM in ultrapure water. Because of the poor solubility of benzonitrile in water ($\sim 2g/L$), the solutions were stirred for 2 hours at 30°. The SSP spectrum of the benzonitrile solution (20mM) in water in the CN stretching range is reported in the inset of fig. 4.5, where the peak at 2240 cm^{-1} indicates a net polar orientation of the benzonitrile molecules at water/air interface, as shown in previous works on nitrile-monosubstituted aromatic compounds [86, 106]. The CN stretching peak intensity is then measured in presence of the QxBox film in order to observe if the cavitand layer affect the arrangement of analyte molecules at the interface. In this regard, 18 μL of 1mM solution of QxBOX in chloroform were spread on the benzonitrile solutions (20mM) drop-by-drop. After solvent evaporation, the film was compressed in the liquid-condensed phase up to 18mN/m, that corresponds to an area per molecule of about 90 $\AA$. In fig. 4.5 the QxBOX compression curve (black line) is reported as a function of the area per molecule. The CN stretch peak intensity was monitored during the compression of the cavitand monolayer and, as evident in fig. 4.5, the SF signal

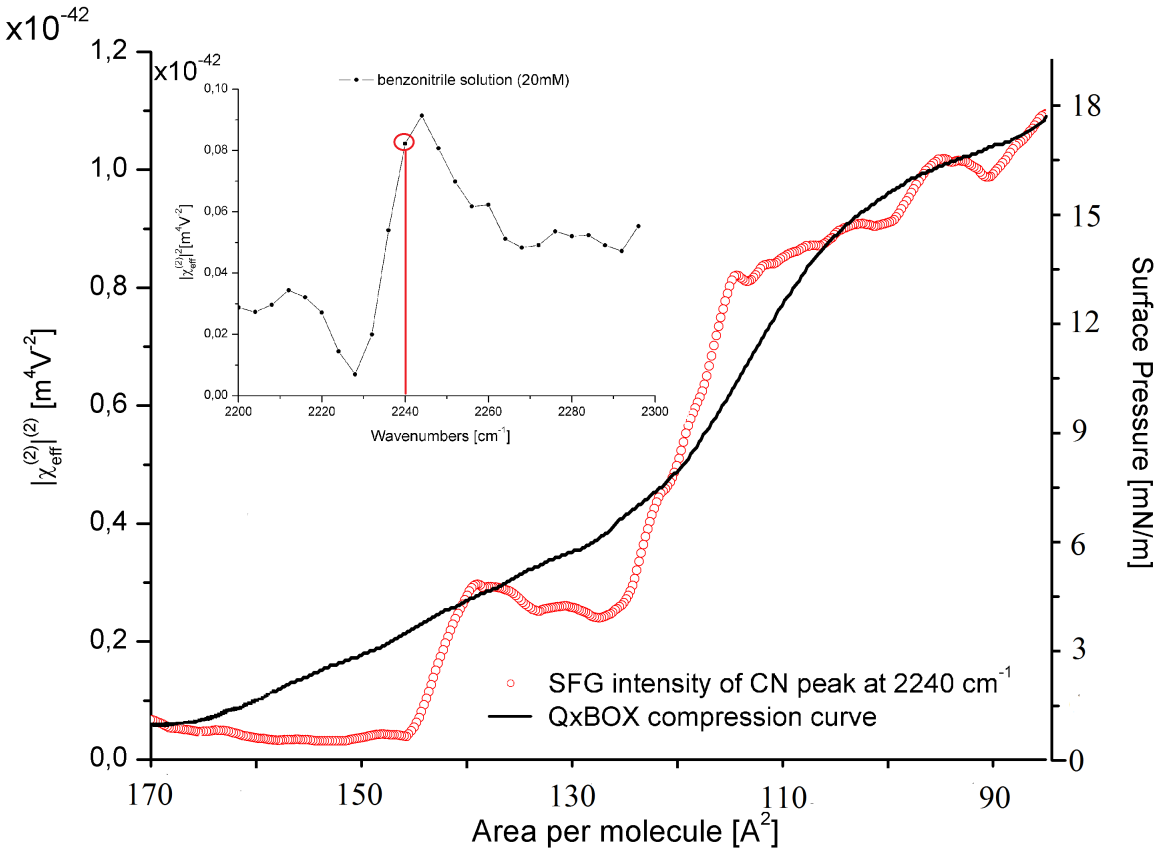

Figure 4.5: Compression curve of QxBOX film (black line) on benzonitrile solution (20mM) and SF intensity of CN stretch (red circles) as a function of the area per molecule. In inset the SSP spectrum of the sole benzonitrile solution (20mM).

at $2240\,cm^{-1}$ (red circles) increases with the reduction of the area per molecules. Furthermore, the CN signal at low value of the area per molecule ($\simeq 90\,\mathring{A}$) is one order of magnitude higher than that of the sole benzonitrile in water. This means that the presence of the receptor monolayer affects the benzonitrile surface density. The compression of the sole benzonitrile solution, indeed, does not change the surface pressure or the intensity of the CN stretch. Therefore, the increasing of the CN peak is due to the benzonitrile molecules engulfed in the QxBOX binding cavities.

In fig. 4.6 the SSP, SPS and PPP spectra of the QxBOX film at a surface pressure of 20mN/m on benzonitrile solution at 8 (b), 20 (c) and 40 (d) mM are reported in the CH aliphatic and aromatic stretching region, to highlight possible changes due to the analyte concentration in water phase. In the range $2750 - 3000\,cm^{-1}$ no significant changes are observed that suggest variation in the alkyl chain conformation versus benzonitrile concentrations, while

the aromatic part $3000-3150\,cm^{-1}$ shows a different behavior.

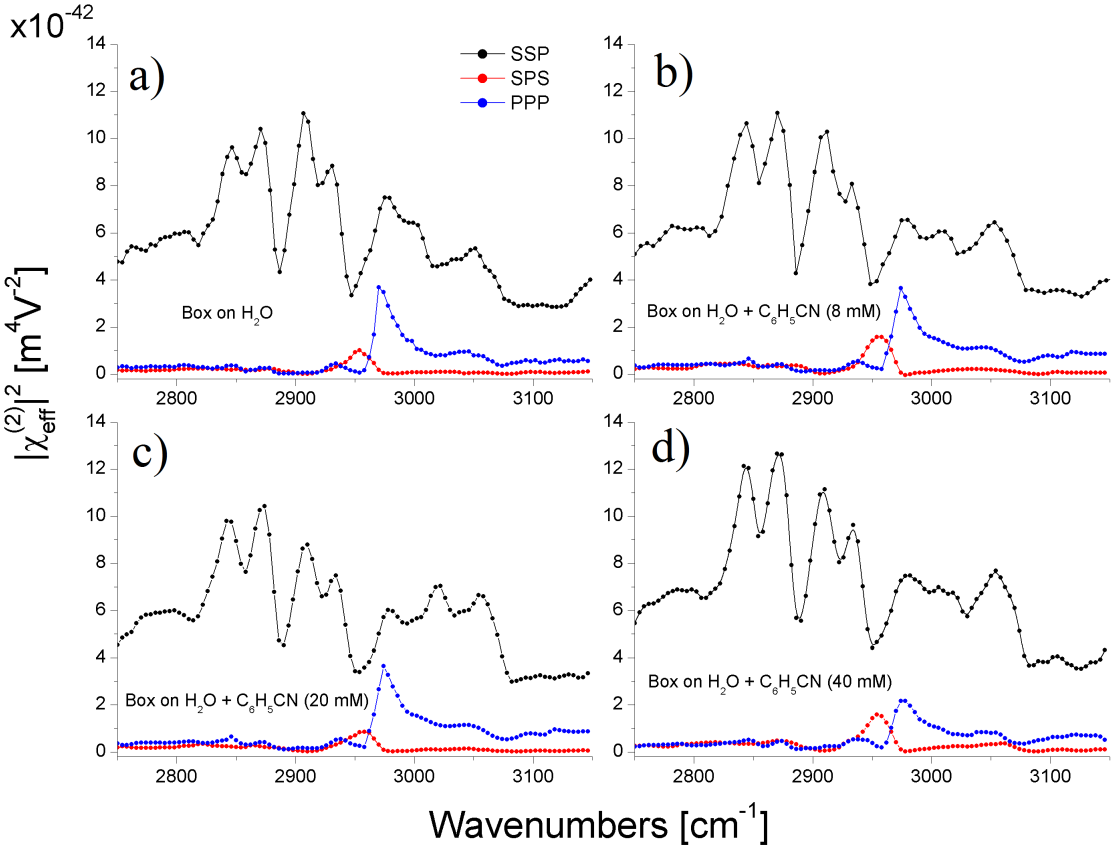

Figure 4.6: SSP (black circles), SPS (red circles) and PPP spectra (blue circles) spectra of QxBOX film on a) water and on benzonitrile solution in water at b) 8 mM, c) 20mM and d) 40mM in the CH aliphatic and aromatic stretching region.

In fig. 4.7, an enlargement of the SSP spectra showed in fig. 4.6 in the CH aromatic range (black circles) is reported. From the best curve fits (black lines), the resonant amplitudes for the QxBOX on water (a) and on benzonitrile solutions at 8 (b), 20 (c) and 40 (c) mM have been deduced. The red, blue and green lines, respectively, represent their contribution to the spectra. The amplitude of the symmetric stretching ν_2 and ν_{20} increase with the concentration of benzonitrile in solution, whose aromatic group exhibits a resonance at about $3080\,cm^{-1}$. The SSP spectrum of the sole benzonitrile solution (20mM) in the CH aromatic range is reported in fig. 4.7-c to for comparison.

In addition, the CN stretch region is also investigated to obtain information about the analyte orientation at the interface. In fig. 4.8 the SSP and SPS spectra of QxBOX film on benzonitrile solution at 8 (a), 20 (b) and 40 (c) mM. In all spectra a peak at about $2240\,cm^{-1}$ indicates the complexation of benzonitrile molecules with a net polar orientation. The intensity

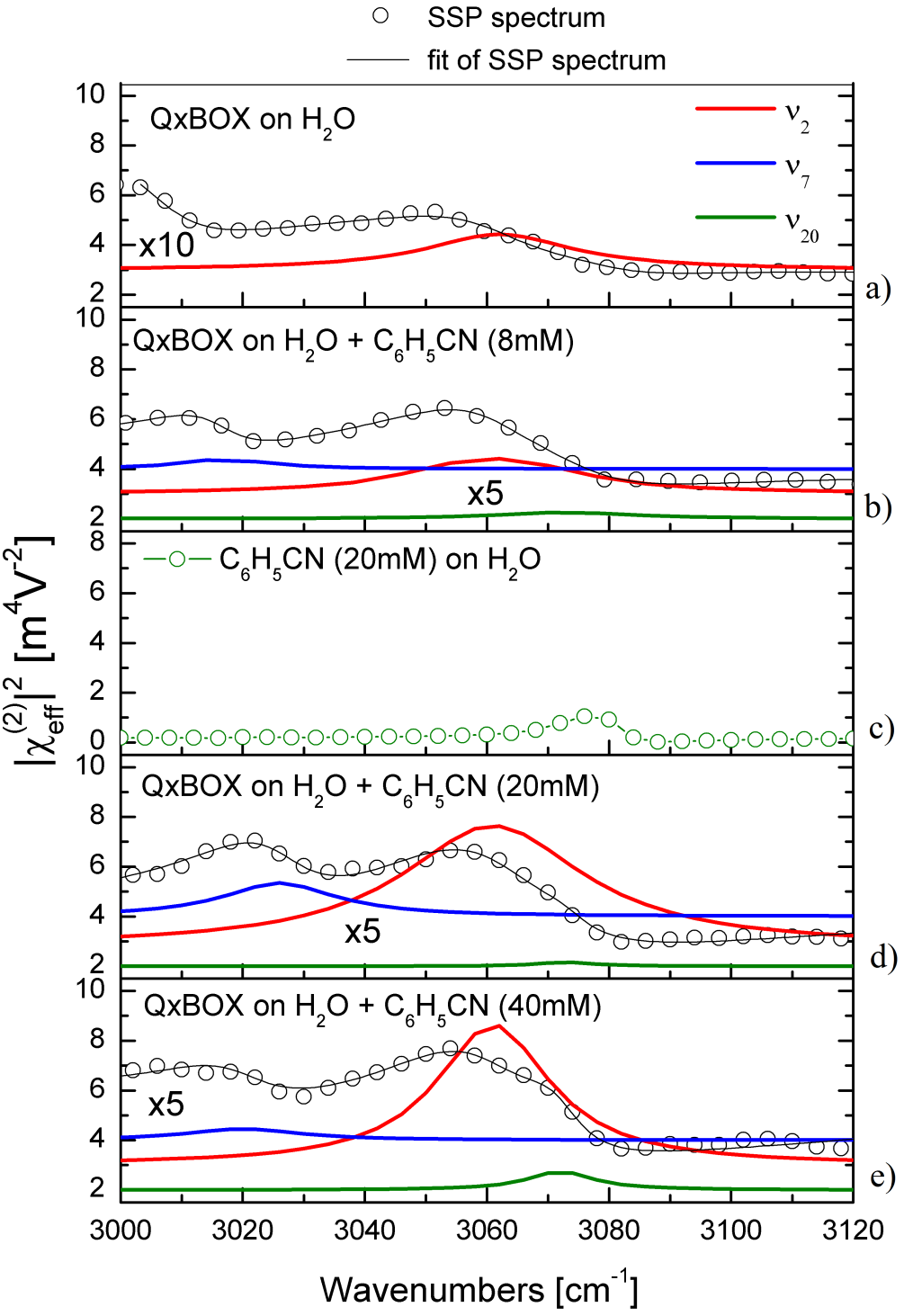

Figure 4.7: SSP spectra (black circles) of a) QxBOX on pure water and benzonitrile solutions at b) 8, d) 20 and e) 40mM in the CH aromatic stretching region with their corresponding best curve fits (black lines). The red, green and blue lines are the contribution of the mode ν_2 ,ν_{20} , and ν_7 resonances to the spectra. Green circles in c) represent the SSP spectrum of the sole benzonitrile in solution (20mM) in the CH aromatic range.

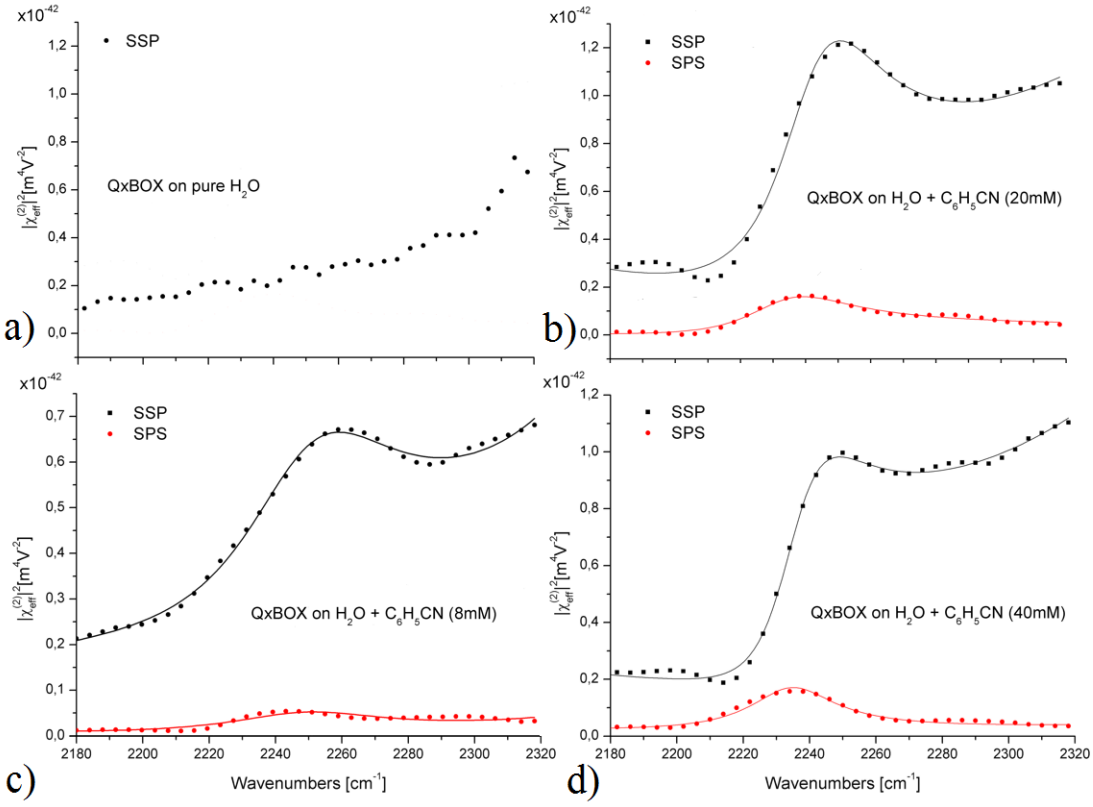

Figure 4.8: SSP (black circles) and SPS (red circles) spectra of QxBOX film on a) pure water and on benzonitrile solution at c) 8 mM, b) 20mM and d) 40mM in the CN stretching region. The solid lines are their corresponding curve fits.

in the SSP spectrum for the 20 mM solution is higher with respect that at 8 mM, indicating a larger number of complexed molecules. No significant difference are observed between the 20 and 40 mM case, probably due to a saturation of the disposable complexation sites. In addition, the resonance frequency exhibits a red shift at higher concentrations (see tab. 4.3), as shown in ref. [106]. For the sake of clarity the SSP sectrum of the QxBOX on pure water is reported in fig. 4.8-b (dashed line) which accounts for the shape of the CN peak due to the non-resonant contribution. The parameters deduced from the best curve fits of the data (shown as solid lines) are reported in tab. 4.3. The contribution to the CN peak due to "free" benzonitrile oriented at the interface is neglected in the following calculations because, as mentioned before, is one order of magnitude lower than that of the complexed molecules.

The data presented in fig. 4.8 have been fitted (solid lines) and the corresponding parameters are reported in tab. 4.3. Assuming as ODF for the CN group $f(\Omega) = \delta(\theta - \theta_{CN})/4\pi^2 \sin\theta_{CN}$, its average orientation can be deduced from the resonant amplitudes of SSP and SPS spectra through eqs. 3.5 and 1.13. The theoretical amplitude ratios are reported

in fig. 4.9 for the assumed ODF.

C_6H_5CN concentration	$\omega\,[cm^{-1}]$	$\Gamma\,[cm^{-1}]$	A_{SSP}	A_{SPS}	A_{SPS}/A_{SSP}	θ_{CN}
$8\,mM$	2246	30	0.80	0.32	0.4	$41° \pm 11°$
$20\,mM$	2242	20	2.52	0.96	0.38	$38° \pm 7°$
$40\,mM$	2235	14	2.10	0.75	0.36	$37° \pm 4°$

Table 4.3: Fit of the CN stretching mode for QxBOX film

The average values of the polar angle θ_{CN} at different concentration are reported in tab. 4.3 and indicate that the benzonitrile molecules form an angle of about $\theta_{CN} \simeq 38°$ with the surface normal. This result is in perfect agreement with the hypothesis of an on-axis complexion of the guest inside the receptor cavity, being this angle very close to that obtained for the QxBOX molecule $\theta_p \simeq 37°$. In addition, the polar angle θ_{CN} does not depend on the concentration of the analyte in solution, demonstrating that the average orientation of the benzonitrile only depends on the conformation of the uppermost cavitand layer.

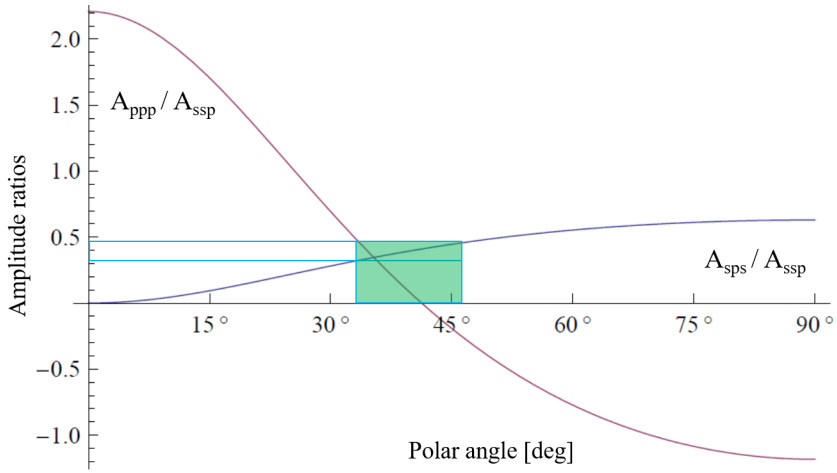

Figure 4.9: Amplitude ratios $A_{CN,SPS}/A_{CN,SSP}$ (in blue) and $A_{CN,PPP}/A_{CN,SSP}$ (in purple) for the *CN* mode as a function of the polar angle θ in the simple case of Dirac delta ODF. Green area represents the experimental amplitude ratio for CN stretch.

Furthermore, the benzonitrile molecules prefer a configuration with the CN group that points toward the water phase [106] while the aromatic moiety is hosted inside the receptor cavity, as found for the QxCav SSHB case in chapter 3. This leads to the conclusion that the benzonitrile molecule is complexed with its main axis parallel to that of the QxBOX cavitand with the nitrile group that points toward the water subphase.

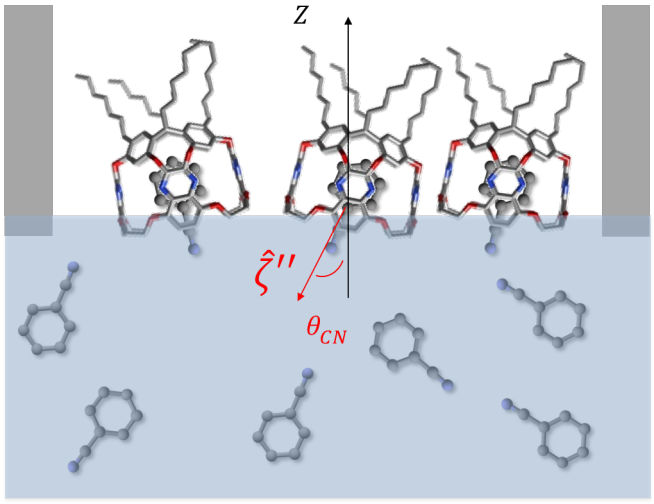

Figure 4.10: Schematic diagram of the benzonitrile complexation inside the QxBOX cavity, at the air/water interface.

The investigation of QxBOX Langmuir film by SFVS has allowed to study the host-guest interactions directly at liquid/gas interface, making possible the reconstruction of the physical picture of the complexation process, that is schematically depicted in fig. 4.10.

4.3 QxCav at water/air interface: quantitative comparison with QxBOX film

In this section the previous results obtained for QxBOX film are compared with those of a QxCav monolayer in the same experimental conditions. The main goal of this study is to highlight possible differences in terms of host-guest complexation efficiency and geometry between the two cavitands. The ability of QxCav to engulf aromatic compounds has been tested at water/air interface for recognition of benzonitrile dispersed in the liquid phase. The QxCav film is compressed until it reaches a surface pressure of 20mN/m on a 20mM benzonitrile solution in water. From the quantitative analysis on the CN stretching mode, the average orientation of the complexed molecules is deduced and their molecular density is compared with that of the QxBOX film.

In fig. 4.11 the SF spectra of a QxCav monolayer on ultrapure water are reported for SSP, SPS and PPP polarization configuration at the surface pressure of 20mN/m in the CH aliphatic and aromatic stretching region $2800-3100\,cm^{-1}$. All the symmetric and asymmetric stretching modes of methyl and methylene groups are present in the range $2800-3000\,cm^{-1}$ due to the alkyl chains of QxCav molecules, while aromatic stretching modes of the quinoxaline

QxCav film	$\omega\,[cm^{-1}]$	$\Gamma\,[cm^{-1}]$	A_{SSP}	A_{SPS}	A_{PPP}
ν_7	3040	13	0.24	0.26	-0.29
ν_2	3065	7	1.07	0.27	0.24
ν_{20}	3080	8	-0.61	0.10	-0.16

Table 4.4: Fit parameters of SF spectra reported in inset of fig. 4.11

moieties are clearly visible in the region $3000-3100\,cm^{-1}$, whose enlargement is shown in the inset of fig. 4.11, where the experimental data are reported with their corresponding best curve fits.

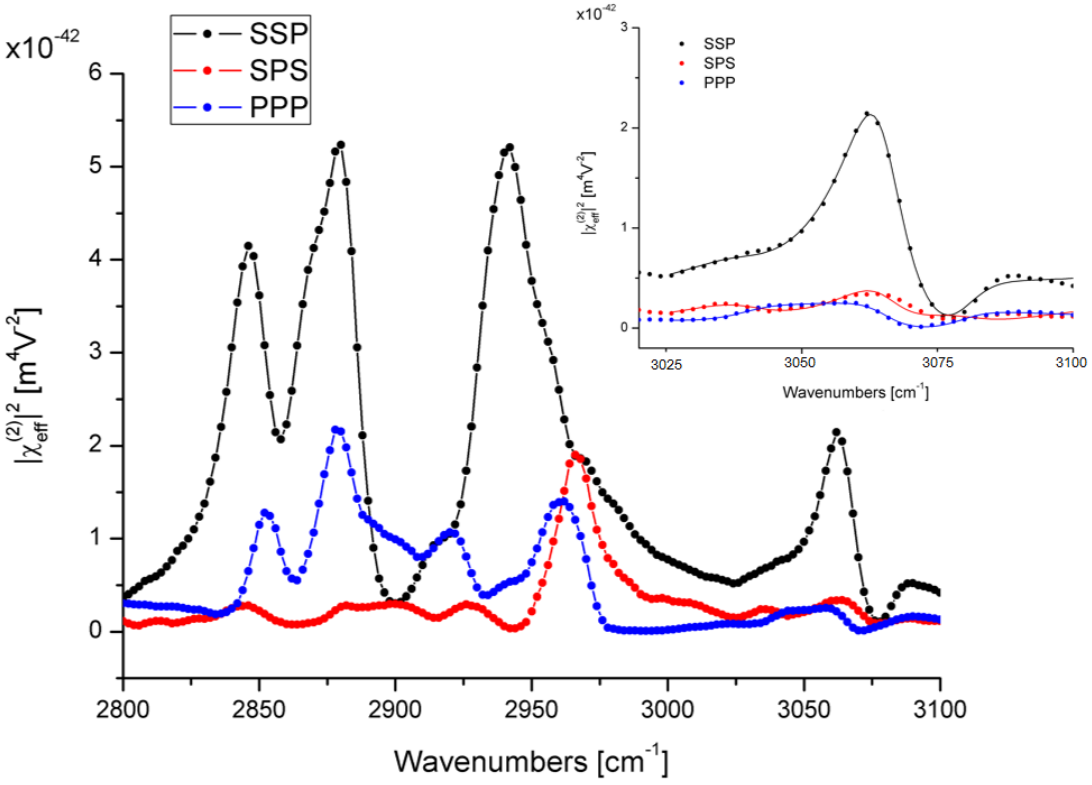

Figure 4.11: SF spectra of a) QxCav film on ultrapure water at surface pressure of 20 mN/m in the CH stretching region. The inset b) is an enlargement of the spectra in the aromatic stretching region (circles) with their corresponding best curve fits (solid lines).

In order to deduce the average orientation of the QxCav molecules a quantitative analysis on the ν_2 mode is carried out assuming the model adopted in chapter 3 (subsec. 3.2.2). The fit parameters of the spectra in the CH aromatic region are reported in tab. 4.4. From the quantitative analysis on the ν_2 mode a polar angle of $\theta_p = 40° \pm 8°$ and aperture angle of

$\theta_m = 5° \pm 2°$ for the QxCav are calculated. These results indicate that the QxCav is in a *vase* configuration with its main axis oriented at 40° with respect to the surface normal. This analysis confirms that the QxCav orientation at water/air interface is very close to that of the QxBOX previously discussed. To compare the performances of these two cavitands in terms of complexation efficiency, the experiment is repeated after the addition of benzonitrile (20mM) in the water subphase. In fig. 4.12, the CN signal (red circles) and the compression curve of the QxCav film on benzonitrile solution (20mM) as a function of the area per molecule. The surface pressure is increased up to about 25mN/m, that corresponds to a $90 \mathring{A}^2$ area per molecule (as shown in fig. 4.5 for the QxBOX film). At first sight, comparing the CN signal of fig. 4.12 and 4.5, a difference between absolute intensity for the two cavitand films can be noticed at the same area per molecule. For the QxBOX case a larger value of the CN signal is achieved at about $90 \mathring{A}^2$ suggesting a higher density of the complexed benzonitrile molecules at the water/air interface. In order to make a direct comparison between the densities of engulfed guests for QxCav and QxBox films, a quantitative analysis on the CN mode for the QxCav monolayer is also required.

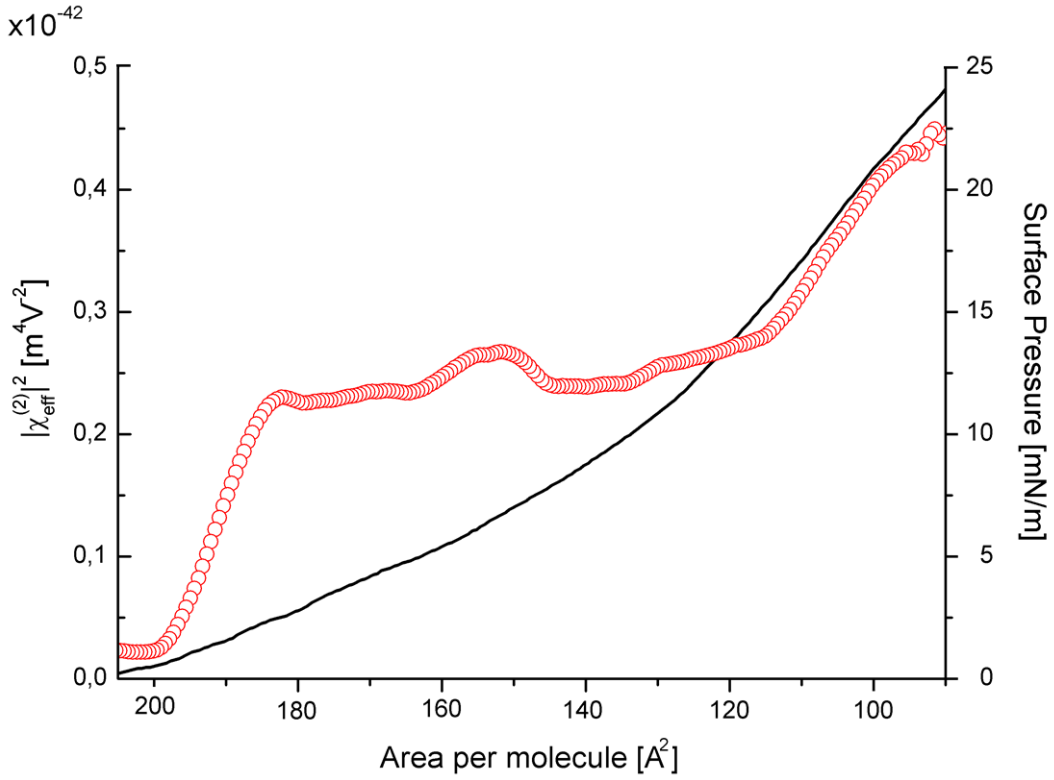

Figure 4.12: Compression curve of QxCav film (black line) on benzonitrile solution (20mM) and SF intensity of CN stretch (red circles) as a function of the area per molecule.

C_6H_5CN concentration	$\omega\,[cm^{-1}]$	$\Gamma\,[cm^{-1}]$	A_{SSP}	A_{SPS}	A_{SPS}/A_{SSP}	θ_{CN}
$20\,mM$	2233	12	0.88	0.29	0.33	$34° \pm 6°$

Table 4.5: Fit of the CN stretching mode for QxCav film

In fig. 4.13 the SSP (black circles) and SPS (red circles) spectra of the QxCav film on benzonitrile solution (20mM) are reported in the CN stretching region. A prominent peak at about $2240\,cm^{-1}$ is clearly visible in the SSP spectrum and it is assigned to the CN stretch. From the fits of the experimental data (corresponding solid lines) and assuming the ODF $f(\Omega) = \delta(\theta - \theta_{CN})/4\pi^2 \sin\theta_{CN}$, the average orientation of the CN group $\theta_{CN} = 34°$ is deduced.

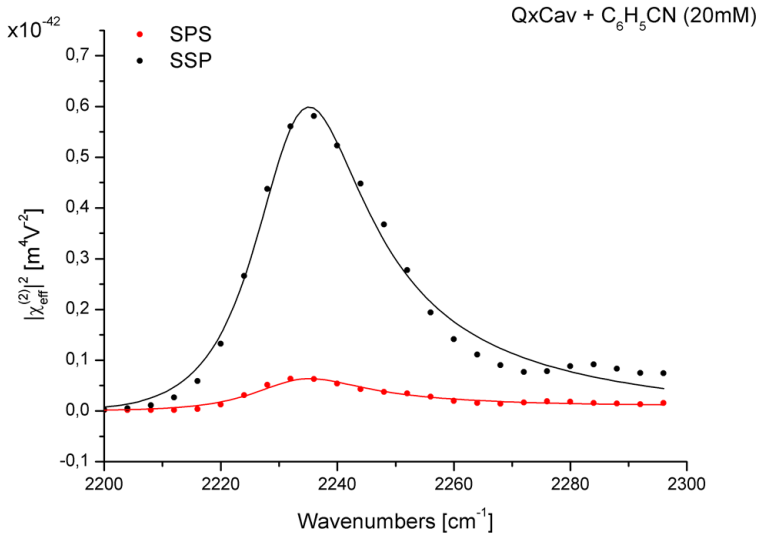

Figure 4.13: SSP (black circles) and SPS (red circles) spectra of QxCav film on benzonitrile solution at 20mM in the CN stretching region. The solid lines are their corresponding curve fits.

This average orientation is compatible with an *on-axis* inclusion of the guest in the cavity mouth of the QxCav, in agreement with the results obtained for the QxBOX film. The relative surface density of the engulfed benzonitrile molecules for the QxCav and QxBOX monolayers, estimated from the ratio between the amplitudes $A_{CN,xxz}$ (see eqs. 3.5), is about $N_{CN}^{(QxBOX)}/N_{CN}^{(QxCav)} \simeq 2$. This result confirms that the ability of QxBOX film to engulf aromatic guests is about two times higher than that of QxCav one, probably due to the rigid structure of its cavity mouth. Indeed, it has been recently proposed that QxBox is able to strengthen the host-guest interactions and enhances the complexation efficiency toward monosubstituted benzene guests, with respect to the QxCav. Thanks to its conformationally blocked configura-

tion QxBOX increases the stability of the complexes avoiding the release of guests due to the vibrations of the quinoxaline walls.

Conclusions

In summary, different cavitand architectures and their complexation ability toward aromatic compounds at solid/gas and liquid/gas interfaces were investigated. In particular the average orientation of both receptors and ligands was deduced from SF spectra, allowing a reconstruction of the physico-chemical picture of the *complexes*. The QxCav hybrid bilayers on top of two different hydrophobic templates, namely OTS and DMOAP, at air/fused silica interface were investigated. The SFVS was used to describe their conformation and to understand how the density and order of the underlayer templates affected the transfer ratio of the cavitand layer by Langmuir–Schaefer method, demonstrating a more efficient QxCav coverage for the loosely packed DMOAP template, 2.5 times denser than that obtained on top of the OTS SAM. The conformation of the QxCav SSHBs was deduced for both the DMOAP and OTS templates, demonstrating that QxCav preserves the *vase* configuration, with an aperture angle of about 20°, and points its cavity toward the gas phase. Based on these results, a viable strategy was proposed to improve the cavitand surface density in SSHBs, which is of paramount importance for the potential applications of such architectures in chemical and biochemical sensing. In this regard, the complexation capability of a QxCav layer transferred on a mixed alkylsilanes SAM (characterized by a lower molecular density at the upper rim) was tested, as well its selectivity toward aromatic compounds. In particular, by probing the solid-gas interface in the aromatic CH and CN stretching ranges, the average polar orientation of the QxCav binding pocket and of the engulfed benzonitrile molecules was deduced, revealing an "on-axis" complexation.

The first evidence of recognition event by SFVS was proved also at the liquid/gas interface, where a Langmuir film of QxBOX cavitands was compressed on the water subphase containing different concentrations of the target molecules. From the analysis of the CH aliphatic and aromatic stretches, the molecular architecture of the receptors was inferred together with the average orientation of the host and guest molecules. An on-axis inclusion of the analyte inside the host binding site was deduced, confirming the same complexation geometry found for the QxCav SSHB at air/fused silica interface.

These results provided a first molecular level picture of chemical recognition at the inter-

faces, close to the actual environment for sensing applications, demonstrating that SFVS is an effective noninvasive tool to investigate both the molecular architecture of receptor decorated surfaces and the host–guest association at the interfaces.

The work presented in this thesis paves the way to a different approach in the study of host-guest interactions at the interfaces, with a technique as SFVS that allows *in-situ* investigation of recognition events. This could lead to more rational design and synthesis of receptors as well as to correlate the *complexation* phenomena that occur at surfaces, essential for transduction mechanisms, to the conformation and arrangement of the receptor layer. SFVS has been proved to be a versatile technique to study *complexes* at the interfaces and to elucidate the geometry of the analyte inclusion within the receptor cavity. Starting from these results, many goals can be achieved. The direct anchoring of the receptors, with proper substitutions at the lower rim, on technologically relevant surfaces could have a huge impact for all the possible chemical and bio-chemical sensing applications. In this frame, a technique as SFVS can help to optimize chemosensor performances in terms of organization and conformation of the receptors at the interfaces. Furthermore, the study can be extended to other host molecules and ligands. For instance, tetraphosphonate cavitands, ideal for recognition of illicit drugs and aminoacid, could be probed in liquid environment exploiting the wider possible range of external conditions, as temperature or pH, allowing to test such receptors in real world operating conditions. Complexation capability of COOH-QxCav toward nitroaromatic compounds could be studied because the detection of explosives in air, soil and liquids it is still an open challenge that demands selective and sensitive devices.

Appendix A

Fluorescence of QxBOX as transduction method for host-guest complexation

Recently, the acquisition of a tunable femtosecond laser system coupled with a streak camera with high spectral and temporal resolution has allowed us to carry out the first measurements of time-resolved fluorescence spectroscopy. In particular, preliminary analysis have been performed on the QxBOX cavitand in solution, because of its intense fluorescent emission in the visible range under UV light excitation, that can offer advantages in terms of transduction mechanism. In this sense, simultaneous static and time-resolved fluorescence spectroscopies have been used to study complexation phenomena and to elucidate how the presence of the analyte in solution can affect the QxBOX emission.

Several fluorescent receptors, indeed, have been synthesized [107, 108] and their complexation capabilities have been probed and demonstrated by fluorescence spectroscopy [108–111]. Here a first preliminary study of the QxBox fluorescence activity in solution is presented, in order to probe the formation of *complexes* due to the presence of guest molecules in solution. Both static and time-resolved fluorescence measurements have been carried out. The theory of fluorescence spectroscopy is beyond the scope of this appendix and can be found elsewhere [112], but its basic principles are summarized here to guide the reader in the following analysis. The normalized fluorescence intensity can be written as:

$$\left(\frac{I_0}{I}\right) = (1 + k_D[Q])\,(1 + k_a[Q]) \tag{A.1}$$

where I_0 and I are the intensities of the sole emitters in solution and after addition of quencher, $[Q]$ is the quencher concentration, while k_D and k_a are the dynamic Stern-Volmer and the association rate constants, respectively. The terms $(1 + k_D[Q])$ and $(1 + k_a[Q])$ account for the dynamic and the static quenching processes.

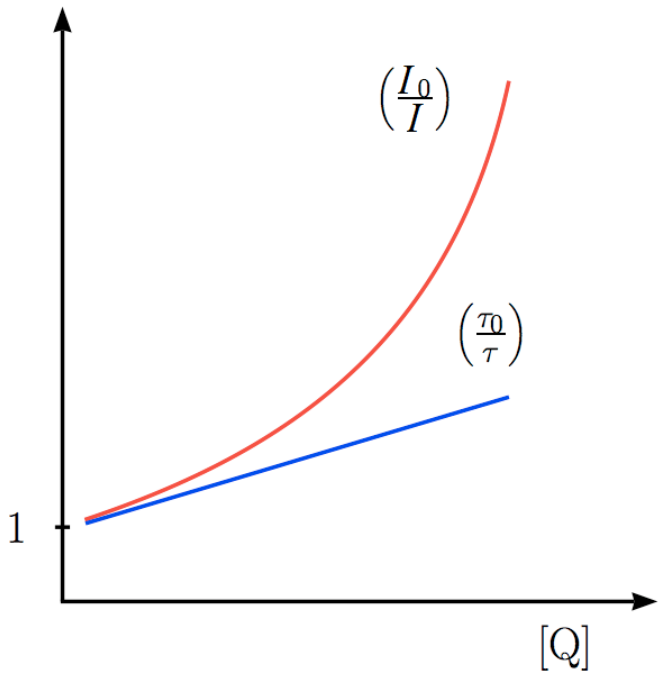

Figure A.1: Plots of eqs. A.1 (red line) and A.2 (blue line)

The first one is related to a non-radiative energy transfer due to the collisions between emitter and quencher or to the overlap between their absorption spectra, while the second one is due to the formation of *complexes* in solution. The dynamic quenching is related to the lifetime through the following equation:

$$\frac{\tau_0}{\tau} = 1 + k_D[Q] \tag{A.2}$$

where τ_0 and τ are the lifetimes of the sole fluorescent molecules and after the addition of the quencher. These two terms can be deduced from the time-resolved fluorescence measurements (as those shown in fig. A.3), allowing to calculate the value of k_D. In order to evaluate the contribution due to the static quenching, it is useful to write the eq. A.1 as:

$$\left(\frac{I_0}{I}\right) / \left(\frac{\tau_0}{\tau}\right) = 1 + K_a[Q] \tag{A.3}$$

From static fluorescence measurements, the intensities I_0 and I can be deduced, and the constant k_a finally calculated. It is important to notice that static quenching does not affect the lifetime of a process, whose variation only depends on dynamic quenching [113].

In this regard, both static and time-resolved fluorescence spectroscopies have been used to investigate how the presence of the analyte in solution can affect the response of the emitting

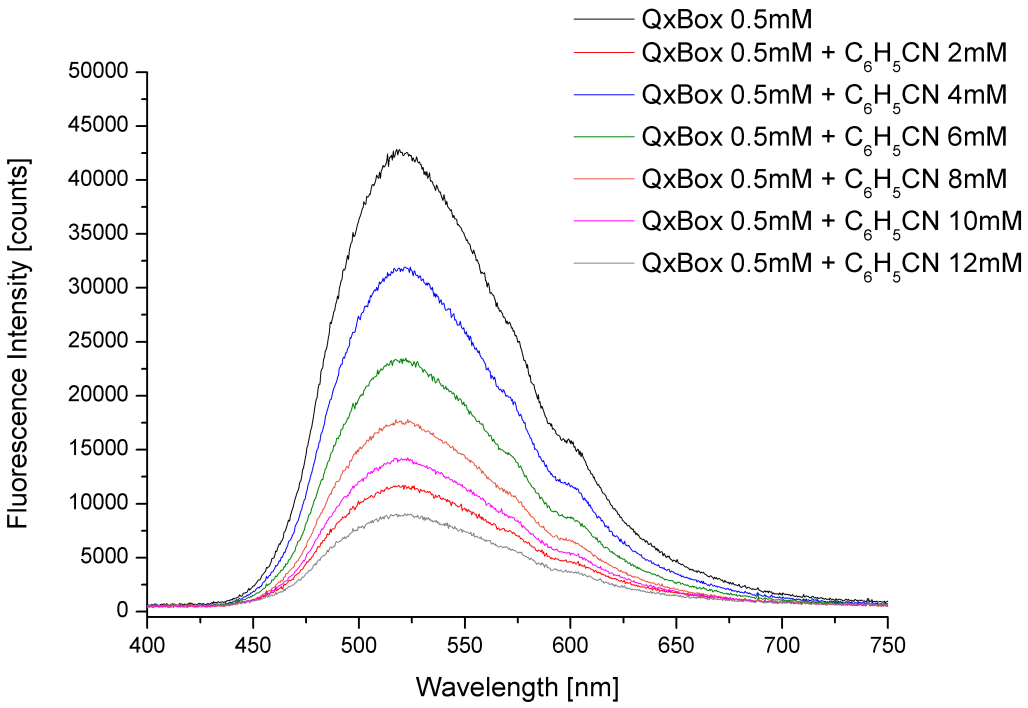

Figure A.2: Fluorescence intensity of the sole QxBOX 0.5mM in acetone (black line) and after addition of benzonitrile (2-12mM).

QxBOX molecules. The static fluorescence spectra have been acquired with a commercial spectrometer (USB2000+, Ocean Optics) for the sole QxBOX 0.5mM in acetone and after the addition of benzonitrile with concentration ranging in 2-12mM. The fluorescence spectra are reported in fig. A.2 in the spectral range 400-750 nm. The broad peak centered at about 520 nm is due to the QxBOX molecules. After the addition of the analyte in solution, a quenching of the fluorescence peak is observed (peak intensity for each curves is reported in tab. A.2). In order to understand the mechanism of the quenching process, complementary time-resolved fluorescence measurements have been carried out. A 400 nm femtosecond laser (20 μJ, 130 fs) was used to pump the samples and the signal has been analyzed with a streak camera (Universal Streak Camera C10910-01 + Slow Single Sweep module M10913-01, Hamamatsu) in the spectral range 490-580 nm in a temporal window of 100 ns with temporal resolution of 20 ps. Shown in fig. A.3 the fluorescence emission at about 520 nm for the sole QxBOX (a) and after the addition of the analyte 12mM (b) as a function of time.

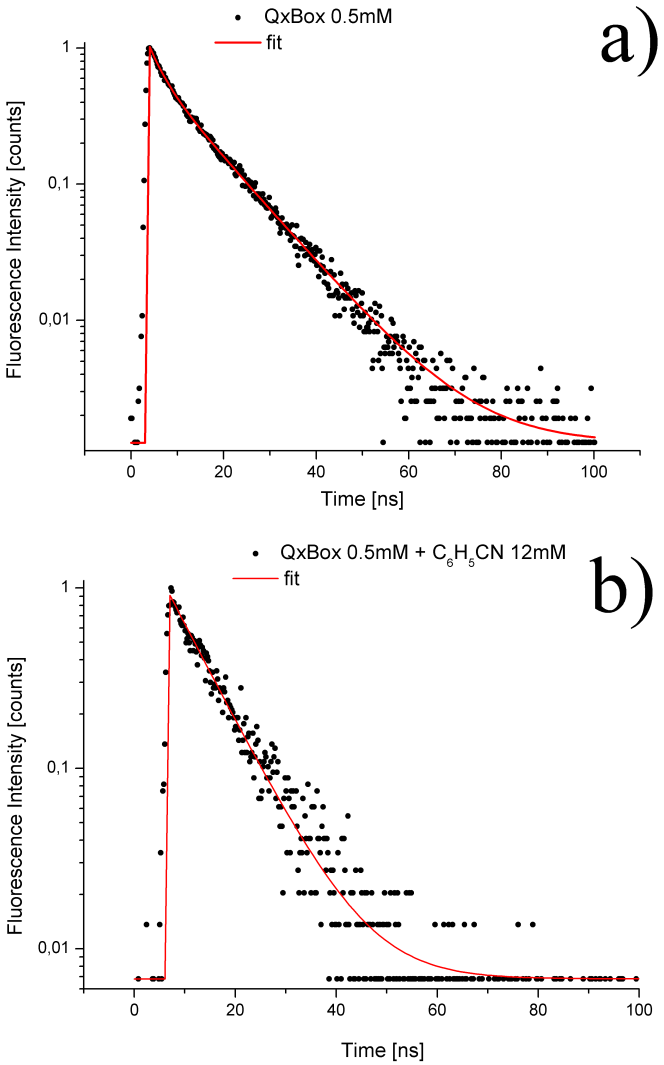

Figure A.3: Fluorescence intensity (black circles) at 520 nm for the sole QxBOX 0.5mM (a) and after addition of benzonitrile 12mM (b) as a function of time. The solid lines represent the corresponding best curve fits.

Their fit parameters, with those of other intermediate concentrations, are reported in tab. A.1. Two different emission processes can be observed for the sole QxBOX and at low concentration (2mM) of the analyte, one faster with a lifetime of 2.87 ns and a second one with a longer lifetime of 11.21 ns. Increasing the benzonitrile concentration the shorter time disappears while the longest time decreases (see inset of fig. A.3), indicating that dynamic quenching occurs. For the 0-2mM analyte concentrations an average lifetime has been calculated

as:

$$\overline{\tau} = \sum_i f_i \tau_i \qquad \text{where} \qquad f_i = \frac{A_i \tau_i}{\sum_i A_i \tau_i} \tag{A.4}$$

[Q] mM	A_1	$\tau_1(ns)$	A_2	$\tau_2(ns)$	$\sum_i A_i \tau_i$	f_1	f_2	$\overline{\tau}([Q])$
0	0.37	2.87	0.65	11.21	8.37	0.13	0.87	10.16 $(=\tau_0)$
2	0.24	2.35	0.75	10.5	8.48	0.07	0.093	9.95
4	-	-	1	9.50	-	-	-	9.50
6	-	-	1	9.13	-	-	-	9.13
8	-	-	1	8.83	-	-	-	8.83
10	-	-	1	8.28	-	-	-	8.28
12	-	-	1	8.00	-	-	-	8.00

Table A.1: Fit parameters of time-resolved fluorescent emission at 520nm.

In tab. A.2 the peak intensities $I([Q])$ of the static fluorescent emission are reported for different analyte concentrations and the calculated ratios for the intensities and lifetimes.

[Q] mM	$I([Q])$counts	$I_0/I([Q])$	$\tau_0/\tau([Q])$	$(I_0/I([Q]))/(\tau_0/\overline{\tau}([Q]))$
0	42280 $(=I_0)$	1.00	1.00	1.00
2	31850	1.33	1.02	1.30
4	23250	1.82	1.07	1.70
6	17670	2.39	1.11	2.15
8	14130	2.99	1.15	2.60
10	11320	3.73	1.23	3.03
12	10000	4.23	1.27	3.33

Table A.2: Calculated ratios of intensities and lifetimes.

In fig. A.4 the Stern-Volmer plot of the QxBOX solution as a function of the analyte concentration is reported. From the best curve fits of the data, the dynamic Stern-Volmer $k_D = 23 mol^{-1}$ and the association rate $k_A = 203 mol^{-1}$ constants can be deduced. The quadratic behavior of the curve I_0/I confirms the formation of non-emitting *complexes*, suggesting that the host-guest association is the predominant cause of quenching phenomenon.

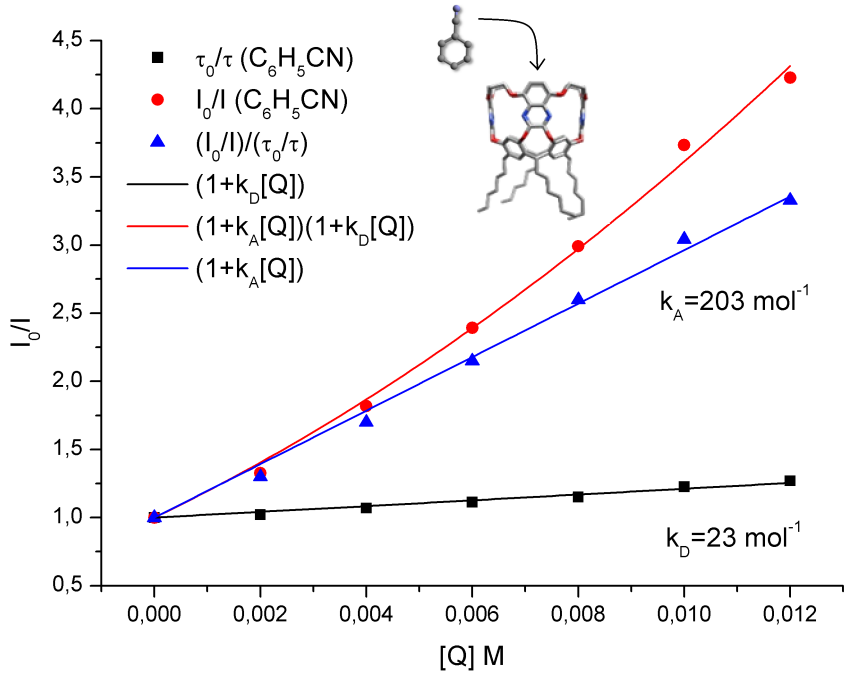

Figure A.4: Stern-Volmer plot of QxBox 0.5mM in acetone versus benzonitrile concentration in solution.

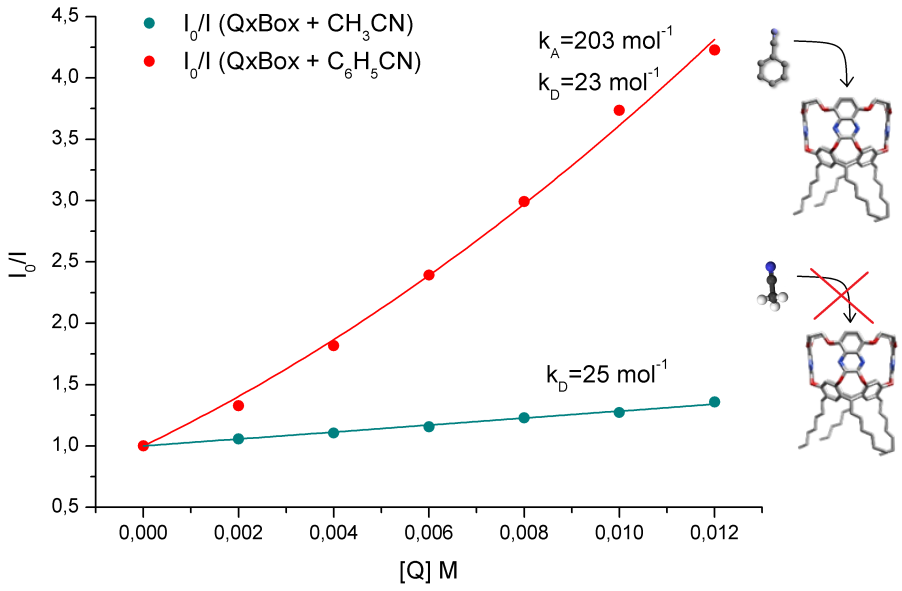

Figure A.5: Stern-Volmer plot of QxBox 0.5mM in acetone versus acetonitrile (in green) and benzonitrile (in red) concentration in solution. Red and green circles are the experimental data and solid lines are their best curve fits.

The measurements have been repeated using a different analyte, namely acetonitrile (CH_3CN), that does not exhibit any specific chemical affinity with QxBOX cavity.In this case the *complexation* of the ligand inside the receptor mouth is not favored and a linear behavior of the curve I_0/I is expected. In fig. A.5 a comparison between the I_0/I curves for benzonitrile (in red) and acetonitrile (in green) cases. The linear behavior of the intensity ratio I_0/I for the aliphatic guest is evidence of dynamic quenching, while static quenching does not occur. The dynamic Stern-Volmer constant, indeed, is very close to that found for the benzonitrile case. This evidence is a confirmation that only aromatic guests with a strong chemical affinity with the QxBOX cavity, as benzonitrile, can be engulfed forming stable and non-emitting *complexes*.

These preliminary analysis want to propose a strategy to study the effects of complexation on the fluorescence activity of QxBOX receptors. Measurements at several concentrations of the analyte in solution have been carried out to give a precise and quantitative analysis of the host-guest association effects, whose study in liquid is only the first step. In the future, QxBOX grafted on solid substrates will be probed to elucidate the receptor-ligand interactions directly at solid/liquid and solid/gas interfaces.

References

[1] Elisa Biavardi, Stefania Federici, Cristina Tudisco, Daniela Menozzi, Chiara Massera, Andrea Sottini, Guglielmo G. Condorelli, Paolo Bergese, and Enrico Dalcanale. Cavitand-grafted silicon microcantilevers as a universal probe for illicit and designer drugs in water. *Angew. Chem., Int. Ed.*, pages 1–7, 2014.

[2] Federica Bianchi, Roberta Pinalli, Franco Ugozzoli, Silvia Spera, Maria Careri, and Enrico Dalcanale. Cavitands as superior sorbents for benzene detection at trace level. *New J. Chem.*, 27:502–509, 2003.

[3] Elisa Biavardi, Cristina Tudisco, Francesca Maffei, Alessandro Motta, Chiara Massera, Guglielmo G. Condorelli, and Enrico Dalcanale. Exclusive recognition of sarcosine in water and urine by a cavitand-functionalized silicon surface. *Proc. Natl. Acad. Sci. U. S. A.*, 109(7):2263–2268, 2012.

[4] Dmitry M Rudkevich, Göran Hilmersson, and Julius Rebek. Self-folding cavitands. *Journal of the American Chemical Society*, 120(47):12216–12225, 1998.

[5] Simone Mosca, Yang Yu, and Julius Rebek Jr. Preparative scale and convenient synthesis of a water-soluble, deep cavitand. *Nature protocols*, 11(8):1371–1387, 2016.

[6] Roberta Pinalli, Giovanna Brancatelli, Alessandro Pedrini, Daniela Menozzi, Daniel Hernández, Pablo Ballester, Silvano Geremia, and Enrico Dalcanale. The origin of selectivity in the complexation of n-methyl amino acids by tetraphosphonate cavitands. *Journal of the American Chemical Society*, 138(27):8569–8580, 2016.

[7] Oliver Dumele, Nils Trapp, and François Diederich. Halogen bonding molecular capsules. *Angewandte Chemie International Edition*, 54(42):12339–12344, 2015.

[8] Kari Rissanen, Leonard J Barbour, and Leonard R MacGillivray. Structural macrocyclic supramolecular chemistry. *CrystEngComm*, 16(18):3644–3645, 2014.

[9] Scott J Dalgarno, Praveen K Thallapally, Leonard J Barbour, and Jerry L Atwood. Engineering void space in organic van der waals crystals: calixarenes lead the way. *Chemical Society Reviews*, 36(2):236–245, 2007.

[10] Fraser Hof, Stephen L Craig, Colin Nuckolls, and Julius Rebek Jr. Molecular encapsulation. *Angewandte Chemie International Edition*, 41(9):1488–1508, 2002.

[11] M Vincenti, E Pelizzetti, E Dalcanale, and Paolo Soncini. Molecular recognition in the gas phase. *Pure and applied chemistry*, 65(7):1507–1512, 1993.

[12] Christoph A Schalley. Molecular recognition and supramolecular chemistry in the gas phase. *Mass spectrometry reviews*, 20(5):253–309, 2001.

[13] Rong Lu, Wei Gan, Bao-hua Wu, Hua Chen, and Hong-fei Wang. Vibrational polarization spectroscopy of ch stretching modes of the methylene group at the vapor/liquid interfaces with sum frequency generation. *The Journal of Physical Chemistry B*, 108(22):7297–7306, 2004.

[14] PB Miranda and YR Shen. Liquid interfaces: a study by sum-frequency vibrational spectroscopy. *The Journal of Physical Chemistry B*, 103(17):3292–3307, 1999.

[15] Cherry S Santos and Steven Baldelli. Gas- liquid interface of hydrophobic and hydrophilic room-temperature ionic liquids and benzene: Sum frequency generation and surface tension studies. *The Journal of Physical Chemistry C*, 112(30):11459–11467, 2008.

[16] PB Miranda, V Pflumio, H Saijo, and YR Shen. Conformation of surfactant monolayers at solid/liquid interfaces. *Chemical physics letters*, 264(3):387–392, 1997.

[17] PB Miranda, V Pflumio, H Saijo, and YR Shen. Surfactant monolayers at solid–liquid interfaces: conformation and interaction. *Thin Solid Films*, 327:161–165, 1998.

[18] Jingming Zhang, Haohan Wu, Thomas J Emge, and Jing Li. A flexible mmof exhibiting high selectivity for co2 over n2, ch4 and other small gases. *Chem. Comm.*, 46(48):9152–9154, 2010.

[19] Francisco CB Maia and Paulo B Miranda. Molecular ordering of conjugated polymers at metallic interfaces probed by sfg vibrational spectroscopy. *The Journal of Physical Chemistry C*, 119(13):7386–7399, 2015.

[20] Zhan Chen. Investigating buried polymer interfaces using sum frequency generation vibrational spectroscopy. *Progress in polymer science*, 35(11):1376–1402, 2010.

[21] Chuan Leng, Yuwei Liu, Courtney Jenkins, Heather Meredith, Jonathan J Wilker, and Zhan Chen. Interfacial structure of a dopa-inspired adhesive polymer studied by sum frequency generation vibrational spectroscopy. *Langmuir*, 29(22):6659–6664, 2013.

[22] PB Miranda, V Pflumio, H Saijo, and YR Shen. Surfactant monolayers at solid–liquid interfaces: conformation and interaction. *Thin Solid Films*, 327:161–165, 1998.

[23] Xiangke Chen, Wei Hua, Zishuai Huang, and Heather C Allen. Interfacial water structure associated with phospholipid membranes studied by phase-sensitive vibrational sum frequency generation spectroscopy. *Journal of the American Chemical Society*, 132(32):11336–11342, 2010.

[24] Khoi Tan Nguyen, Ronald Soong, Sang-Choul lm, Lucy Waskell, Ayyalusamy Ramamoorthy, and Zhan Chen. Probing the spontaneous membrane insertion of a tail-anchored membrane protein by sum frequency generation spectroscopy. *Journal of the American Chemical Society*, 132(43):15112–15115, 2010.

[25] II Rzeznicka, Ravindra Pandey, Michael Schleeger, Mischa Bonn, and Tobias Weidner. Formation of lysozyme oligomers at model cell membranes monitored with sum frequency generation spectroscopy. *Langmuir*, 30(26):7736–7744, 2014.

[26] Shuji Ye, Khoi Tan Nguyen, Stéphanie V Le Clair, and Zhan Chen. In situ molecular level studies on membrane related peptides and proteins in real time using sum frequency generation vibrational spectroscopy. *Journal of structural biology*, 168(1):61–77, 2009.

[27] Y. R. Shen. Surface properties probed by second-harmonic and sum-frequency generation. *Nature*, 337:519–525, 1989.

[28] John C Conboy, Marie C Messmer, and Geraldine L Richmond. Dependence of alkyl chain conformation of simple ionic surfactants on head group functionality as studied by vibrational sum-frequency spectroscopy. *J. Phys. Chem. B*, 101(34):6724–6733, 1997.

[29] P Guyot-Sionnest, R Superfine, JH Hunt, and YR Shen. Vibrational spectroscopy of a silane monolayer at air/solid and liquid/solid interfaces using sum-frequency generation. *Chem. Phys. Lett.*, 144(1):1–5, 1988.

[30] Dennis K. Hore, Mathew Y. Hamamoto, and Geraldine L. Richmond. Mid-infrared second-order susceptibility of $\alpha-$quartz and its application to visible-infrared surface sum-frequency spectroscopy. *J. Chem. Phys.*, 121(24):12589–12594, 2004.

[31] J. Y. Huang, R. Superfine, and Y. R. Shen. Nonlinear spectroscopic study of coadsorbed liquid-crystal and surfactant monolayers: Conformation and interaction. *Phys. Rev. A*, 42:3660–3663, Sep 1990.

[32] F Lagugné-Labarthet, T Yu, WR Barger, DK Shenoy, E Dalcanale, and YR Shen. Orientation of cavitands at air/water and air/solid interfaces studied by second harmonic generation. *Chem. Phys. Lett.*, 381(3):322–328, 2003.

[33] Alex G. Lambert, Paul B. Davies, and David J. Neivandt. Implementing the theory of sum frequency generation vibrational spectroscopy: A tutorial review. *Applied Spectroscopy Reviews*, 40(2):103–145, 2005.

[34] Vladimir A Azov, Andrew Beeby, Martina Cacciarini, Andrew G Cheetham, Francois Diederich, Markus Frei, James K Gimzewski, Volker Gramlich, Bert Hecht, Bernhard Jaun, et al. Resorcin [4] arene cavitand-based molecular switches. *Advanced Functional Materials*, 16(2):147–156, 2006.

[35] Enrico Dalcanale, Giuliano Costantini, and Paolo Soncini. Removal of organic pollutants from water via molecular inclusion within a cavitand. *Journal of inclusion phenomena and molecular recognition in chemistry*, 13(1):87–92, 1992.

[36] Guglielmo G Condorelli, Alessandro Motta, Maria Favazza, Ettore Gurrieri, Paolo Betti, and Enrico Dalcanale. Molecular recognition of halogen-tagged aromatic vocs at the air–silicon interface. *Chemical Communications*, 46(2):288–290, 2010.

[37] François Lagugné-Labarthet, Yong Q An, Tao Yu, Yuen R Shen, Enrico Dalcanale, and Devanand K Shenoy. Proton driven vase-to-kite conformational change in cavitands at an air- water interface monitored by surface shg. *Langmuir*, 21(16):7066–7070, 2005.

[38] Pasquale Pagliusi, Franois Lagugné-Labarthet, Devanand K. Shenoy, Enrico Dalcanale, and Y. Ron Shen. Sensing vase-to-kite switching of cavitands by sum-frequency vibrational spectroscopy. *J. Am. Chem. Soc.*, 128(39):12610–12611, 2006.

[39] Pamela Roncucci, Laura Pirondini, Giuseppe Paderni, Chiara Massera, Enrico Dalcanale, Vladimir A Azov, and François Diederich. Conformational behavior of pyrazine-bridged and mixed-bridged cavitands: A general model for solvent effects on thermal vase–kite switching. *Chemistry–A European Journal*, 12(18):4775–4784, 2006.

[40] N Riboni, JW Trzcinski, F Bianchi, C Massera, R Pinalli, L Sidisky, E Dalcanale, and M Careri. Conformationally blocked quinoxaline cavitand as solid-phase microextraction coating for the selective detection of btex in air. *Analytica chimica acta*, 905:79–84, 2016.

[41] JA Armstrong, N Bloembergen, J Ducuing, and PS Pershan. Interactions between light waves in a nonlinear dielectric. *Physical Review*, 127(6):1918, 1962.

[42] M Bass, PA Franken, AE Hill, CW Peters, and G Weinreich. Optical mixing. *Physical Review Letters*, 8(1):18, 1962.

[43] XD Zhu, Hajo Suhr, and YR Shen. Surface vibrational spectroscopy by infrared-visible sum frequency generation. *Physical Review B*, 35(6):3047, 1987.

[44] Alex G Lambert, Paul B Davies, and David J Neivandt. Implementing the theory of sum frequency generation vibrational spectroscopy: a tutorial review. *Applied Spectroscopy Reviews*, 40(2):103–145, 2005.

[45] YR Shen. Basic theory of surface sum-frequency generation. *The Journal of Physical Chemistry C*, 116(29):15505–15509, 2012.

[46] De-Sheng Zheng, Yuan Wang, An-An Liu, and Hong-Fei Wang. Microscopic molecular optics theory of surface second harmonic generation and sum-frequency generation spectroscopy based on the discrete dipole lattice model. *International Reviews in Physical Chemistry*, 27(4):629–664, 2008.

[47] Hong-Fei Wang, Wei Gan, Rong Lu, Yi Rao, and Bao-Hua Wu. Quantitative spectral and orientational analysis in surface sum frequency generation vibrational spectroscopy (sfg-vs). *International Reviews in Physical Chemistry*, 24(2):191–256, 2005.

[48] X Zhuang, PB Miranda, D Kim, and YR Shen. Mapping molecular orientation and conformation at interfaces by surface nonlinear optics. *Physical Review B*, 59(19):12632, 1999.

[49] K. M. Gough. Theoretical analysis of molecular polarizabilities and polarizability derivatives in hydrocarbons. *The Journal of Chemical Physics*, 91(4):2424–2432, 1989.

[50] RG Snyder. A bond polarizability interpretation of the raman intensities of cyclohexane and cyclohexane-d 12. *Journal of Molecular Spectroscopy*, 36(2):204–221, 1970.

[51] Woongmo Sung, Sangjun Seok, Doseok Kim, C. S. Tian, and Y. R. Shen. Sum-frequency spectroscopic study of langmuir monolayers of lipids having oppositely charged headgroups. *Langmuir*, 26(23):18266–18272, 2010.

[52] Xing Wei, Seok-Cheol Hong, Xiaowei Zhuang, Tomohisa Goto, and YR Shen. Nonlinear optical studies of liquid crystal alignment on a rubbed polyvinyl alcohol surface. *Physical Review E*, 62(4):5160, 2000.

[53] Donald J Cram and Jane M Cram. *Container molecules and their guests*. Number 4. Royal Society of Chemistry, 1997.

[54] D'Souza. Cyclodextrins. *Chem. Rev*, 98(5):1741–2076, 1998.

[55] François Diederich. *Cyclophanes*, volume 2. Royal Society of Chemistry, 1991.

[56] Dmitry M Rudkevich and Julius Rebek Jr. Deepening cavitands. *European journal of organic chemistry*, 1999(9):1991–2005, 1999.

[57] Ayub Jasat and John C Sherman. Carceplexes and hemicarceplexes. *Chemical reviews*, 99(4):931–968, 1999.

[58] Dmitry M Rudkevich. Nanoscale molecular containers. *Bulletin of the Chemical Society of Japan*, 75(3):393–413, 2002.

[59] Dmitry M Rudkevich. Molecular containers in action. *Functional Synthetic Receptors*, pages 257–298, 2005.

[60] Paolo Soncini, Stefanio Bonsignore, Enrico Dalcanale, and Franco Ugozzoli. Cavitands as versatile molecular receptors. *The Journal of Organic Chemistry*, 57(17):4608–4612, 1992.

[61] Harold Boerrigter, Willem Verboom, and David N Reinhoudt. Novel resorcinarene cavitand-based cmp (o) cation ligands: synthesis and extraction properties. *The Journal of organic chemistry*, 62(21):7148–7155, 1997.

[62] Donald J. Cram. Cavitands: Organic hosts with enforced cavities. *Science*, 219(4589):1177–1183, 1983.

[63] Pierrick Clément, Saša Korom, Claudia Struzzi, Enrique J Parra, Carla Bittencourt, Pablo Ballester, and Eduard Llobet. Deep cavitand self-assembled on au nps-mwcnt as highly sensitive benzene sensing interface. *Advanced Functional Materials*, 25(26):4011–4020, 2015.

[64] Marco Dionisio, Jan M Schnorr, Vladimir K Michaelis, Robert G Griffin, Timothy M Swager, and Enrico Dalcanale. Cavitand-functionalized swcnts for n-methylammonium detection. *J. Am. Chem. Soc.*, 134(15):6540–6543, 2012.

[65] F Lagugné-Labarthet, T Yu, WR Barger, DK Shenoy, E Dalcanale, and YR Shen. Orientation of cavitands at air/water and air/solid interfaces studied by second harmonic generation. *Chemical physics letters*, 381(3):322–328, 2003.

[66] Federica Bianchi, Alessandro Bedini, Nicolo‘ Riboni, Roberta Pinalli, Adolfo Gregori, Leonard Sidisky, Enrico Dalcanale, and Maria Careri. Cavitand-based solid-phase microextraction coating for the selective detection of nitroaromatic explosives in air and soil. *Analytical chemistry*, 86(21):10646–10652, 2014.

[67] Roberta Pinalli and Enrico Dalcanale. Supramolecular sensing with phosphonate cavitands. *Accounts of chemical research*, 46(2):399–411, 2012.

[68] Arun Sreekumar, Laila M Poisson, Thekkelnaycke M Rajendiran, Amjad P Khan, Qi Cao, Jindan Yu, Bharathi Laxman, Rohit Mehra, Robert J Lonigro, Yong Li, et al. Metabolomic profiles delineate potential role for sarcosine in prostate cancer progression. *Nature*, 457(7231):910–914, 2009.

[69] Anne L. Plant. Supported hybrid bilayer membranes as rugged cell membrane mimics. *Langmuir*, 15(15):5128–5135, 1999.

[70] Kyoungmoo Koh, Kohji Ohno, Yoshinobu Tsujii, and Takeshi Fukuda. Precision synthesis of organic/inorganic hybrid nanocapsules with a silanol-functionalized micelle template. *Angewandte Chemie International Edition*, 42(35):4194–4197, 2003.

[71] Jianzhong Du, Yongming Chen, Yanhong Zhang, Charles C Han, Karl Fischer, and Manfred Schmidt. Organic/inorganic hybrid vesicles based on a reactive block copolymer. *Journal of the American Chemical Society*, 125(48):14710–14711, 2003.

[72] Elisa Biavardi, Maria Favazza, Alessandro Motta, Ignazio L. FragalÃ , Chiara Massera, Luca Prodi, Marco Montalti, Monica Melegari, Guglielmo G. Condorelli, and Enrico Dalcanale. Molecular recognition on a cavitand-functionalized silicon surface. *Journal of the American Chemical Society*, 131(21):7447–7455, 2009.

[73] Shen Ye, Satoshi Nihonyanagi, and Kohei Uosaki. Sum frequency generation (sfg) study of the ph-dependent water structure on a fused quartz surface modified by an octadecyltrichlorosilane (ots) monolayer. *Physical Chemistry Chemical Physics*, 3(16):3463–3469, 2001.

[74] Na Ji, Victor Ostroverkhov, Chao-Yuan Chen, and Yuen-Ron Shen. Phase-sensitive sum-frequency vibrational spectroscopy and its application to studies of interfacial alkyl chains. *Journal of the American Chemical Society*, 129(33):10056–10057, 2007.

[75] A Aprile, P Pagliusi, F Ciuchi, MP De Santo, R Pinalli, and E Dalcanale. Probing cavitand–organosilane hybrid bilayers via sum-frequency vibrational spectroscopy. *Langmuir*, 30(43):12843–12849, 2014.

[76] MM Gentleman and JA Ruud. Role of hydroxyls in oxide wettability. *Langmuir*, 26(3):1408–1411, 2009.

[77] György Varsányi. *Vibrational spectra of benzene derivatives*. Elsevier, 2012.

[78] Arianna Aprile, Federica Ciuchi, Roberta Pinalli, Enrico Dalcanale, and Pasquale Pagliusi. Probing molecular recognition at the solid–gas interface by sum-frequency vibrational spectroscopy. *The Journal of Physical Chemistry Letters*, 7(15):3022–3026, 2016.

[79] Yusuke Hiraku and Shosuke Kawanishi. Oxidative dna damage and apoptosis induced by benzene metabolites. *Cancer Research*, 56(22):5172–5178, 1996.

[80] Prema Kolachana, Vangala V Subrahmanyam, Kathleen B Meyer, Luoping Zhang, and Martyn T Smith. Benzene and its phenolic metabolites produce oxidative dna damage in hl60 cells in vitro and in the bone marrow in vivo. *Cancer research*, 53(5):1023–1026, 1993.

[81] Cristina Andreoli, Paola Leopardi, and Riccardo Crebelli. Detection of dna damage in human lymphocytes by alkaline single cell gel electrophoresis after exposure to benzene or benzene metabolites. *Mutation Research/Fundamental and Molecular Mechanisms of Mutagenesis*, 377(1):95–104, 1997.

[82] Bidisha Mukherjee, Anindita Dutta, Sanghita Roychoudhury, and Manas Ranjan Ray. Chronic inhalation of biomass smoke is associated with dna damage in airway cells: involvement of particulate pollutants and benzene. *Journal of applied toxicology*, 33(4):281–289, 2013.

[83] Federico Bertani, Nicolò Riboni, Federica Bianchi, Giovanna Brancatelli, Elizabeth S Sterner, Roberta Pinalli, Silvano Geremia, Timothy M Swager, and Enrico Dalcanale. Triptycene-roofed quinoxaline cavitands for the supramolecular detection of btex in air. *Chemistry–A European Journal*, 22(10):3312–3319, 2016.

[84] Federica Bianchi, Monica Mattarozzi, Paolo Betti, Franco Bisceglie, Maria Careri, Alessandro Mangia, Leonard Sidisky, Stefano Ongarato, and Enrico Dalcanale. Innovative cavitand-based sol- gel coatings for the environmental monitoring of benzene and chlorobenzenes via solid-phase microextraction. *Analytical chemistry*, 80(16):6423–6430, 2008.

[85] Markus Frei, Federica Marotti, and François Diederich. Znii-induced conformational control of amphiphilic cavitands in langmuir monolayers. *Chem. Comm.*, 12:1362–1363, 2004.

[86] Yi Rao, Matthew Comstock, and Kenneth B Eisenthal. Absolute orientation of molecules at interfaces. *The Journal of Physical Chemistry B*, 110(4):1727–1732, 2006.

[87] Melissa C Kido Soule, Dennis K Hore, Donna M Jaramillo-Fellin, and Geraldine L Richmond. Differing adsorption behavior of environmentally important cyanophenol isomers at the air-water interface. *The Journal of Physical Chemistry B*, 110(33):16575–16583, 2006.

[88] Yoshihito Tanaka, S Lin, M Aono, and T Suzuki. Sum-frequency vibrational spectroscopy of a monolayer self-assembled on gold: interference between resonant and nonresonant contributions of nonlinear polarization. *Applied Physics B: Lasers and Optics*, 68(4):713–718, 1999.

[89] Alex G Lambert, David J Neivandt, Adam M Briggs, Eric W Usadi, and Paul B Davies. Interference effects in sum frequency spectra from monolayers on composite dielectric/metal substrates. *The Journal of Physical Chemistry B*, 106(21):5461–5469, 2002.

[90] Alexandre G Brolo, Reuven Gordon, Brian Leathem, and Karen L Kavanagh. Surface plasmon sensor based on the enhanced light transmission through arrays of nanoholes in gold films. *Langmuir*, 20(12):4813–4815, 2004.

[91] Rongzhang Hao, Dianbing Wang, Xianen Zhang, Guomin Zuo, Hongping Wei, Ruifu Yang, Zhiping Zhang, Zhenxing Cheng, Yongchao Guo, Zongqiang Cui, et al. Rapid detection of bacillus anthracis using monoclonal antibody functionalized qcm sensor. *Biosensors and Bioelectronics*, 24(5):1330–1335, 2009.

[92] KD Schierbaum, T Weiss, EU Thoden van Velzen, JFJ Engbersen, DN Reinhoudt, and W Göpel. Molecular recognition by self-assembled monolayers of cavitand receptors. *Science*, 265(5177):1413–1415, 1994.

[93] Marco Dionisio, Francesca Maffei, Enrico Rampazzo, Luca Prodi, Andrea Pucci, Giacomo Ruggeri, and Enrico Dalcanale. Guest-controlled aggregation of cavitand gold nanoparticles and n-methyl pyridinium-terminated peg. *Chemical Communications*, 47(23):6596–6598, 2011.

[94] E Dalcanale and J Hartmann. Selective detection of organic compounds by means of cavitand-coated qcm transducers. *Sensors and Actuators B: Chemical*, 24(1-3):39–42, 1995.

[95] P Nelli, E Dalcanale, G Faglia, G Sberveglieri, and P Soncini. Cavitands as selective materials for qmb sensors for nitrobenzene and other aromatic vapours. *Sensors and Actuators B: Chemical*, 13(1-3):302–304, 1993.

[96] Michele Suman, Micol Freddi, Chiara Massera, Franco Ugozzoli, and Enrico Dalcanale. Rational design of cavitand receptors for mass sensors. *Journal of the American Chemical Society*, 125(40):12068–12069, 2003.

[97] Colin D Bain, Joe Evall, and George M Whitesides. Formation of monolayers by the coadsorption of thiols on gold: variation in the head group, tail group, and solvent. *J. Am. Chem. Soc.*, 111(18):7155–7164, 1989.

[98] Colin D Bain, E Barry Troughton, Yu Tai Tao, Joseph Evall, George M Whitesides, and Ralph G Nuzzo. Formation of monolayer films by the spontaneous assembly of organic thiols from solution onto gold. *Journal of the American Chemical Society*, 111(1):321–335, 1989.

[99] Alex G Lambert, David J Neivandt, Adam M Briggs, Eric W Usadi, and Paul B Davies. Enhanced sum frequency generation from a monolayer adsorbed on a composite dielectric/metal substrate. *The Journal of Physical Chemistry B*, 106(41):10693–10700, 2002.

[100] Paul E Laibinis, George M Whitesides, David L Allara, Yu Tai Tao, Atul N Parikh, and Ralph G Nuzzo. Comparison of the structures and wetting properties of self-assembled monolayers of n-alkanethiols on the coinage metal surfaces, copper, silver, and gold. *Journal of the American Chemical Society*, 113(19):7152–7167, 1991.

[101] Colin D Bain, Paul B Davies, T Hui Ong, Robert N Ward, and Murray A Brown. Quantitative analysis of monolayer composition by sum-frequency vibrational spectroscopy. *Langmuir*, 7(8):1563–1566, 1991.

[102] Margaret A Hines, JA Todd, and P Guyot-Sionnest. Conformation of alkanethiols on au, ag (111), and pt (111) electrodes: A vibrational spectroscopy study. *Langmuir*, 11(2):493–497, 1995.

[103] Gang Ma and Heather C Allen. Dppc langmuir monolayer at the air- water interface: probing the tail and head groups by vibrational sum frequency generation spectroscopy. *Langmuir*, 22(12):5341–5349, 2006.

[104] Ellen C Wrobel, Poliana M Santos, Márcio Lazzarotto, Osvaldo N Oliveira, Thiers M Uehara, Paulo B Miranda, Luciano Caseli, Jarem R Garcia, Sérgio R de Lázaro, Alexandre Camilo Jr, et al. Interaction of para-tert-butylcalix [6] arene molecules in langmuir films with cadmium ions and their effects on molecular conformation and surface potential. *Physical Chemistry Chemical Physics*, 16(47):26168–26175, 2014.

[105] Jakub Waldemar Trzcinski, Roberta Pinalli, Nicolò Riboni, Alessandro Pedrini, Federica Bianchi, Stefano Zampolli, Ivan Elmi, Chiara Massera, Franco Ugozzoli, and Enrico Dalcanale. In search of the ultimate benzene sensor: The etqxbox solution. *ACS Sensors*, 0(ja):null, 0.

[106] AnAn Liu, Zhi Huang, GangHua Deng, and Yuan Guo. Adsorption of benzonitrile at the air/water interface studied by sum frequency generation spectroscopy. *Chinese Science Bulletin*, 58(13):1529–1535, 2013.

[107] Zsolt Csók, Tímea Kégl, Yin Li, Rita Skoda-Földes, László Kiss, Sándor Kunsági-Máté, Matthew H Todd, and László Kollár. Synthesis of elongated cavitands via click reactions and their use as chemosensors. *Tetrahedron*, 69(38):8186–8190, 2013.

[108] Sook Kyung Kim, Byung-Sik Moon, Ju Hyun Park, Young Il Seo, Hwa Soo Koh, Yeo Joon Yoon, Kap Duk Lee, and Juyoung Yoon. A fluorescent cavitand for the recognition of gtp. *Tetrahedron letters*, 46(39):6617–6620, 2005.

[109] Yuji Kubo, Kazusa Tsuruzoe, Sachiko Okuyama, Ryuhei Nishiyabu, and Takashi Fujihara. Resorcin [4] arene cavitand with 1, 3, 2-benzodiazaborolyl walls as a fluorescence receptor for ammonium cations. *Chemical Communications*, 46(20):3604–3606, 2010.

[110] Orion B Berryman, Aaron C Sather, and Julius Rebek Jr. A deep cavitand with a fluorescent wall functions as an ion sensor. *Organic letters*, 13(19):5232–5235, 2011.

[111] Yun Jung Jang, Byung-Sik Moon, Min Sun Park, Bong-Gu Kang, Ji Young Kwon, Jay Sung Joong Hong, Yeo Joon Yoon, Kap Duk Lee, and Juyoung Yoon. New cavitand derivatives bearing four coumarin groups as fluorescent chemosensors for cu

2+ and recognition of dicarboxylates utilizing cu 2+ complex. *Tetrahedron letters*, 47(16):2707–2710, 2006.

[112] Maurice R Eftink. Fluorescence quenching: theory and applications. In *Topics in fluorescence spectroscopy*, pages 53–126. Springer, 2002.

[113] Frauke Schibilla, Linda Stegemann, Cristian A Strassert, Fabio Rizzo, and Bart Jan Ravoo. Fluorescence quenching in β-cyclodextrin vesicles: membrane confinement and host–guest interactions. *Photochemical & Photobiological Sciences*, 15(2):235–243, 2016.